ABSTRACT

Title of Dissertation:	DEVELOPMENT OF AN ENDOTHELIAL CELL/MESENCHYMAL STEM CELL COCULTURE STRATEGY FOR THE VASCULARIZATION OF ENGINEERED BONE TISSUE.
	Charlotte Marianne Piard, Doctor of Philosophy in Bioengineering, 2019
Dissertation directed by:	Fischell Family Distinguished Professor & Department Chair, John P. Fisher, Fischell Department of Bioengineering

In the past two decades, remarkable progress has been made in the development of surgical techniques for bone reconstruction, significantly improving clinical outcomes. However, major reconstruction after trauma or cancer is still limited by the paucity of autologous material and donor site morbidity. Recent advances in the field of tissue engineering have generated new approaches for restoring bone defects. In spite of this progress, the necessity of suitable blood supply to ensure cell function is a major challenge in the development of more complex and functional grafts. Many investigators have successfully demonstrated the use of different strategies including growth factor delivery and in vitro coculture of ECs and MSCs to develop vascular structures. MSCs have the ability to secrete a wide range of bioactive cytokines and growth factors that can influence nearby cells via paracrine signaling. This crosstalk

between ECs and MSCs is mutually beneficial, as ECs enhance osteogenic differentiation of hMSCs through direct cell-cell contact and paracrine signaling. In the native environment of cortical bone, both cell populations, osteogenic and vasculogenic, follow a unique well-defined pattern, called osteons.

The goal of this proposed study was to develop a novel bio-inspired and vascularized bone construct, harvesting the synergistic effects of pro-angiogenic growth factor delivery and coculture of ECs and MSCs. To address this goal, we first developed mesoporous calcium deficient hydroxyapatite apatite microparticles, with biological properties closer to bone than commercially available hydroxyapatite, and capable of efficiently loading and sustainably releasing pro-angiogenic growth factors. We then demonstrated the successful fabrication of a novel bio-inspired 3DP fibrin-PCL composite scaffold, with mechanical strength comparable to bone. The utilization of these scaffolds in constructing osteons for bone regeneration demonstrated the promising capacity of the construct to improve neovascularization. In light of these results, we hypothesized that cell placement or patterning could play a critical role in neovascularization. Which lead us to investigate the role of distance between cell populations, introduced via 3D printing, in ECs/MSCs crosstalk. Our results suggested that controlling the distance between ECs and MSCs in coculture, using 3D printing, could influence angiogenesis.

DEVELOPMENT OF AN ENDOTHELIAL CELL/MESENCHYMAL STEM CELL COCULTURE STRATEGY FOR THE VASCULARIZATION OF ENGINEERED BONE TISSUE

by

Charlotte Marianne Piard

Dissertation submitted to the Faculty of the Graduate School of the
University of Maryland, College Park, in partial fulfillment
of the requirements for the degree of
Doctor of Philosophy
2019

Advisory Committee:
Professor John P. Fisher, Chair
Professor Yu Chen
Professor Steven M. Jay
Professor Helim Aranda-Espinoza
Professor Carol Keefer

Acknowledgments

It is a pleasure to thank the many people who made this thesis possible. I would like to thank my advisor, Dr. John Fisher, for his support, encouragement, sound advice and mentorship throughout the completion of this work. I would also like to extend my appreciation to my committee members for providing guidance and suggestions that have improved the outcome of my research throughout this process. I am especially grateful to all my friends and lab mates, past and present, in the Tissue Engineering and Biomaterials Lab and in the BIOE department for their help and support. With a special mention to Laurie and Imaly, for their honest feedback, support and of course friendship throughout this journey. I would also like to acknowledge Timur Kamalitdinov and Rachel Luthcke, the undergraduate researchers whose work contributed to this project.

Table of Contents

List of Tables

List of Figures

Chapter 1: Introduction

The need for engineered bone tissue.

With more than one million procedures performed in the United States annually, plus an additional 2.2 million worldwide, bone is the second most transplanted tissue [1] [2]. Those numbers are expected to increase in the next decade due to a variety of factors, including an aging population and deteriorating physical activity levels [3].

Bones have two main purposes, structural and metabolic, accomplished through maintenance of a rigid skeletal extracellular matrix (ECM) [4]-[5]. On the macroscopic scale, bone is made of dense cortical bone forming an outside shell and cancellous bone within the marrow cavity. Bone tissue is a mineralized connective tissue and is formed by three different cell types: osteoblasts - which differentiate from pluripotent mesenchymal cells (MSCs), osteocytes, and osteoclasts [6]. Calcium phosphates, in the form of hydroxyapatite, are the principal mineral content of bone's extracellular matrix (ECM), making up to 70% of the ECM. The organic matrix (22%) consists mostly of type I collagen (90% of the organic matrix) [7,8]. (See Appendix 1: A brief summary of bone biology. for a more detailed summary of bone biology). Additionally, bones are well known for their innate healing abilities: osteoblasts, responsible for the secretion and mineralization of ECM, and osteoclasts, resorbing the ECM, work together to

regenerate and repair damaged bone tissue; yet this ability can be undermined by the severity and size of the injury or disease [9].

For larger bone defects repair, allogenic, autologous and prosthetic grafts are often used. Non-immunogenic and histocompatible autografts are currently the gold standard for bone grafts, as they are able to achieve osteoconduction, osteoinduction, and osteogenesis [10,11]. Although autografts and allografts have proven successful in many cases, they present significant drawbacks, including limited sources, a requirement for secondary operations, risks of disease transmission and immunoreactions [12–14]. In addition, extensive studies have shown that with autologous grafts, complications can affect 10 to 30% of patients [15]. Other sources of materials have been used for bone repair including metals, ceramics, and polymers. However, metals can provide sufficient physical strength but have poor patient site integration, and are unable to be remodeled [16], while ceramics are biocompatible and are osteoconductive but they tend to be brittle [17].

Bone tissue engineering (BTE) is a promising alternative, for the treatment of bone defects that will ideally eliminate the issues described above [18]. BTE aims at not only repairing bone defects but also enhance bone regeneration allowing host tissue in-growth [19]. Tissue engineering strategies are based on several key components: (i) a biocompatible porous scaffold mimicking the bone's natural environment that will allow, (ii) osteogenic cells to lay down new bone matrix directed by, (iii) morphogenic signals. Tremendous progress over the last decades has been made in BTE, with an exponentially increasing number of papers published on the PubMed database since the

1990s [20]. But despite the increasing research expenditure and discoveries, there is still a major discrepancy between scientific research efforts and clinical applications.

*The need for **vascularized** engineered bone tissue.*

Vascularization is a crucial process during the growth and development of bone, yet it remains one of the main challenges in the reconstruction of large bone defects [21]. Vasculature is a requirement when engineering most tissues. The diffusion distance for nutrients and oxygen implicit to cell survival is limited (150–200 μm) and this can lead to necrosis in the center of the supportive scaffolds [22]. Many studies in BTE have relied on the spontaneous organization of endothelial cells, and uncontrolled angiogenesis, to form a vascular network. However, technologies to control and direct neovascularization within a mineralized construct have been developed to improve clinical outcomes from bone grafting procedures. Many authors have successfully demonstrated the use of different strategies to develop vascular structures, including growth factor delivery [23], channeled scaffolds [24], perfusion bioreactors [25], cell cocultures [26], cell functionalization [27], and in vivo systems [28].

One of the most traditional methods to initiate angiogenesis and osteogenesis include delivering growth factors (GFs), such as vascular endothelial growth factor (VEGF) and bone morphogenetic proteins (BMPs) [29]. Even though delivery of growth factors is known to enhance angiogenesis and osteogenesis in construct, their dosage and timing must be tightly controlled. Several particle-based systems, either naturally or synthetically derived, have been developed to deliver growth factors (GFs), including VEGF, to the target sites, in a more controlled fashion. This option will be

explored in Chapter 2: Development of Porous Hydroxyapatite Microparticles for the Exogenous Delivery of VEGF, which summarized our effort to develop porous osteoconductive hydroxyapatite microparticles has a novel way to encapsulate and deliver VEGF.

Because vascularized bone regeneration requires cross-communication between multiple cell types, the use of in vitro coculture of human umbilical vein endothelial cells (HUVECs) and human mesenchymal stem cells (hMSCs) is also one of the most explored options, as it allows for concurrent creation of a vascular network as well as the target tissue [30–32]. It is well established that both cell types secrete specific growth factors that are mutually beneficial. For example, endothelial cells are known to secrete growth factors such as insulin growth factor-1 [33], endothelin-1, and bone morphogenic protein-2, promoting osteogenic growth and differentiation of the MSCs [34]. In most cases, both cells population are either seeded onto or encapsulated into a scaffold in a somewhat random manner. However, additive manufacturing (AM), or 3D printing has emerged in the recent years as a promising method for the fabrication of porous scaffolds with a higher resolution, accurate cell patterning, and recapitulating complex hierarchical structures. The use of 3D printing to create cell-laden scaffolds for BTE is further explored in Chapter 3: Cell-Laden 3D Printed Scaffolds for Bone Tissue Engineering. Thanks to 3D printing technologies, we developed a bio-inspired coculture system, inspired by osteons found in cortical bones, in order to enhanced neovascularization of the scaffolds. The results of this study are detailed in Chapter 4: Bioprinted Osteon-like Scaffolds Enhance in Vivo Neovascularization.

Finally, research efforts by a number of groups have focused on strategies that can enhance the secretory function of MSCs and ECs in cocultures. Recently, studies suggested that cell-cell communication and paracrine secretion can be affected by the substrate microarchitecture [35], mechanical environment [36] or the matrix stiffness [37]. However, little is known about the effect of cell patterning and the distance between cell populations on their crosstalk. The fact that different tissue types, such as osteons in bones, have precisely regulated architecture, combined with positive results from Chapter 4, suggests that characteristic features related to the number, types, and spacing of cells might be critical to tissue function. This led us to investigate how the distance between cells in different 3D printed co-cultures affected angiogenesis by modulating cell-cell communication. Our findings are presented in Chapter 5: Cell-to-Cell distance of HUVECS and MSCs in 3D printed cocultures impacts cellular interactions and angiogenesis..

Objectives

As discussed above, most bone tissue engineering strategies failed to reach clinical stages. The need for new technologies to control and direct neovascularization is critical in order to obtain viable bone graft. In this dissertation, we focused specifically on developing bio-inspired vascularization strategies, based on what is found in the native bone. Specifically, this work aims to provide an alternative approach to the fabrication of vascularized bone tissue engineering scaffolds, through the development and characterization of a novel growth factor delivery system and novel 3D printed cocultures of MSCs and ECs. The aims of this work are as follow:

1. Develop mesoporous calcium deficient hydroxyapatite apatite microparticles, capable of efficiently loading and sustainably releasing pro-angiogenic growth factors.
2. Establish a 3D printed bio-inspired scaffold that promotes bone regeneration and neovascularization.

a. Develop a 3D printed biphasic osteon-like scaffold that is biocompatible, and possess mechanical properties close to cortical bone.

b. Investigate the cross talk between ECs-MSCs within bio-inspired 3D printed cocultures.

c. Demonstrate the positive healing capacities (bone formation and neovascularization) of optimized 3DP scaffolds in a rat cranial defect.

The successful completion of these objectives will result in the development of a unique method of encapsulating VEGF that could hold great potentials for drug-delivery applications and a broad utility in many bone tissue engineering applications where sustained release of factors in a local environment is advantageous. In addition, the development of bio-inspired osteon-like construct could potentially be developed as scaffolds in vascularized bone tissue engineering. We see this as a major step towards creating a vascularized tissue-engineered bone construct of a relevant size that will fill a void in the regenerative medicine field.

Chapter 2: Development of Porous Hydroxyapatite Microparticles for the Exogenous Delivery of VEGF

Introduction

One of the biggest challenges faced in the field of bone tissue engineering is promoting the growth of vasculature within engineered tissues, to enable sufficient engraftment and integration within the host [38]. A variety of approaches have been developed for this purpose. The delivery of vascular endothelial growth factor (VEGF) is a particularly promising way to enhance angiogenesis due to the fact that it has the ability to increase vascular network formation and vascular permeability [39,40] resulting in increased blood flow and access to the defect site by progenitor cells.

Hydrogels are the most commonly reported delivery system for growth factors (GFs) but are generally unable to release GFs for extended periods [41,42]. Moreover, uncontrolled delivery of growth factors can also lead to heterotopic tissue formation or hematomas in soft tissues. This occurs as a result of GFs leakage into other areas of the body, due to the uncontrolled manner in which the GF is released [43]. This has led to the emergence of GFs delivery systems in the form of microparticles, which protect the GF while controlling its release [44,45]. The scientific literature describes numerous methodologies for encapsulating drugs in a variety of matrix materials [46,47]. To be used as a GFs carrier, the material forming the microparticles must have the ability to (i) incorporate a drug either physically or chemically, (ii) retain the drug, (iii) be gradually degraded, and deliver the drug in a controlled manner over time [48]. Calcium phosphates (CaP) met all those criteria.

Hydroxyapatite (HA), (Ca10(PO4)6(OH)2, HA), is a form of CaP with a Ca/P ratio of 1.67. HA is widely used in bone tissue engineering due to its structural and chemical similarities with the key mineral component of bone [7,49–51]. HA is also used in chromatography for purification and separation as an absorbent agent to its excellent absorption of many molecules [52]. Favorable biological properties, which includes biocompatibility, bioaffinity, osteoconduction and in certain cases, osteoinduction [53], of HA over other ceramics are some of the reasons that CaP systems are increasingly being explored as drug delivery systems for orthopedics, dental and maxillofacial applications. Porous hydroxyapatite microparticles (HAp) can be prepared according to a great diversity of methods, the simplest being chemical precipitation [54].

In the present study, the overall objective was to enhance the regenerative capacity of tissue engineering scaffolds through the incorporation of therapeutic GFs. Specifically, collagen scaffolds were functionalized with VEGF-releasing hydroxyapatite particles, in an attempt to engineer a material capable of localizing and sustaining the release of VEGF over extended periods. We hypothesized that a synthetic system presenting an osteoconductive surface and capable of delivering an angiogenic growth factor in a localized and sustained manner would enhance osteogenesis as well as angiogenesis. To this end, the first aim was to develop microparticles and characterize their size, chemical properties and Ca/P ratio to validate the formation of hydroxyapatite. The second aim was to evaluate the osteogenic potential of HAp when cultured with mesenchymal stem cells (hMSCs) and compare it to commercially available hydroxyapatite (SBp). The final aim was to characterize the encapsulation and release

of VEGF in the HAp and assess the angiogenic potential of the VEGF-HAp when culture with endothelial cells.

Materials and Methods

Microparticles Synthesis and Characterization

Synthesis. All chemicals, including calcium chloride anhydrous (CaCl2), sodium carbonate anhydrous (Na2CO3), disodium phosphate dodecahydrate (Na2HPO4·12H2O), aspartic acid (Asp), and sodium dodecyl sulfate (SDS) were purchased from Sigma (St. Louis, MO). Hydroxyapatite particles (HAp) were synthesized in a two-step reaction previously described elsewhere [55] (**Figure 1a**). Aspartic acid and sodium dodecyl sulfate were used as a surfactant to form hollow calcium carbonate (CaCO3) sacrificial template. HAp was then formed by an anion exchange process between CaCO3 and disodium phosphate dodecahydrate (Na2HPO4, 12H2O). Briefly, two solution were prepared: (i) 0.1 mol/L of CaCl2, 0.1 mol/L of Na2CO3 and 0.5 g/L of Asp, and (ii) 0.1 mol/L of CaCl2, 0.1 mol/L of Na2CO3, 0.5 g/L Asp and 30 mmol/L SDS. CaCO3 crystals were precipitated by rapidly pouring solution (i) into solution (ii), and stirring for 1 h at 40 °C. Afterward, an equal volume of 0.03 mol/L Na2HPO4-12H2O was added to the CaCO3 solution dropwise, and stirred at a constant rate of 200rpm, for 3h at 50 °C and pH10. After 3h, the collected particles were filtered off, rinsed in distilled water and washed with ethanol. The particles were flash-freeze in liquid nitrogen before being dried in a lyophilizer.

Microparticles morphology & size distributions. The shape and morphology of the microspheres were investigated by field emission scanning electron microscopy (FE-

SEM) (Hitachi SU-70, Japan). The particle size distributions were measured using a Mastersizer S apparatus (Malvern Instruments, United Kingdom), based on dynamic light scattering (DLS). For each analysis, 50 mg of particles in suspension were loaded into the instrument to monitor their sizes and deviations.

X-ray photoelectron spectroscopy (XPS). The chemical composition of the particles and their calcium-phosphate ratio was measured using a high sensitivity Kratos AXIS 165 spectrometer (Kratos Analytical Ltd, United Kingdom).

X-ray powder diffraction (XRD) patterns were examined under a Bruker Apex2 diffractometer (Brucker, Billerica, MA).

Cell Culture

hMSCs (RoosterBio, Frederick, MD) were cultured in RoosterBasal Media supplemented with RoosterBooster, as per the manufacturer's specifications. Cells were expanded on tissue culture polystyrene flasks for 5 days and grown to 90% confluency before being passaged using trypsin/EDTA. Cells at passage P3 were used for the experiments. The osteogenic media was formulated by supplementing growth media (Gibco, Carlsbad, CA) with 100nM dexamethasone (Sigma, St. Louis, MO), 10mM β-glycerophosphate, and 173 mM ascorbic acid (Sigma). HUVECs (Lonza) were cultured in EBM-2 Basal Medium (Lonza) supplemented by EGM-2 SingleQuot Kit. Cells were expanded on tissue culture polystyrene flasks with media changes every 3 days and grown to 80% confluency before being passaged using trypsin/EDTA. Cells at passage P4 were used for the experiments.

Live/Dead Assay. Cell viability was assessed incubation using a Live/Dead assay (Invitrogen) following standard protocols. HAp (2mg/ml) and hMSCs (1.10^6 cells/ml) were suspended in 4 mg/ml type I collagen (Corning) and scaffolds were formed by pipetting 150 µl of the cells/HAp/Collagen solution in a 12 wells plate and incubated 15 min at 37 °C to crosslink. After 24h culture in media, the scaffolds were incubated in 2 mM ethidium homodimer and 4 mM calcein AM (Molecular Probes) for 30 min. Fluorescent and brightfield images were then taken using an inverted microscope (Nikon Eclipse Ti2).

Growth factor loading and VEGF release study.

The typical drug loading and in vitro release experiments were performed as follows. VEGF (Sigma) adsorption to HA was carried out by incubating 2mg/ml HAp into a centrifuge tube containing a solution of 6ng/ ml of VEGF (C0). Store-bought hydroxyapatite (<200nm) (SBp) (Sigma, St. Louis, MO) were used as a control. The solutions were then incubated at 37°C for 1 h on a shaker in order to achieve maximum loading. After centrifugation, the VEGF-loaded microparticles (HAp or SBp) were dried at room temperature under a vacuum overnight. Samples of the supernatants were frozen for later analysis. The concentration of VEGF (C1) contained in the supernatant was determined by Enzyme-Linked Immunosorbent Assay (ELISA) (Abcam, Cambridge, MA). The VEGF-loaded samples were referred to as VEGF-HAp or VEGF-SBp.

The rate at which VEGF molecules were released from freestanding microparticles in an aqueous environment was measured. VEGF-HAp and VEGF-SBp were prepared in

25 mg samples, and incubated at 1 mg/mL, shaking at 37°C. At each predetermined time interval, 200 μL of solution was removed from the vial and flash frozen for later analysis. 200 μL of PBS was replaced in each vial in order to maintain a constant volume. After the collection of samples from all time points, the extracted PBS was analyzed using an ELISA (Abcam, Cambridge, MA) to determine VEGF concentration.

Osteogenic/Angiogenic Potential Experiments

For all experiments, 2mg/ml of particles (HAp or SBp) and 1.10^6 cells/ml were suspended in 4 mg/ml type I collagen (Corning) and scaffolds were formed by pipetting 150 µl of the cells/HAp/Collagen solution in a 12 wells plate. Scaffolds containing no hydroxyapatite were used as controls. For osteogenic experiments, hMSCs were used and cultured in osteogenic media for 14 days along with HAp or SBp. For angiogenic experiments, HUVECs were used and grown in growth media for 7 days, along with VEGF-HAp and VEGF-SBp.

DNA quantification Assay. Scaffolds from each group (n=3) were collected after 0 and 7 days of culture (HUVECs) and 0 and 14 days of culture (hMSCs). Cells were isolated from collagen hydrogels by dissolution in 2 mg/mL collagenase (Sigma) for 30 min at 37°C and a cell pellet was formed by centrifugation. Total DNA was isolated using DNeasy Blood and Tissue Kit (Qiagen) according to the manufacturer instructions. DNA content was quantified using the PicoGreen DNA assay (Invitrogen) following the manufacturer's instructions. An XTT (2,3-bis-(2-methoxy-4-nitro-5-sulfophenyl)-

2H-tetrazolium-5-carboxanilide) (Sigma) assay was performed, following the manufacturer's instructions, at the same time point on all groups to quantify.

Quantitative Reverse Transcriptase Polymerase Chain Reaction (qRT-PCR). After 0, 7 and 14 days (hMSCs) or 0 and 7 days (HUVECs) of culture, scaffolds from each group were collected. To isolate mRNA from the cells, the scaffolds were dissolved in collagenase (Sigma) for 30 min at 37°C and cells were collected by centrifugation. Total RNA was isolated with Trizol Reagent (Invitrogen, Carlsbad, CA) following the supplier's protocol. Reverse Transcription was performed using TaqMan Reverse Transcription Reagents (Applied Biosystems, Foster City, CA) following the supplier's protocol. qRT-PCR was performed using TaqMan PCR Master Mix and TaqMan Gene Expression Assays for either bone morphogenetic protein 2 (BMP2) and osteocalcin (OCN) or vascular endothelial growth factor A (VEGFA) and platelet endothelial cell adhesion molecule (PECAM). Quantification of target genes was performed relative to the reference GADPH gene. The mean minimal cycle threshold values (Ct) were calculated from triplet reactions.

Von Kossa Staining. After 14 days of culture in osteogenic media, hMSCs scaffolds from each group were fixed in 4% paraformaldehyde (PFA) (Sigma) for 15 min. The scaffolds were then dehydrated for histological processing in a series of ethanol dilutions (75%, 90%, 100%), embedded in paraffin (Fisher Scientific), and sectioned using a microtome (Leica) into 5-micron-thick sections. For the Von Kossa staining, the sections were incubated in 2.5% (w/v) silver nitrate for 20 min under UV light, followed by 5% (w/v) sodium carbonate for 5 min, and 0.1% Nuclear Fast Red (Poly Scientific).

Migration Assay.

The scratch wound assay is a simple, quick and inexpensive method to quantify ECs migration. It is based on the ability of EC to fill an area that has been mechanically 'wounded' using a pipette tip on a confluent monolayer of ECs [56]. HUVECs were seeded in 48 well plates at a density of 30,000 cells per well, and incubated for 24h or until a uniform monolayer was formed. The monolayer was then "scratched" using a pipette tip to create a linear gap through the middle of each well. Growth medium supplemented with 0.5 mg/ml VEGF/HAp or 0.5 mg/ml VEGF/SBp were used. Full growth media was used as a positive control, while serum free media was used as a negative control. Images of the wells were taken using an inverted microscope (Nikon Eclipse Ti2) after 0h and 12h of incubation. Pictures were analyzed using ImageJ to determine the overall gap closure, as previously described [57].

Statistical Analysis.

All samples were evaluated in triplicates. Data were analyzed using single-factor analysis of variance followed by Tukey's Multiple Comparison Test assuming normal data distribution with a confidence of 95% ($p<0.05$).

Results and Discussion

Formation of Calcium Deficient Hydroxyapatite Microparticles (CDHAp).

The first aim of this chapter was to develop microparticles and characterize their size, chemical properties and Ca/P ratio to validate the formation of hydroxyapatite. Hydroxyapatite particles (HAp) were synthesized in a two-step reaction. Aspartic acid

and sodium dodecyl sulfate were used as a surfactant to form hollow calcium carbonate (CaCO3) template. HA was then formed by an anion exchange between CaCO3 and disodium phosphate dodecahydrate (Na2HPO4, 12H2O) under constant stirring (**Figure 1**a).

Microparticles were measured to have an average diameter of 8.08 µm ± 2.68 µm, with 96.35% of particles being between 5 µm and 20 µm (**Figure 1**b). SEM images of the particles (**Figure 1**c) show that homogeneous crystalloids were obtained. Commercially available particles (SBp) were also analyzed and were 73.8 nm ± 15.6 nm in diameter. Some broken microparticles can be observed revealing a hollow interior. HAp particles, unlike SBp, had a coarse surface, constructed by short needle nanoparticles (276nm by 20nm), creating numerous interstitial spaces, or mesopores, which is believed to improve the absorption of growth factors. The XRD patterns of the microparticles are presented in **Figure 1**d. The diffraction peaks at 25.8°, 28.9°, 31.7°, 32.8°, 34.0°, 39.1°, 46.7°, 49.4°, and 53.2° are consistent with those of hydroxyapatite, confirming the fabrication of hydroxyapatite particles.

XPS spectrum of the HA microparticles (**Figure 1**e) matched previously reported hydroxyapatite XPS spectrum [58]. Besides the expected Ca, P, and O peaks, a C (1s)

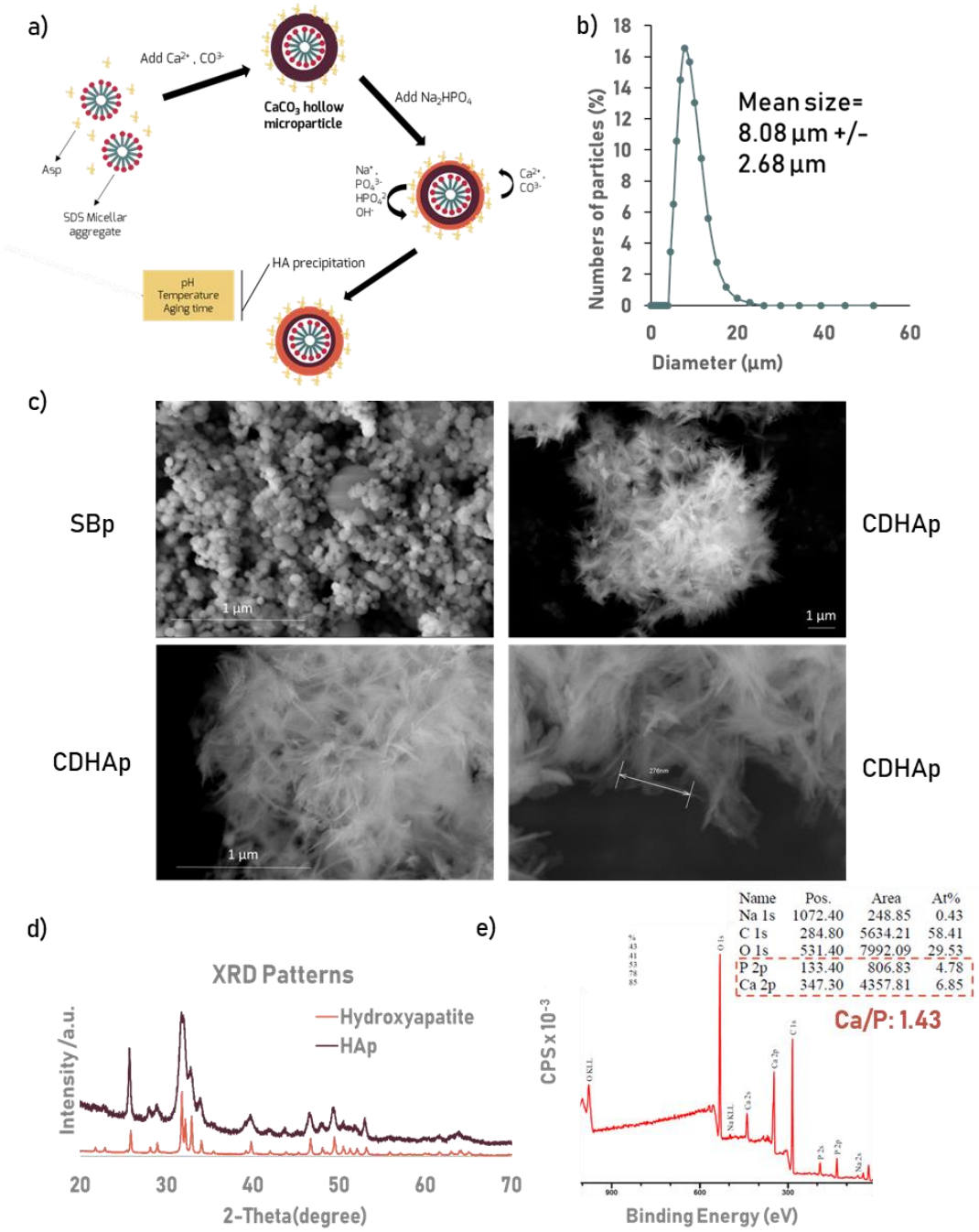

Figure 1: Hydroxyapatite Particles Characterization. (a) Hydroxyapatite particles (HAp) were synthesized in a two-step reaction. Aspartic acid and sodium dodecyl sulfate were used as surfactant to form hollow calcium carbonate (CaCO3) template. HA was then form by an anion exchange between CaCO3 and disodium phosphate dodecahydrate (Na2HPO4, 12H2O) under constant stirring (b) Particles size distribution. Average diameter is 8.08 µm ± 2.68 µm. 96.35% of particles' diameter is with the range of 5-20 µm. (c) SEM images of the particles show that homogeneous crystalloids were obtained. HAp particles, unlike SBp, had a coarse surfaces, constructed by short needle nanoparticles creating numerous interstitial spaces (d) XRD patterns of the synthesized microparticles and hydroxyapatite (PDF 01-070-4465). (e) XPS spectrum of the HA microparticles matched previously reported hydroxyapatite XPS spectrum. Besides the expected Ca, P, and O peaks, a C (1s) peak was observed. Ca/P indicates that HAp are calcium deficient.

peak was observed. Carbonate is a common impurity found incorporated into various synthetic calcium phosphates during synthesis, due to the presence of CO2 in the air and solutions. The Ca/P values were calculated directly from XPS data and were on average 1.36 ± 0.08. Stoichiometric hydroxyapatite has a Ca/P ration of 1.67, indicating that the HAp are calcium deficient. Bone is actually constituted of nano-crystalline, non-stoichiometric, calcium-deficient apatites whose Ca/P molar ratio can go from 1.33 up to 1.67 [59]. Calcium-deficient hydroxyapatite (CDHA) appears biologically more active than HA. Structurally and physically, they are unstable and very reactive due to a lower Ca/P ratio hence a higher solubility [60]. Several hydroxyapatite parameters can affect the cellular activity: its composition, dissolution, topography and surface energy. For example, a clear link between dissolution rate and early bone formation in vivo and the osteogenic differentiation in vitro of osteoprogenitor cells has been demonstrated, suggesting the influence of free calcium and inorganic phosphates on bone formation [61]. Osteoblasts have also be shown to be sensitive to the crystal shape: large apatite crystals induced more bone sialoprotein and osteocalcin expression after 3 weeks of culture than small apatite crystals [62]. This would suggest that the CDHA particles, whose composition and structure are very close to the natural bone mineral, could be of greater biological interest than stoichiometric, commercially available HA and a suitable candidate for bone regeneration [63,64].

Finally, HAp was suspended, alongside MSCs in a collagen gel, and co-cultured for 24h. Gels containing cells but no HA were used as a control. Brightfield images of the gels (Figure 2b.) showed that while HAp seemed well uniformly distributed throughout the gel, SBp aggregated and formed larger structures (black). A fluorescent

viability stain was performed on the scaffolds at the end of the culture period (Figure 2a), where green represents viable cells and red stains dead cells. The image displays high cell viability after encapsulation of the cells and microparticles in scaffolds. Viability was not affected by the incorporation of HAp.

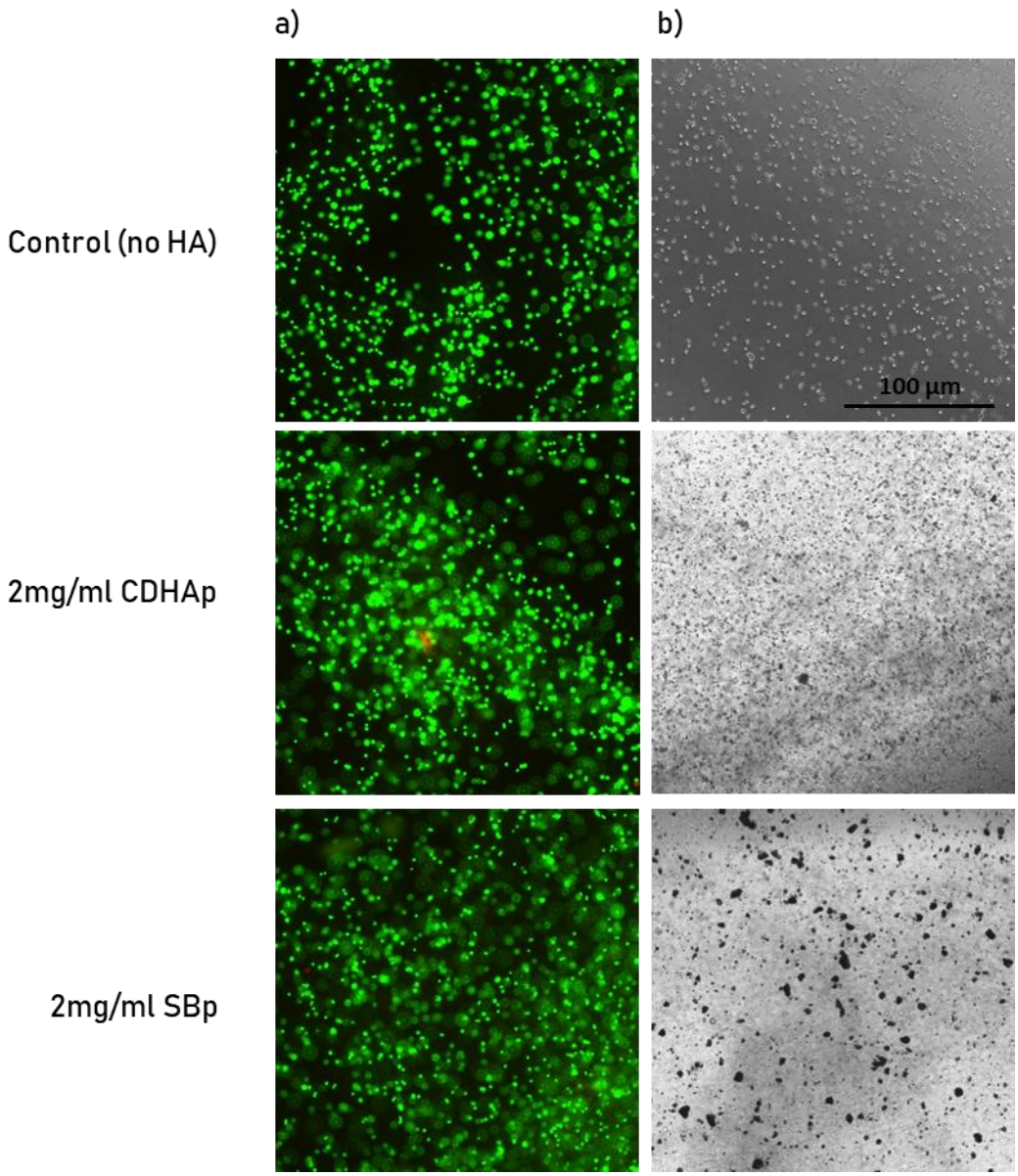

Figure 2: Hydroxyapatite Particles Characterization (2). (a) Cell viability after 24h of culture with either HAp or SBp. Green represents viable cells and red stains dead cells. The image displays high cell viability after encapsulation of the cells and microparticles in scaffolds. (b) Brightfield images of the gels showed that while HAp seemed well uniformly distributed throughout the gel, SBp aggregated and formed larger structures (black).

Osteogenic Potential of Calcium Deficient Hydroxyapatite Microparticles.

MSCs are the most commonly used stem cells because of their beneficial properties: they are easily accessible, easily expandable, have a stable phenotype and respond appropriately to the bioactive factors with subsequent production of the typical osteogenic markers [65]. Osteoblastic differentiation of hMSCs encapsulated in collagen with either CDHAp or SBp was assessed and compared to that of hMSCs in pure collagen to determine the effect of the microparticles.

After 14 days of in vitro culture, cells were retrieved and DNA was collected. The DNA quantification assay showed no significant difference between groups at day 0 ($p=0.997$). After 14 days of culture in osteogenic media, a significantly lower ($p<0.05$) DNA concentration in the samples containing CDHAp compared to the samples containing SBp or no HA (**Figure 3**a) was found. However, XTT results (normalized to DNA content) showed a significantly increased metabolic activity at D14 ($p<0.05$)) for the cells cultured with CDHAp when compared to the two other groups (**Figure 3**b). These results could suggest that hMSCs cultured with CDHAp are less proliferative but more differentiated than hMSCs grown with SBp. Research suggests that proliferation and differentiation show an inverse relationship: differentiation usually coincides with proliferation arrest [66,67]. In addition, Shum *et al.* demonstrated that metabolic activity is increased during osteogenic differentiation of MSCs [68]. Active oxidative phosphorylation is likely required to meet high ATP demands needed for extensive biosynthesis of extracellular matrix protein during osteogenesis.

mRNA expression of BMP2 and OCN was also used to monitor osteogenic differentiation. Rt-PCR showed an increase in gene expression of BMP2 and OCN in

MSCs cultured with both HAp (CDHAp and SBp) after 14 days (**Figure 3**c). A significant increase in fold change ($p<0.05$) in mRNA of both osteogenic markers was observed in the CDHAp group. Both BMP2 and OCN was described as a late marker of developing osteoblasts appearing with matrix mineralization and was at its maximum expression after 21 days post osteogenic induction [69]. Therefore it would appear that MSCs grown with CDHAp are at a later stage of osteogenesis.

During osteogenic differentiation, hMSCs will increase their deposition of minerals in the extracellular matrix (ECM). Therefore, Von Kossa staining was performed to study the mineralization and calcification of the collagen scaffolds, indicative of the stage of osteoblastic differentiation. Cross-sectional images of collagen scaffolds cultivated until day 14 and stained with Von Kossa are shown in **Figure 3**d. Mineralization, seen in dark brown/black, was minimal in no HA culture groups on day 14 and appeared the most intense in CDHAp groups.

Using evidence from cellular metabolic activity and gene expression results as well as Von Kossa staining, we can conclude that overall, the coculture of hMSCs with CDHAp resulted in greater osteogenic differentiation, compared to control and SBp. Additionally, this suggests that calcium deficient hydroxyapatite is more biologically relevant and improve osteogenesis when compared to hydroxyapatite.

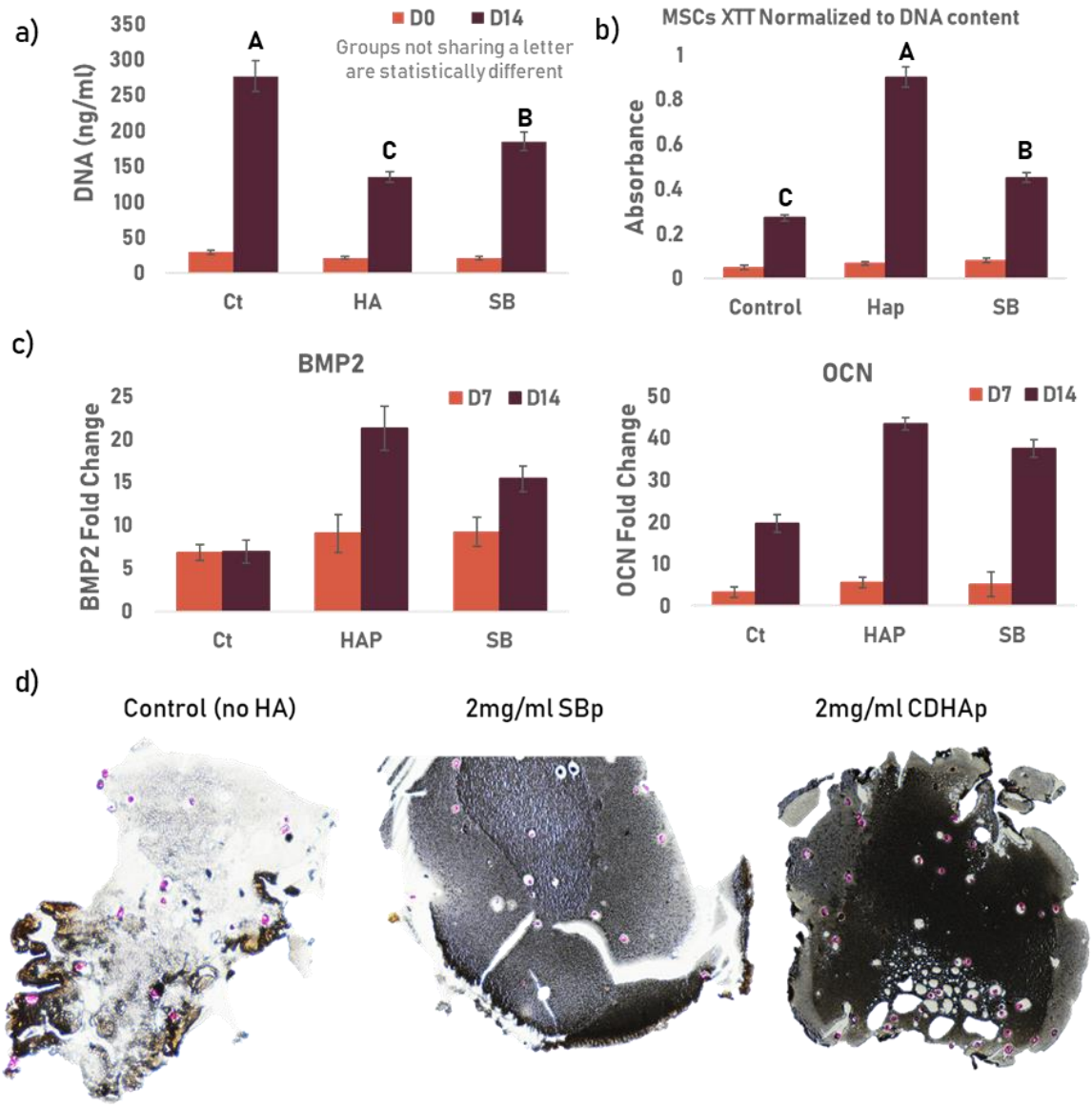

Figure 3: Osteogenic Potential of CDHAp. Ct: control group, HAp: 2ml/ml CDHAp and SB: 2mg/ml commercially available HA (Sigma). (a) After 14 days of culture in osteogenic media, a significantly lower ($p<0.05$) DNA concentration in the samples containing CDHAp compared to the samples containing SBp or no HA (b) Metabolic activity of cells after o and 14 days of culture. The results are normalized to DNA content. Results showed a significant increase in metabolic activity at D14 in the CDHAp group. (c) mRNA fold change for BMP2 and OCN after 7 and 14 days of culture. Rt-PCR showed an increase in gene expression of BMP2 and OCN in MSCs cultured with both HAp (CDHAp and SBp) after 14 days (d) Von Kossa histology staining shows great calcification (black) in SBHAp cells on Day 14 compared to SBp. Cells are stained pink.

VEGF Encapsulation and Bioactivity of CDHAp

Synthesized calcium deficient hydroxyapatite particles have the potential to be employed as a drug vehicle with high drug loading and efficiency. To demonstrate these advantages, the drug loading and release capabilities of CDHAp have been evaluated. **Figure 4**a summarizes the drug loading efficiency of both CDHAP and SBp. The CDHAp showed a high VEGF loading efficiency of 64.88 % ± 4.82 %, which was significantly higher than the loading efficiency of SBp. This suggests that the inner hollow space and the mesoporous structures at the surface of CDHAp plays an important role in improving the specific surface area and therefore enhancing the loading efficiency. Because the initial concentration was considerably high, VEGF was most likely primarily absorbed onto HAp surface through ionic affinity and then were able to pass through the channels between needle-like nanoparticles and into the hollow space serving as a reservoir.

A release study of the encapsulated VEGF into PBS was performed to evaluate the sustained release of growth factors from the microparticles. A burst of about 40% (1557 pg/ml) of VEGF from CDHAp was observed during the first 24h, followed by a more gradual and linear release over the following 14 days, during which 88% (3425 pg/ml) of the entire amount of VEGF was released. Under the same condition, 80% VEGF (814 pg/ml) was release from SBp after 24h, and about 93% (946 pg/ml) of the initial VEGF concentration was released after 14 days. Compared to SBp, CDHAp hollow core could also play an important role in reducing the drug release and assuaging the initial burst release of VEGF. The hollow interior could serve as a drug reservoir, maintaining a constant release rate. Comparing the release profiles of CDHAp with

SBp, the trend observed was that CDHAp released their cargo much slower than SBp, which prolong the drug's effect. One day after the beginning of the release study, CDHAp had release significantly ($p<0.05$) less VEGF than SBp: 41.2% of total encapsulated VEGF for CDHAp versus 86.1% for SBp.

The angiogenic potential of CDHAp was assessed and compared to that of SBp. HUVECs were suspended in collagen gels, along with either SBp or CDHAp. Both microparticles were loading with VEGF. No HA particles were used as a control. After 7 days of in vitro culture, cells were retrieved from the scaffolds and DNA was collected. The DNA quantification assay showed no significant difference between groups at day 0 ($p=0.185$). After 7 days of culture, a significantly higher DNA concentration ($p<0.05$) was found in the samples containing CDHAp compared to the samples containing SBp (**Figure 4**b). Similarly, XTT results (normalized to DNA content) showed a significantly increased metabolic activity at D7 ($p<0.05$) for the cells cultured with CDHAp when compared to the two other groups (**Figure 4**c).

mRNA expression of PECAM and VEGF was also used to monitor angiogenesis. Rt-PCR showed an increase in gene expression of both PECAM and VEGF in HUVECs cultured with both HAp (CDHAp and SBp) after 7 days (**Figure 4**d). A significant increase in fold change in mRNA ($p<0.05$) of both osteogenic markers was observed in the CDHAp group. A set of experiments was conducted to investigate the ability of VEGF-CDHAp to stimulate the migration of HUVECs (**Figure 4**e). HUVEC migratory activity when cultured with CDHAp increased when compared to SBp. Quantification of the invaded area indicated that wound closure was significantly higher when HUVECS were supplemented with CDHAp rather than SBp ($p<0.05$). Altogether,

these results indicate the superior ability of CDHAp loaded with VEGF to promote angiogenesis.

Conclusion

In the present study, we demonstrated the successful fabrication of calcium deficient hydroxyapatite microparticles, with biological properties closer to bone than stoichiometric, commercially available hydroxyapatite. These CDHA particles exhibit a well-defined 3D network of crystalline nanoplates forming mesoporous and hollow structures. The high specific area created by those structures enabled the loading of VEGF with high efficiency when compared to the loading efficiency of SBp. The high loading efficiency of VEGF and its sustained release property suggest that the HCHAs have the great potentials for bone-implantable drug-delivery applications. Furthermore, their biological performances were evaluated in vitro. Our results indicate that VEGF-CDHAp can be used to improve both osteogenesis and angiogenesis, as evidenced by upregulation of osteogenic and vasculogenic genes, and an increase in matrix mineralization. The system developed in this study could be used to deliver not only VEGF but multiple bioactive growth factors and could find broad utility in many bone tissue engineering applications where sustained release of factors in a local environment is advantageous.

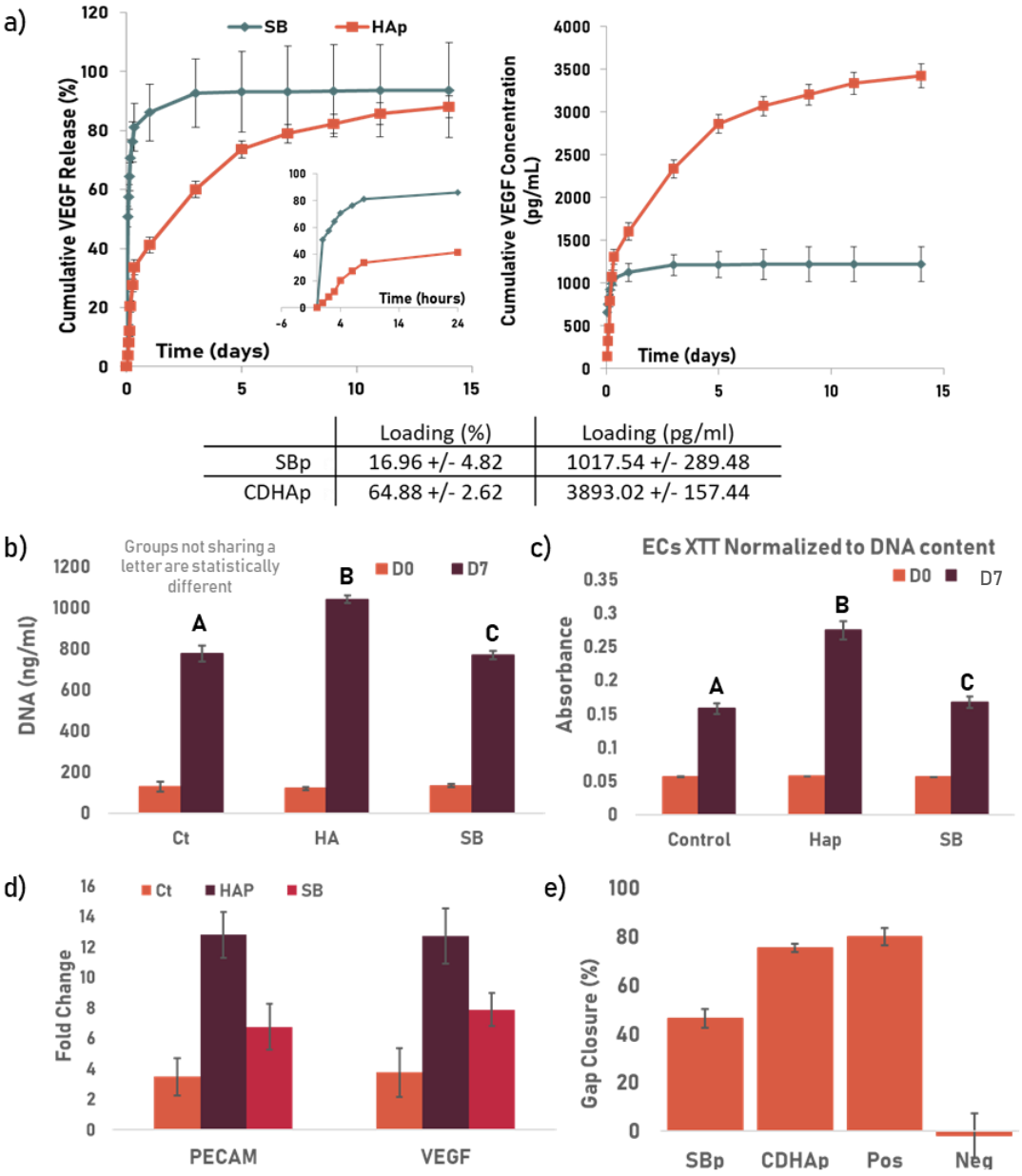

	Loading (%)	Loading (pg/ml)
SBp	16.96 +/- 4.82	1017.54 +/- 289.48
CDHAp	64.88 +/- 2.62	3893.02 +/- 157.44

Figure 4: VEGF Release and CDHAp Bioactivity. Ct: control group, Hap: HA: 2ml/ml CDHAp and SB: 2mg/ml store bought HA (Sigma). (a) Release profile of VEGF from SBp and CDHAp. The insert in the first graph shows the first 24h of release. The table summarize the loading efficiency for both particles. (b) DNA quantification after 0 and 7 days of culture. After 7 days of culture, a significantly higher DNA concentration was found in the samples containing CDHAp compared to the samples containing SBp (c) XTT results (normalized to DNA content) showed a significantly increased metabolic activity at D7 for the cells cultured with CDHAp when compared to the two other groups (d) mRNA expression of PECAM and VEGF was also used to monitor angiogenesis. Rt-PCR showed an increase in gene expression of both PECAM and VEGF in HUVECs cultured with both HAp (CDHAp and SBp) after 7 days. A significant increase in fold change in mRNA of both osteogenic markers was observed in the CDHAp group. (e) Migration assay. Quantification of invaded area indicated that wound closure was significantly higher when HUVECS were supplemented with CDHAp rather than SBp.

Chapter 3: Cell-Laden 3D Printed Scaffolds for Bone Tissue Engineering[1]

Introduction

Bone tissue engineering has emerged as a promising technique to fabricate biological substitutes [70]. Cells play a central role in bone regeneration; non-tissue, acellular materials will lack the abilities of resorption, secretion, and mineralization. Cellular strategies in bone tissue engineering play an important role, and proof of concept models have been previously demonstrated [71–78]. However, cells require mechanical support and a physical template, or scaffold to facilitate their attachment and to stimulate neotissue formation. Such scaffolds should mimic the native ECM. Mechanical strength and architecture are important scaffold parameters; high interconnectivity between pores enabling nutriment and oxygen transport as well as pores size of at least 300μm have been showing to enhance bone formation and vascularization [79–81]. Porous bone scaffolds have been made using different techniques, such as particle/salt leaching [82], gas foaming [83], freeze drying [84], and phase separation [85]. However, those approaches cannot allow full control over the pore size, porosity, interconnectivity, and specific shape of the scaffold. Addressing those limitations, additive manufacturing (AM) has emerged in recent years as a promising method for the fabrication of porous scaffolds, providing accurate and precise architecture. The

[1] Adapted from CM Piard, Y Chen, JP Fisher, "Cell-laden 3d printed scaffolds for bone tissue engineering". Clinic Rev Bone Miner Metab (2015) 13: 245.

first example of AM, called stereolithography, was introduced in 1986 by Chuck Hull and involved thin layers of material sequentially printed and cured with ultraviolet light to form a solid structure. Currently, several other 3D printing approaches are used to fabricate scaffolds directly from a computer-aided design file (CAD), such as rapid prototyping and solid freeform fabrication, allowing scaffold [86]. Taking AM technologies a step further, bioprinting allows the direct and precise deposition, layer by layer, of biological materials, cells, and biochemicals. Several technologies are been developed to fabricate 3D functional living structures, including inkjet bioprinting, microextrusion, and laser-assisted printing [87]. 3D porous bone scaffolds fabrication has developed and investigated, both by standard AM approaches and by 3D bioprinting, as shown in Table 1 [88,89,98,90–97].

In bone tissue engineering, the presence of viable cells inside a graft has been shown to enhance bone formation *in vivo*, as cells not only participate in ECM formation but also stimulate bone remodeling using paracrine signals [99,100]. Cells are typically incorporated into AM fabricated constructs using one of two different strategies, as described in . The first strategy, 3D bioprinting, involves the layer by layer deposition of a bioink, made of a scaffold material and cells. The second strategy focuses on the fabrication of a scaffold by printing an acellular material, following by a post-treatment to remove cytotoxic crosslinking agents and to sterilize the scaffolds before seeding living cells. Here, we review both approaches, focusing on fabrication techniques and scaffold materials. Then we will describe and discuss the properties of the resulting constructs in term of mechanical properties, ECM production, and mineralization, and finally, consider the advantages and limitations of each approach.

3D Bioprinting of Cell-Laden Hydrogels

3D Bioprinting Techniques

The main technologies used in 3D printing are inkjet and microextrusion [87]. Bone 3D printing is mostly extrusion-based [89–95]. This approach uses a three-axis dispensing system, which builds 3D constructs by extruding fibers of cell-laden biomaterials in a layer-by-layer fashion, as directed by CAD software. The most common method to extrude fibers is by applying pressure from a compressed gas. The construct, if necessary, is chemically or UV-crosslinked to maintain the structural integrity of the fibers. The main advantage of microextrusion is the ability to deposit very high cell densities. Inkjet printing has also been adapted to printing bone grafts [88]. This technology relies on the ejection of drops of liquid onto a substrate due to thermal or acoustic forces. It provides excellent printing resolution, with controlled volumes of liquid being delivered to predefined locations.

Cell viability after undergoing microextrusion has been shown to be lower than when using an inkjet printer. Several dispensing parameters impact cell viability such as the extrusion pressure, the dispensing nozzle diameter, and length, and the nozzle head speed. Among those parameters, the extrusion pressure has been shown to have the most significant effect on cell viability [101]. Cell survival rates using microextrusion range from 40 to 86%, and decrease as the extrusion pressure increases, a phenomenon likely due to shear stress [101,102]. Cell viability is important as cell must be not only alive but also keep their specific function, i.e. producing and mineralizing bone matrix.

However, it has been shown that initial cell damages due to printing may be reversible with time [102].

One of the most significant challenges with 3D bioprinting is determining the appropriate material that will provide the right structural and mechanical properties for a bone graft. This material, in addition to being biocompatible and biodegradable, must protect the cells from damage during printing and allow them to proliferate, differentiate, and produce their own ECM post-printing. The material must also be suitable for the printing techniques described above, with suitable crosslinking mechanisms to facilitate the printing process and the controlled and precise deposition of the cells.

Hydrogels are highly hydrated materials composed of hydrophilic polymers that are crosslinked to form three-dimensional networks [103]. They are popular materials for bioprinting, as they are able to undergo a phase transition from liquid to gel based on thermal or chemical cues [104]. Their structure is morphologically similar to that of natural ECM due to their high water content, and they have shown excellent biocompatibility and biodegradability [105]. Hydrogels are widely used to encapsulate cells, enabling them to exhibit phenotypes more similar to those *in viv*o than when the cells are grown in monolayer culture [106,107]. Currently, the main hydrogel materials used in 3D bioprinting for bone tissue engineering are based on natural polymers such as alginate and gelatin, or synthetic molecules such as poly(ethylene glycol) (PEG). These materials fit the previous criteria and are abundant and less expensive than synthetic polymers.

Printing With Naturally Derived Polymers

Alginate remains one of the most widely used natural materials for cell-based hydrogel printing of bone substitute [108–110]. It is a polysaccharide, a polyanionic linear block copolymer containing blocks of (1,4)-linked β-D-mannuronic (M block) and α-L-guluronic (G block) acids. When dissolved in an aqueous medium, alginate forms a hydrocolloid, which gels under gentle conditions induced by multivalent cations, such as Ca^{++}, and therefore the hydrogel is characterized by excellent cells compatibility [111]. Alginate is characterized by a wide pore size distribution (5–200 nm), explaining an important diffusion rate of large molecules in and out of the gel [111]. Alginate has also demonstrated the capacity to support cellular function and differentiation *in vitro*, including bone formation [112–115].

One of the main problems with printing alginate is overcoming its low viscosity. A low viscosity usually leads to the collapse of deposited structures during printing, and directly influences shape fidelity post printing [116]. Increasing alginate concentration is a common approach to improve its printability [117]. Another approach is to use a combination of alginate with a second biopolymer during scaffold fabrication. The addition of gelatin can enable fast solidification of the 3D structure, as it acts as a short-term stabilizer. Gelatin is composed of acid-denatured collagen, the main component of native ECM. Due to its biocompatibility and rapid biodegradability, it has been used for drug release and tissue engineering due [118,119]. Gelatin gelation is solely based on physical intermolecular interaction of the gelatin molecules and the resulting gels are not stable under physiological temperature [120]. After methylation of gelatin, gelatin

methacrylate (GelMA) is a photocurable material and can be used as a bioink in 3D bioprinting [120,121]. Schütz *et al*. used methylcellulose, a water-soluble derivative of cellulose, in combination with alginate to form a viscous solution in water [93]. Methylcellulose does not contribute to the gelation and is released from the printed construct after crosslinking. Long-term stability is provided by the alginate, and the loss of the second polymer has no impact on geometry, nor does it increase the scaffold's microporosity [94,122]. To this end, porosity has been shown to substantially impact scaffold mechanical properties [79].

In addition to understanding the viscosity and flow properties of the material, mechanical properties of the scaffold must be considered; in general, hydrogels are too soft for load-bearing defects [123]. Alternative strategies to enhance their biological and mechanical properties have been developed for printing composite biomaterials by combining stiff materials with mechanically-weak hydrogels, or by suspending particles with bioactive potential into the hydrogel matrix. Wang *et al.* showed that a cell-laden alginate/collagen matrix could be supplemented with particles of bioglass, a well-established, hard, porous material used in the fabrication of bone replacement scaffolds [124,125], in order to render the material stiffer and stimulate cell growth and mineralization [91]. Microcarriers (MCs) are particles that promote attachment, homing, and survival of cells, and their encapsulation in hydrogel matrices has been shown to increase the mechanical strength of the gel [126127]. Osteoblasts cultured on MCs have been found to better retain their phenotype and display greater potential to regenerate bone [128]. Levato *et al.* incorporated MCs in GelMA bioink and showed that not only the mechanical properties were increased two-fold when compared to gels without

MCs, but also differentiation of hMSCs improved [92]. Wüst *et al.* used a combination of gelatin, alginate, and hydroxyapatite (HA) to improve the mechanical stiffness of the hydrogel [94]. HA has been shown to be osteoconductive and enhance cell attachment, guiding osteogenic differentiation *in vivo* [108,129].

Bioprinting With Synthetic Polymers

However, even composite hydrogels based on natural polymers still have low stiffness (in kPa range) when compared to bone (in the GPa range) (Table 1). Greater stiffness can be achieved by using synthetic polymers and molecules. Gao *et al.* used PEG-GelMA hydrogels for inkjet printing of bone constructs [88]. They showed improved mechanical properties compared to GelMA-only scaffolds, with a reported modulus of 1-2 MPa. Poly(L-lactic-*co*-glycolic acid) (PLGA)-PEG-PLGA hydrogels have also been used to print scaffolds [95]. In this case, even greater stiffness was achieved, with a modulus between 54.4 and 57.3 MPa; while this is within the range of cancellous bone, it is still lower than moduli obtained in other bone tissue engineering studies. Synthetic polymers are the most commonly used polymers for 3D printing in bone tissue engineering. However, harsher conditions, such as exposure to extreme temperature, pressure, or pH, are usually involved in the printing process, and the direct incorporation of cells is generally avoided [130,131]. In this scenario, the cells are seeded onto the scaffold after fabrication.

Cell Seeding on 3D Printed Scaffolds

Rapid Prototyping Techniques for Scaffold Fabrication

Layer-by-layer scaffold fabrication techniques based on rapid prototyping methods include stereolithography (SLA) [132], 3D printing (also called melt plotting) [133], selective laser sintering (SLS) [134], fused deposition modeling (FDM) [135] and direct writing [136]. With SLA, scaffolds are formed by immersing a platform in a liquid polymer. Exposure to focused light, according to a desired design, crosslinks and solidifies the polymer at the focal point. As the platform moves upward or downward, the scaffold is created. The same principle is applied to SLS, where powders are added and sintered using a laser source. 3D printing, FDM, and direct writing involve layer-by-layer extrusion at a constant rate and under a specific pressure. 3D printing is based on the deposition of strands of viscous material in solution, while FDM uses heated polymers/ceramics, and direct writing uses liquids. In direct writing, the solidification of the scaffold is achieved through a liquid-to-gel transition. These techniques present advantages and disadvantages, as discussed extensively in previous reviews [86]. Briefly, 3D printing, due to mild processing conditions, allows the incorporation of biomolecules and drugs, but it is still limited by the post-processing methods required for some materials. As SLA requires the use of focused light, only photopolymers can be used; however complex internal features can be obtained. With SLS, no post-processing is needed, but the resolution of scaffold features depends on the diameter of the laser used. Direct writing enables a precise control on thickness. SLS, FDM, and direct writing do not require a supportive platform. Depending on scaffold composition and inherent material properties – including melting temperature, crosslinking or

solidification mechanism, and solution homogeneity – a specific technique may be more amenable than others when printing scaffolds for bone tissue engineering.

Ceramics And Polymers

A broad range of ceramics (calcium phosphates [137,138] or bioactive glass [139]), polymers (poly(ε-caprolactone) (PCL) [140,141]), or composite materials [142,143] have been successfully used for 3D printing. Ceramics are the gold standard for repairing bone voids, as they have good biocompatibility and have been shown to be osteoconductive [144]. Ceramics include calcium phosphates, bioactive glass, and bioactive compounds of glass and ceramic [145]. Calcium phosphates, like biodegradable tricalcium phosphates (TCP) and hydroxyapatite (HA), are among the most studied ceramic materials [144]. Due to the formation of iron-rich cellular microenvironment, ceramics have the ability to upregulate osteogenesis. Moreover, their degradation rate has been shown to be lower than hydrogels, allowing for prolonged structural support and guided neotissue formation [130]. SLS is commonly used for ceramics 3D printing. Scaffolds with a high HA content, superior to 50% w/v, have been successfully fabricated [146]. The effect of pores size on osteoblasts was studied on 3D printed TCP scaffolds, showing that a decrease in pore size from 1000 to 750µm resulted in an increase in cell density and proliferation [147]. TCP 3D printed scaffold have also been shown to promote osteogenesis in a rat femur model [148].

Polymers represent other promising materials for bone tissue repair as they provide mechanical strength, are easy to fabricate, cost-effective, biocompatible, and have

tunable degradation characteristics [149]. The polymers most commonly used for 3D printed bone scaffolds include PCL, poly(lactic acid) (PLA) [150], poly(glycolic acid) (PGA) and its co-polymer poly(lactic-co-glycolic acid)(PLGA) [98], poly(methyl methacrylate) (PMMA), polyethylene (PE) [151], and poly(propylene fumarate) (PPF) [152]. FDM techniques have been used to fabricate PCL scaffolds [153,154]. Reichert *et al.* printed a composite material made of PCL and 20% w/v of TCP, extruding filament of 300 μm diameter forming scaffolds with a 70% porosity and an elastic modulus of 22.2 MPa [154]. *In vivo* implantation showed a significantly greater bone formation and mechanical strength when compared to the gold standard, autologous grafts. Wang *et al.* fabricated PPF scaffolds using SLA and showed that their compressive modulus was in the range of bone and that they provided mechanical stability while degrading without inducing any cytotoxic response [155].

As with hydrogels, these polymers have also been paired with bioactive molecules in order to improve scaffold mechanical or biological properties. Furthermore, molecule release and surface properties of the material play an important role in stimulating cell interaction, differentiation, and infiltration throughout the 3D printed bone scaffold [156]. Lee *et al.* used stereolithographic PPF scaffold as a delivery vehicle for PLGA microspheres containing BMP-2 [157]. They were able to fabricate scaffolds that maintained an interconnected network of pores and showed improved cell differentiation *in vitro*. Gonçalves *et al*. used carbon nanotubes (CNTs) in combination with PCL-HA scaffolds in order to achieve polarized and conductive surface properties [97], as it has been shown that electrical stimuli enhance cell function [158]. They showed

that cell adhesion and proliferation was improved in CNT scaffolds due to the formation of an apatite layer on the surface.

Cell-Biomaterial Interactions

Another important point to consider when seeding cells on a 3D printed scaffold are the cell-biomaterial interaction, which plays an important role in the growth and differentiation of cells on the scaffold's surface [156]. Surface properties of scaffolds can be tuned to improve cell adhesion, proliferation, and differentiation after its attachment on the surface [159,160]. Different methods, such as physical adsorption or covalent conjugation, have been investigated to modify scaffold surfaces. For example, PCL surface characteristics are not favorable for cell adhesion and proliferation, as it is a hydrophobic polymer and lacks a bioactive functional group [161]. Seydnejad *et al.* developed a modified PCL, poly(hydroxymethylglycolide-co-caprolactone), to increase its hydrophilicity and allow tuning of the degradation rate and hydroxyl groups to enable surface functionalization with peptides [133]. Their results showed that metabolic activity of the cells was significantly enhanced, and cells differentiated toward osteogenic lineage when compared with PCL scaffolds. Kao *et al*. 3D printed PLA scaffolds and used a surface coating of poly(dopamine) (PDA), which, due to amine functional groups, has the ability to attach to various hydrophobic surfaces via self-polymerization to improve cell attachment and differentiation [162]. An increase in cell adhesion and proliferation was observed, due to improved surface hydrophobicity, when compared to unmodified PLA scaffolds. More osteogenic differentiation, as well as angiogenesis, was also observed. Kuo *et al.* functionalized PLGA/chitosan scaffolds

with type I collagen and were able to improve MSC adhesion and viability on PLGA/chitosan scaffolds, as well as direct differentiation towards osteoblastic lineages [163].

Once the cell-based construct is fabricated, either a cell-laden printed hydrogel or a scaffold seeded, it needs to either be implanted in vivo or pre-cultured in vitro. However, the 2D in vitro culture of a 3D construct presents some hurdles. The cells within the construct receive a limited amount of glucose, nutrients and oxygen, which results in cells death [164]. In response to this problem, bioreactors systems have been developed to optimize in vitro culture. It has been demonstrated that bioreactor, in particular, perfusion system, effectively perfuse media throughout a porous 3D construct and enhance nutrients transport [165]. By exposing the cells to fluid shear stress, bioreactors have even been shown to improve upregulate the expression of osteoblastic markers and mineralization of the ECM [166].

3D Bioprinting vs Cell Seeding on a Printed Scaffold

Cell-laden 3D printing scaffolds present several advantageous proprieties when compared to standard fabrication techniques. Their use enables precise positioning of cells and biomaterials, tunable mechanical properties, fine control of the external and internal architecture. Moreover, it allows for scalable and patient-specific fabrication of complex designs. However, both approaches using cells alongside 3D printing described previously are unable to satisfy all those criteria at once. Each technique has its own advantages and limitations.

Mechanical Properties

When comparing cell printing versus cell seeding post-printing, the resulting mechanical integrity and compressive modulus of the printed construct are different. For example, hydrogels are mainly used for cell printing but have lower mechanical strength than printed polymer and ceramic scaffolds. 3D bioprinted constructs, based mostly on hydrogels, have a very low stiffness (in kPa range) when compared to bone, even after improvement of the materials as described previously. In addition, it is known that crosslinked alginate loses its mechanical integrity over time due to an outward flux of ions [167]. Compared to native tissue, the compressive modulus of cancellous bone is approximately 244 MPa, while that of cortical bone is a degree of magnitude lower – about 17 MPa [168,169]. It has been shown that cells can act as a reinforcing material to hydrogels; as they differentiate, and mineralization of the ECM appears, the modulus of the gel can increase by up to 100% [88,92]. Even in this case, the stiffness is still too low to match that of bone. However, the use of synthetic polymers and rapid prototyping enables the fabrication of scaffolds with compressive modulus from 4-77.2 MPa (Table 1), which is in the range of cancellous bone. The higher values in this range could, however, be related to the scaffold porosity as it is directly connected to mechanical strength [170]. Finally, in particular cases of non-load bearing defects, mechanical properties may not be the main concern, as it might not be necessary to provide implants with the original biomechanical properties of bone since the scaffold is meant to be completely remodeled.

Macro- and Microporosity

One of the main challenges in the fabrication of a cell-laden hydrogel scaffold is the generation of 3D constructs with relevant size and of high accuracy with respect to the predefined shape, porosity, and inner pore structure. On the contrary, when printing polymer or ceramic scaffolds prior to cell seeding, complex internal features can be obtained with a good resolution due to the better structural integrity of the fibers or struts. Pore size and porosity not only affects the mechanical characteristics of a scaffold but also cell behavior. Tarafder *et al.* studied the effect of pore size on osteoblasts using sintered 3D printed tricalcium phosphate (TCP) scaffolds and showed that lower pore size resulted in an increase in cell density, good cell adherence, and cell ingrowth into the pores [147]. 3D printed TCP samples with macro- and microporosity also facilitated osteogenesis in a rat femur [148]. In addition, the presence of micropores within macropore walls has been indicated as a method to make the material osteoinductive [171]. With the optimization of 3D bioprinting techniques, it may become possible to create pores in the appropriate range for supporting bone tissue regeneration *in vitro* and *in vivo*.

Cell Distribution and Integration Within the 3D Printed Scaffold

3D bioprinting of cell-laden hydrogels may not exhibit as intricate designs as scaffolds printed prior to cell seeding, but it allows control of cell distribution and cell density within the graft by incorporating cells directly in the printed material. Among other hydrogel printing techniques, inkjet printing has the capacity to create a concentration gradient of cells, materials, or growth factors throughout the 3D structure of the

scaffold [172]. 3D bioprinting also enables the deposition of multiple cell types in the same construct. Fedorovich *et al.* used this technique to improve the vascularization of a bone construct by printing two different hydrogels loaded with endothelial progenitor cells (EPCs) or MSCs. After 6 weeks of implantation, they showed bone formation in cell-laden gels, as well as tubular structures and erythrocytes in some of the lumina [173]. The multiple printed cells retained their functionality and produced ECM according to their respective cell type. While hydrogels expose cells to a highly hydrated 3D microenvironment that closely resembles the natural ECM [174], the majority of hydrogels used for 3D bioprinting only provide the cell with a non-interactive encapsulation matrix, a template to permit cell localization but lacking any surface modification to promote cell attachment and migration [103]. Strategies to seed cells rather than embed them provide an alternative to more freely promote cell motility in a bone scaffold. Due to high temperatures or pressures, rapid prototyping techniques for printing polymers and ceramics do not allow the exact deposition of cells in the scaffold. As a result, cells that are then seeded on the porous scaffold often remain on its periphery. The promotion of cell migration to the center of the scaffold may then rely on other external cues, such as surface modification, signaling from bioactive molecules, or even flow perfusion [165].

One of hydrogels other advantages is the ability to expose cells to a highly hydrated 3D microenvironment that closely resemble the natural ECM [174]. However, the majority of hydrogel for 3D bioprinting only provide the cell with non-interactive encapsulation matrix, acting as a template to permit cell localization but lack of any surface modification to promote cell attachment and migration [103].

Conclusions

Two techniques for bioprinting and incorporating cells have been highlighted for bone tissue engineering: 1) 3D bioprinting of cell-laden hydrogels, and 2) seeding cells onto 3D printed polymeric or ceramic scaffolds. While direct embedding of the cells during scaffold fabrication can lead to a high seeding density, uniform distribution, and spatial control of one or more cell types, the materials used – mostly hydrogel-based – do not allow for an exact and intricate design of the scaffold, as in the approach of printing and processing a polymer or ceramic-based scaffold prior to seeding. Another major problem discussed above is the lack of mechanical integrity. Even though hydrogel modifications can improve the compressive strength of scaffolds, moduli are still low. The other option, seeding cells on a 3D printed scaffold, allows the use of more stiff polymeric or ceramic materials with mechanical properties in the range of those of cortical bone. However, optimal seeding, adhesion, and proliferation of cells may require surface modification of the scaffolds. Based on currently reported methods, no single fabrication technique is able to satisfy all the requirements discussed previously. Scaffold fabrication of bone implants would ideally require the use of two printable matrices: a solid, mechanically strong, porous matrix and a softer biocompatible hydrogel into which the embedded cells can proliferate and differentiate, printed together in an intricate design. Furthermore, when designing a scaffold for bone tissue engineering, it is important to prioritize functionality over complexity. Exploiting benefits from both techniques to promote cell viability and infiltration, mechanical integrity, and proper matrix remodeling of defect tissue will result in the most functional regeneration of bone.

Table 1: Techniques Used For Inclusion Of Cells In Bone Scaffolds During Or After Printing. Examples of studies involving both cells and 3D printing for the fabrication of bone grafts are provided. The printing techniques, the type of cells used, the biomaterial printed, the results of mechanical testing and the stain used for histology of in vivo samples are summarized. *MSCs: mesenchymal stem cells, EPCs: endothelial progenitor cells, PEG: polyethylene glycol, PLGA: poly(lactic-co-glycolic acid), HA: hydroxyapatite, PLLA: poly-L-lactic acid, PPF: poly(propylene fumarate, HE: hematoxylin and eosin, OCN: osteocalcin, ALP: alkaline phosphatase , COL1: collagen 1, vWF: von Willebrand factor, αSMA: alpha smooth muscle actin.*

	Additive Manufacturing Technique	Cell	Material	Compressive Moduli	In Vitro Study	Ref
3D Bioprinting of Cells	Inkjet Printing	Human MSCs	PEG / Gelatin Methacrylate	35 kDa	No	[27]
		Human MSCs	Acrylated PEG	1 to 2 MPa	No	[38]
	Bioplotting	Goat MSCs	Alginate / Gelatin	NA	HE, OCN ALP, COL1, OCN, vWF, αSMA	[28]
		Human MSCs	Alginate	NA		[29]
		SaOS-2 cells,	Alginate / Gelatin / Silica	NA	No	[30]
		Rat MSCs	Gelatin Methacrylate / Gellan Gum	42 to 48 kPa	No	[92]
		Human MSCs	Alginate / Methylcellulose	101 kPa	No	[93]
		Human MSCs	Alginate / Hydroxyapatite / Gelatin	32 to 37 kPa	No	[94]
		Human MSCs	PLGA-PEG-PLGA	55 to 57 MPa	No	[95]
		Goat MSCs, Goat EPCs	Matrigel / Alginate	NA	ALP, COL I, vWF, αSMA	[173]
Cell Seeding Post Printing	Direct-Write Assembly	MC3T3-E1, Preosteoblasts	Gelatin / Hydroxyapatite	4 MPa	No	[96]
	3D Plotting	MG63 Osteoblast-Like	Polycaprolactone / HA	6 MPA	No	[97]
		Human Fetal Osteoblast	PLGA	77 MPa	No	[98]
		Human MSCs	Bioactive Glass / Alginate	NA	No	[124]
	Stereolithography	Human MSCs, Adipose-Derived	PLLA	NA	No	[162]
		MC3T3-E1, Preosteoblasts	PPF	NA	HE	[157]

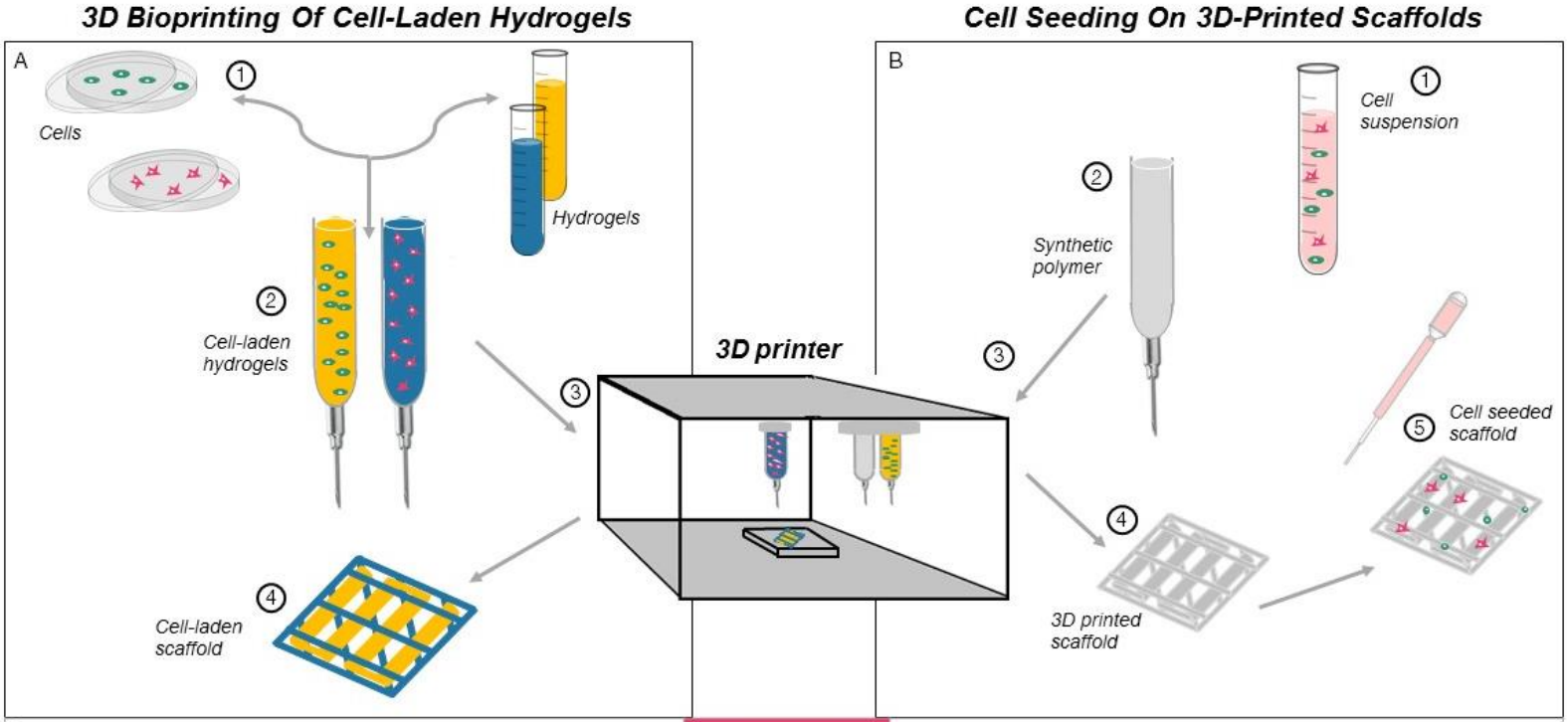

Figure 5: Strategies For The Fabrication of Cell-laden 3D Printed Scaffolds. Cells are typically incorporated into 3D printed constructs using one of two different strategies. The first strategy, 3D bioprinting (A), involves the preparation of a bioink, a cell laden hydrogel (1 and 2), and its layer by layer deposition (3). The second strategy (B) focuses on the fabrication of a scaffold by printing an acellular material (4), such as a synthetic polymer, before seeding living cells (5). Table C summarizes the advantages and limitations of each approach.

Chapter 4: Bioprinted Osteon-like Scaffolds Enhance in Vivo Neovascularization[2]

Introduction

The use of in vitro coculture of human umbilical vein endothelial cells (HUVECs) and human mesenchymal stem cells (hMSCs) has been one of the most explored options to improve neovascularization of the graft [8, 11-12]. In cortical bone, both cell populations, osteogenic and vasculogenic, are arranged in a well-defined pattern, called osteons [175]. Each osteon is composed of concentric bone-cells containing layers (lamellae) surrounding the Haversian canal, a narrow central channel, which contains small blood vessels. One attempt to recreate osteon-like structures used electrospun gelatin/PLLA rods seeded with osteoblasts [176]. However, cell infiltration in these avascular scaffolds was hindered by the tight nanofibrous network resulting in cell apoptosis.

To address this shortcoming, we present in this paper an alternative method to mimic the spatial pattern of HUVECs and hMSCs found in native osteons based on the use of extrusion-based 3D bioprinting (3DP). 3DP, as discussed in the previous chapter, offers an efficient tool for accurate fabrication of biomaterial scaffolds with tunable properties [177]. Fibrin is a natural polymer known to support wound healing by inducing angiogenesis and promoting cell attachment and proliferation, and therefore an

[2] Adapted from CM Piard, H Baker, T Kamalitdinov and JP Fisher, "Bioprinted osteon-like scaffolds enhance in vivo neovascularization". Biofabrication (2019), *in press.*

attractive matrix for stem cell differentiation and tissue engineering [178–180]. Although fibrin has shown potential in vitro in promoting osteogenesis, it lacks the mechanical strength required for bone tissue engineering [181]. The co-printing of a solid mechanically strong and porous matrix, such as polycaprolactone (PCL) along a softer biocompatible hydrogel into which the embedded cells can proliferate and differentiate is an alternative strategy [182]. PCL is biocompatible and exhibits a slow biodegradation rate that can maintain mechanical stability long enough to allow new bone formation [183].

In the present study, the overall objective was to develop a 3DP biphasic osteon-like scaffold, containing two separate osteogenic and vasculogenic cell populations encapsulated in a fibrin bioink in order to improve neovascularization. To this end, the first objective was to optimize the fibrin bioink to improve the resolution of printed fibers and ensure a reproducible printing process; the influence of printing parameters on extruded fiber diameter and cell survival was also investigated. The second objective was to improve the mechanical strength of the construct by co-printing the fibrin bioink along a supporting PCL carrier scaffold. Finally, HUVEC and hMSC laden fibrin hydrogels were printed in osteon-like patterns and cultured in vitro. Biphasic scaffolds seeded with rat aortic endothelial cells and MSCs were implanted subcutaneously in rats. Results showcase the capacity of our 3DP biphasic construct to provide accurate physical cues for large-scale vascularized bone.

Material and Methods

Cell Culture

L929 cells (ATCC, Manassas, VA) were cultured as per the manufacturer's specifications with Minimum Essential Medium (Life Technologies, Frederick, MD) and 10% horse serum (Life Technologies). Prior to printing, cells were passaged using Trypsin/EDTA and encapsulated in fibrin bioink (two densities were examined, 2x106 cells/ml and 10x106 cells/ml). hMSCs (Lonza, Walkersville, MD) were cultured in control media consisting of Dulbecco's Modified Eagle's medium (DMEM, Gibco, Carlsbad, CA) supplemented with 10% fetal bovine serum (Gibco), 1.0% v/v penicillin/streptomycin (Gibco), 0.1 mM non-essential amino acids (Gibco), and 4 mM L-glutamine (Gibco as per the manufacturer's specifications). Cells were expanded on tissue culture polystyrene flasks with media changes every 3 days and grown to 80% confluency before being passaged using trypsin/EDTA. Cells at passage P2 were used for the experiments. HUVECs (Lonza) were cultured in EBM-2 Basal Medium (Lonza) supplemented by EGM-2 SingleQuot Kit. Rat primary aortic endothelial cells (RAECs) were purchased from Cell Biologics (Chicago, IL) and cultured according to manufacturer instructions. Rat MSCs (rMSCs) were purchased from RD Systems (Minneapolis, MN) and cultured in osteogenic media for 7 days prior to implantation. The osteogenic media was formulated by supplementing growth media with 100 nM dexamethasone (Sigma, St. Louis, MO), 10 mM β-glycerophosphate (Sigma), and 173 mM ascorbic acid (Sigma). Cells were expanded on tissue culture polystyrene flasks with media changes every 3 days and grown to 80% confluency before being passaged using trypsin/EDTA. Cells at passage P4 were used for the experiments.

Fibrin Hydrogel Preparation and Characterization

Fibrinogen and thrombin from bovine plasma, and gelatin type I were purchased from Sigma. Type A porcine gelatin (300g Bloom) was purchased from Sigma. The bioink was prepared by mixing different ratios of fibrinogen and gelatin and heating to 60°C for 15 min. The hydrogel samples were printed using an extrusion-based bioprinter (3D-Bioplotter; EnvisionTEC; Germany). All printing supply (30cc barrel and 200 µm/400 µm precision tips) were purchased from Nordson EFD (RI, USA). The fibrin bioink was loaded into the low-temperature printer head and allowed to equilibrate for 30 min at a 22°C. Printed constructs were crosslinked in 100 U thrombin for 30 min. The printer took successive images of each layer during printing, allowing quantification of strand diameter in each layer.

Swelling experiment: For each bioink formulation, nine samples per group were printed and crosslinked. Each 10 mm by 10 mm sample was printed using a 200 µm tip, and fibers were spaced every 200 µm. Pictures were taken before and after 24 h incubation in PBS at 37°C. Images were analyzed using ImageJ to calculate strand diameter and pore area. The swelling was calculated by dividing the average porosity of a sample post-printing by the average porosity of the same sample after incubation.

Cell Viability Assay: Mouse fibroblast, L929, was used to assess in vitro viability, as per ISO standard 10993-5. Cell viability was assessed using a Live/Dead assay (Invitrogen) following the manufacturer's protocol. Briefly, 6 samples per group were incubated with 2 µM ethidium homodimer and 4 µM calcein AM for 1 h. Dead control

was incubated in 70% methanol (Sigma) for 15 min prior to Live/dead staining. Fluorescent images were taken using a confocal microscope (Leica SP5 X). Five digital images per samples, with each an area of 1 mm2, were processed in ImageJ. A resulting percentage of cell viability was calculated from the ratio of the number of live cells divided by the total number of cells.

Evaluation of Fibrin Hydrogels: Shear stress and viscosity measurements as a function of shear rate of the fibrin bioink were obtained at 22°C (printing temperature) using an AR2000 stress-controlled rheometer (TA Instruments, Newark, DE) with a plate-plate geometry. A Q800 Dynamic Mechanical Analyser (TA Instruments LLC, Delaware, USA) was used to evaluate the compressive modulus of fibrin hydrogels. The compressive stress-strain was obtained at a strain rate of 1mm/min at room temperature.

PCL Carrier Scaffold Fabrication and Characterization

Computational Modeling: Scaffolds were designed with 3D solid modeling CAD software (Solidworks 2015). Circular cross-sections were swept along a pattern mimicking the Bioplotter needle path during printing to make a uniformly porous structure. CAD models corresponding to various extruder needle sizes (200 and 400 μm) and inner cylinder diameters (2, 4, and 6 mm) were designed. A computational fluid dynamic analysis was performed using Solidworks Flow Simulation Module. Briefly, the scaffold models were enclosed in a hollow cylinder to allow for the establishment of the computational domain with the inlet perfusing water at a fully developed, laminar, volumetric flow rate of 100 mm3/s at 37°C through the bottom of

the scaffold and the outlet representing environmental pressure at the top end of the scaffold.

PCL Samples Preparation: Scaffolds, with a dimension of 10 mm in diameter and 5 or 10 mm in height, were fabricated using a commercial 3DP system with corresponding cartridges and needles (3D Bioplotter, EnvisionTEC, Gladbeck, Germany). PCL (MW 43000, Polysciences, Warrington, PA) was loaded into a high-temperature print head and heated at 120°C for 30 min prior to printing. Strands were extruded at a pressure of 5 bar and speed of 2 mm/s to form scaffolds.

Scanning Electron Microscopy (SEM): For morphology observation of internal structures, samples were imaged by a field emission gun scanning electron microscope (Hitachi SU-70) at 5 kV. Images were analyzed using ImageJ to calculate pore size and strand diameter and to determine printing accuracy.

Compressive Mechanical Testing: Compressive mechanical analysis was performed on four samples per group using an Instron mechanical testing system (33R/4465, Norwood, MA). All tests were performed using a high-capacity load cell (5000 N). Samples were compressed at a displacement rate of 2 mm/min, and experimental values were recorded every 10 ms. Compression was maintained until a drop of at least 60% in force was measured. Engineering stress and strain were calculated based on original cross-sectional area and height, respectively, which were then used to compute compressive modulus, 1% offset yield stress and ultimate compressive stress.

In vitro and In vivo evaluation

Scaffolds Preparation: Scaffolds for in vitro and in vivo evaluation were fabricated using a commercial 3D printing system (3D Bioplotter, EnvisionTEC, Gladbeck, Germany). For both experiments, cells were passaged, suspended in media and centrifuged to form a pellet. After aspiration of the supernatant, the pellet was then suspended in fibrin bioink by manual pipetting, until the solution was homogenous and all clumps were broken down. All fibrin samples, control and experimental, were about 1 mm in thickness and 2.5 mm in diameter. For in vitro evaluation, fibrin bioink encapsulating either 2x106 hMSCs/mL or 3x106 HUVECs/mL were loaded into separate print heads and were heated to 22°C for 30 min prior to printing. Control groups consisted of fibrin bioink casted within the barrel of a 3 mm diameter syringe and contained a suspension of hMSCs and HUVECs (ratio 3:1) at a density of 2x106 cells/mL. The ratio was calculated based on the actual volume of ECs and MSCs bio inks used by the Bioplotter to print the experimental samples (19µL and 73µL respectively, for a print, comprise of 25 osteons). Once gelled, control samples were casted out of the syringe using the plunger. All scaffolds were crosslinked into 100 U thrombin for 30 min before being transferred to appropriate culture media and incubated at 37°C. Media was changed every 2 days. For in vivo experiments, fibrin bioink encapsulating 2x106 rMSCs/ml or 3x106 RAECs/ml and PCL were loaded into separate print heads and were heated to 22°C and 120°C respectively, for 30 min prior to printing. Control groups consisted of printed PCL base and a casted fibrin bioink disc containing either a suspension of rMSCs or a suspension of rMSCs and RAECs (ratio 3:1) at a density of 2x106 cells/ml. All scaffolds were allowed to crosslink for 30min in 100 U thrombin before subdermal rat implantation.

DNA quantification Assay: Cell samples from each group (n=9) were isolated from fibrin hydrogels by dissolution in 1 mg/mL collagenase (Sigma) for 120 min at 37°C and a cell pellet was formed by centrifugation and washed with PBS three times. Total DNA was isolated using DNeasy Blood and Tissue Kit (Qiagen) according to the manufacturer instructions. DNA content was quantified using the PicoGreen DNA assay (Invitrogen) following the manufacturer's instructions.

Quantitative reverse transcriptase polymerase chain reaction (rt-PCR): Total RNA was isolated using the RNeasy Plus Mini Kit (Qiagen), following the supplier's protocol (n=9). Reverse transcription was performed using TaqMan Reverse Transcription reagents (Applied Biosystems) following the supplier's protocol. qRT-PCR was performed using TaqMan PCR Master mix and TaqMan Gene Expression Assays for alkaline phosphatase (ALP), bone morphogenetic protein-2 (BMP2), vascular endothelial growth factor-A (VEGFA) and platelet and endothelial cell adhesion molecule-1 (PECAM1). Quantification of target gene expression was calculated relative to the reference glyceraldehyde 3-phosphate dehydrogenase (GAPDH) gene. The mean minimal cycle threshold values (Ct) were calculated from triplet reactions.

Animal Implantation: The Institutional Animal Care and Use Committee of the University of Maryland approved the study (protocol number R-MAY-18-26), and all animals were treated in accordance with the Guide for the Care and Use of Laboratory Animals. The experiment was conducted in 6 male adult Sprague Dawley rats. A small incision was made on the back of each animal, and one scaffold from each group was implanted in the subdermal space. At 7 and 14 days post implantation, 3 animals were

euthanized and the samples and surrounding tissue were explanted. Each explanted tissue sample was preserved in paraformaldehyde (4%) for histological analysis.

Histological Analysis: Explanted tissue samples were processed, embedded in paraffin and sliced (15 µm slides) by Histoserv, Inc. (Germantown, MD). For histological evaluation, sections were stained by Masson's Trichrome staining and Von Kossa staining, to demonstrate deposits of calcium or calcium salts. Von Kossa calcium positive control slides (placenta) were purchased from Newcomer Supply (Middleton, WI). Images were analyzed using ImageJ to quantify collagen surface area, cell surface area, and the number of blood vessels per area. Area refers here to the area of the picture, to which the empty area (void left by the PCL scaffold) were subtracted. To quantify the collagen surface area (stained blue) and cell surface area (stained purple), first hues were adjusted using the function Adjust/Color Threshold to isolate either blues or purples. The pictures were then made binary (Process/Binary), and the black surface area was measured. Cell or collagen surface area was obtained by subtracting the area occupied by the scaffolds fibers to the black surface area. Blood vessels were identified as a tubular structure with a dark purple rim, filled with erythrocytes (stain light purple/red).

Statistical Analysis

Data were analyzed using single factor analysis of variance (ANOVA) followed by Tukey's Multiple Comparison Test assuming normal data distribution with a confidence of 95% ($p<0.05$).

Results and Discussion

3D Printed Fibrin Bioink

3D printing offers an efficient tool for accurate fabrication of biomaterial scaffolds with tunable properties and defined architecture. The first objective of this work was to optimize the fibrin bioink to improve the resolution of printed fibers and to understand the influence of printing parameters on extruded fiber diameter and cell survival in order to ensure a reproducible printing process.

Because of their mechanical degradation properties (i.e. fibrin breaks down with fibrin hydrogels are not good candidates for pressure based extrusion printing. A composite hydrogel consisting of fibrinogen and gelatin was then prepared, using gelatin as a support material during the printing process, which then will be leached into the media. We tested two concentrations (5w/v% and 10w/v %) of each to achieve proper printing resolution. Each group of bioink was extruded to form a rectangular lattice, with defined fiber diameter and pore size. Pictures of each printed samples were taken immediately after printing and 24h after crosslinking in thrombin and incubation at 37°C to allow the gelatin to leach out (

*Figure **6***a). All of the images were then analyzed to measure changes in pore size. The bioink containing 10w/v% fibrinogen and 5w/v% gelatin had the lowest degree of either swelling or shrinking (

*Figure **6***b) which is ideal, and therefore was used for the remainder of the experiments. The results shown in

*Figure **6***b can be explained by two phenomena. First, a high concentration of fibrinogen has been shown to result in fibrin gels with an increased number of fibrin fibers and decreased porosity, which therefore does not absorb as much water as gels with lower fibrinogen concentrations [179]. Second, gelatin was used here as a thickener agent and therefore was not modified and crosslinked. The gelatin contained in the sample was leaching out into the incubation media, resulting in a loss of material in the sample.

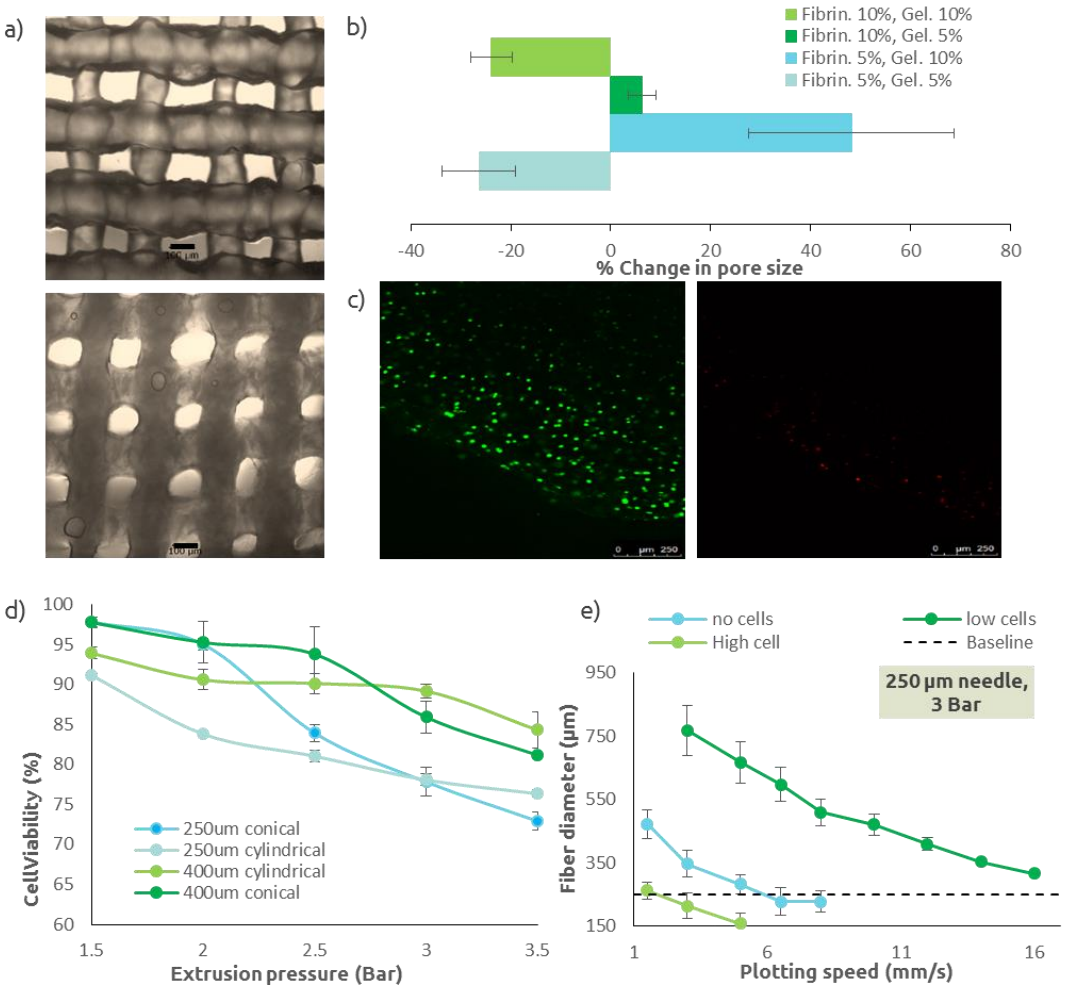

Figure 6 Fibrin bioink characterization. (a) Micrographs of 3D printed fibrin bioink (fibrinogen 5%, gelatin 5%) immediately after printing (top) and after 24h, following crosslinking of the fibrinogen and leaching of the gelatin (bottom). Fiber swelling is visible in this example. Scale bar is 100 µm. (b) Change in pore size for each bioink groups (n=9). A negative change correlates to a swelling of the extruded fibers, while a positive change corresponds to a shrinking of the extruded fibers. Fibrinogen 10%w/v/ gelatin 5%w/v was the chosen bioink composition for following experiments. (c) Live/Dead images of extruded L929. Live cells (left) are stained green, dead cells (right) are stained red. Cells were counted using Image J in order to quantify cell viability. (d) Cell viability after extrusion in the 3D printer, as a function of extrusion pressure and needle size/shape (n=6). (e) Extruded fiber diameter as a function of extrusion pressure, plotting speed, and cell density for a needle with an inner diameter of 250µm, which was used in the following experiments (n=9). The baseline line represents the targeted fiber diameter (i.e. needle inner diameter). All data points represent mean ± standard deviation.

Prior to printing full-size constructs, parameters influencing cell viability were investigated in order to select the most appropriate conditions to construct a highly viable cell-laden scaffold. Fibers of bioink seeded with L929 cells were extruded at variable pressure (1.5 to 3.5 bar), needle type (conical or cylindrical), and needle diameter (250µm and 400µm) to study the effect of pressure and needle on cell viability directly after printing. Extruded fibers were stained with Live/Dead and imaged (

*Figure **6***c). Images were processed and dead or live cells counted to quantify cell viability. Across all groups and for any pressure, cell viability was greater than 70% (

*Figure **6***d). For all tested needles, higher extrusion pressure resulted in decreased cell viability. Cell viability was dependent on needle type, with higher cell viability for conical needles at low pressure (<2 bar). However, for higher pressures (>2.5 bar), cell viability observed for cylindrical needles was significantly ($p<0.05$) higher than with conical needles. To understand the discrepancy between two needle types, finite element simulations were performed. The simulation demonstrated that for low pressure, higher shear stresses were shown for conical needles, but were only observed proximal to the fluid outlet, limiting exposure to high shear stress to this region. On the other hand, shear stresses in cylindrical needles were lower but for an increased passage length. However, at higher pressure (>2.5 bar), as flow velocity increased, the passage time of cells in this high shear region is reduced and the limited exposure to shear stress in conical needles cannot make up for the higher shear stresses induced.

The accuracy of a 3D printed sample depends on the accuracy of the extruded fibers. Fibers should be round and their diameter should theoretically match the inner diameter of the extrusion needle. The effects of extrusion pressure, plotting speed, cell density using different needle size, on extruded fibers diameter, and therefore printing accuracy, are shown in

*Figure **6***e. Increased pressure and decreased speed resulted in larger fibers diameter, which was expected. The incorporation of cells altered the rheological properties (

Figure **10**), which was correlated with fiber diameters. While using a 400µm needle, results showed decreased fiber diameter with increased cell density, with smaller fibers (i.e. more viscous bioink) observed with the highest cell density. However, while using a 250µm needle, results showed no correlation between fibers diameter and cell density. This indicated that the viscosity of the low cell density bioink changed in function of the applied shear stress between needle sizes.

PCL Carrier Scaffold Characterization

The second objective was to improve the mechanical strength of the construct by co-printing the fibrin bioink along a supporting PCL carrier scaffold. Tissue engineering scaffolds must retain sufficient mechanical properties to fulfill the requirements of structural integrity once implanted in vivo. Accordingly, we considered whether our osteon-like constructs had mechanical properties similar to that of bone. Dynamic mechanical analysis performed on fibrin hydrogels showed an elastic modulus of

0.7±0.3MPa under compression. However, cortical bone compressive strength is in the range of 100-150MPa [184]. In order to improve the mechanical strength of the construct, we designed and 3D printed PCL carrier scaffolds that would be co-printed along the fibrin bioink and would encase several fibrin hydrogels (*Figure 7*a). Several PCL carrier scaffolds were 3D printed, with defined pore size, fiber diameter, center post and variable porosity (*Figure 7*b). Sufficiently high porosity and suitable pore size are required for spreading of cells and nutrients throughout the structure. An optimal pore size for bone tissue engineering scaffolds is not well defined, however pore sizes between 100 and 400μm are considered optimal for osteoconduction, and pore sizes greater than 300μm have been shown to enhance bone formation via vascularization [185,186]. In order to evaluate printing accuracy, SEM images (**Figure 7**b) of the 3D printed constructs were analyzed in order to quantify the resulting pore size and fiber diameter. Across, all printed constructs, results showed that printed fibers were on average 9.6±0.4% bigger than the designed ones, resulting in pores on average 18.2±1.7% smaller, due to spreading and thermal expansion of the PCL matrix during 3D printing. These results were taken into account when designing PCL 3D printed scaffolds for later experiments.

Computational modeling of flow was performed and showed a homogeneous and sufficient fluid distribution throughout the scaffold, with minimum shear stress (*Figure 7*c). Finally, compressive mechanical testing was performed on 3D printed PCL scaffolds. *Figure 7*d shows a typical stress/strain curve from compression testing, with an initial increase in stress at low strain followed by a plateau region, with fluctuations. These fluctuations could be attributed to the successive collapse of each

layer under compression. The compressive moduli of the porous scaffolds were quantified from the initial slope of the stress-strain curve in *Figure 7*d. All the PCL scaffolds showed improved mechanical properties with an average compressive modulus of 130.93±22.74MPa, which falls in the lower range of cortical bone [184].

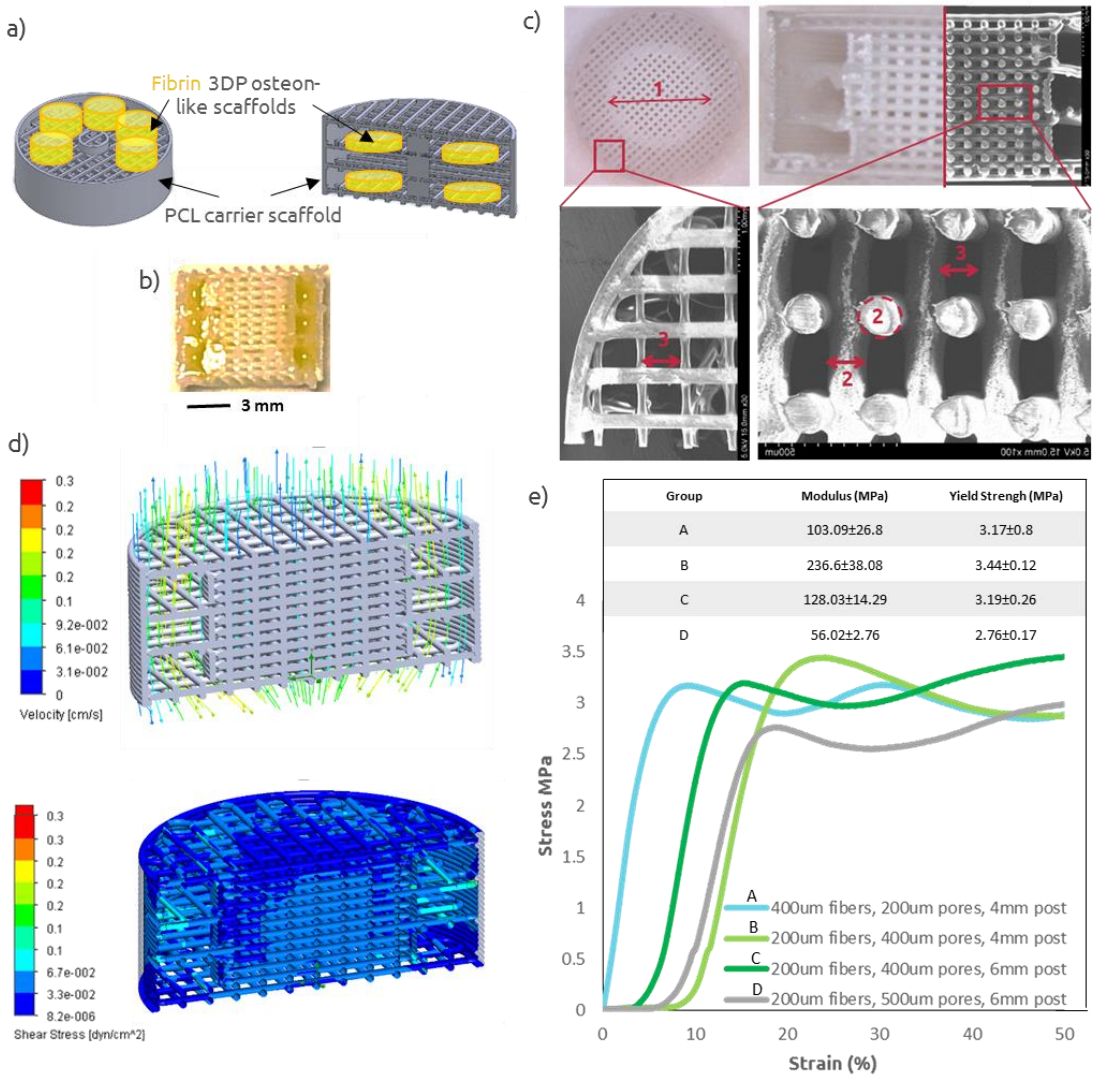

Figure 7 PCL Carrier Scaffold Characterization. (a) Schematic of 3D printed osteon-like scaffolds (green) and PCL carrier scaffold (gray). (b) Micrograph of a 3D printed PCL/Fibrin scaffold. Yellow food coloring was added to the fibrin bioink for photography purpose. (c) Micrograph and SEM images of 3D printed PCL scaffolds, with variable central post diameter (1), fiber diameter (2), and pore size (3). (d) Computational modeling of flow and shear stress within 3DP scaffolds while under perfusion. (e) the strain-stress curve for four representative examples of 3DP PCL scaffolds (n=4). All data points represent mean ± standard deviation.

In Vitro and In Vivo Evaluation of Osteon-like Scaffolds

The third objective of this work was to test the osteogenic and angiogenic potential of osteon-like scaffolds, and demonstrated that a bio-inspired approach could enhance neovascularization of the graft. Constructs were 3D printed using the Bioplotter. As shown in Figure 8a and Figure 8b, the osteon-like unit had a concentric triple-ring structure with an outer diameter of 2.5 mm. A set of two bioink was used: one encapsulating hMSCs for the outer rings and one encapsulating HUVECs to recreate the Haversian canal in the center. After 14 days of in vitro culture, cells were retrieved and DNA and RNA were collected. The DNA quantification assay showed a significantly higher ($p<0.05$) DNA concentration in the printed samples compared to the casted samples (Figure 8c). In addition, a significant increase ($p<0.05$) in DNA concentration over the 14 days was found for the printed samples, while the casted samples showed no significant changes ($p=0.084$). Scaffolds were stained using Live/Dead to assay cell viability after 7 and 14 days of culture (Figure 8e). Cell viability was not significantly different ($p=0.071$) between control and experimental groups. After 14 days, cell viability was 94.8±2.8% for the printed samples. Rt-PCR showed an increase in gene expression of BMP2, ALP, VEGFA, and PECAM1 in both groups after 14 days (Figure 8d). However, while rt-PCR showed no significant difference in gene expression of osteogenic markers ($p=0.098$), a significant fold change ($p<0.05$) in mRNA of angiogenic markers was observed.

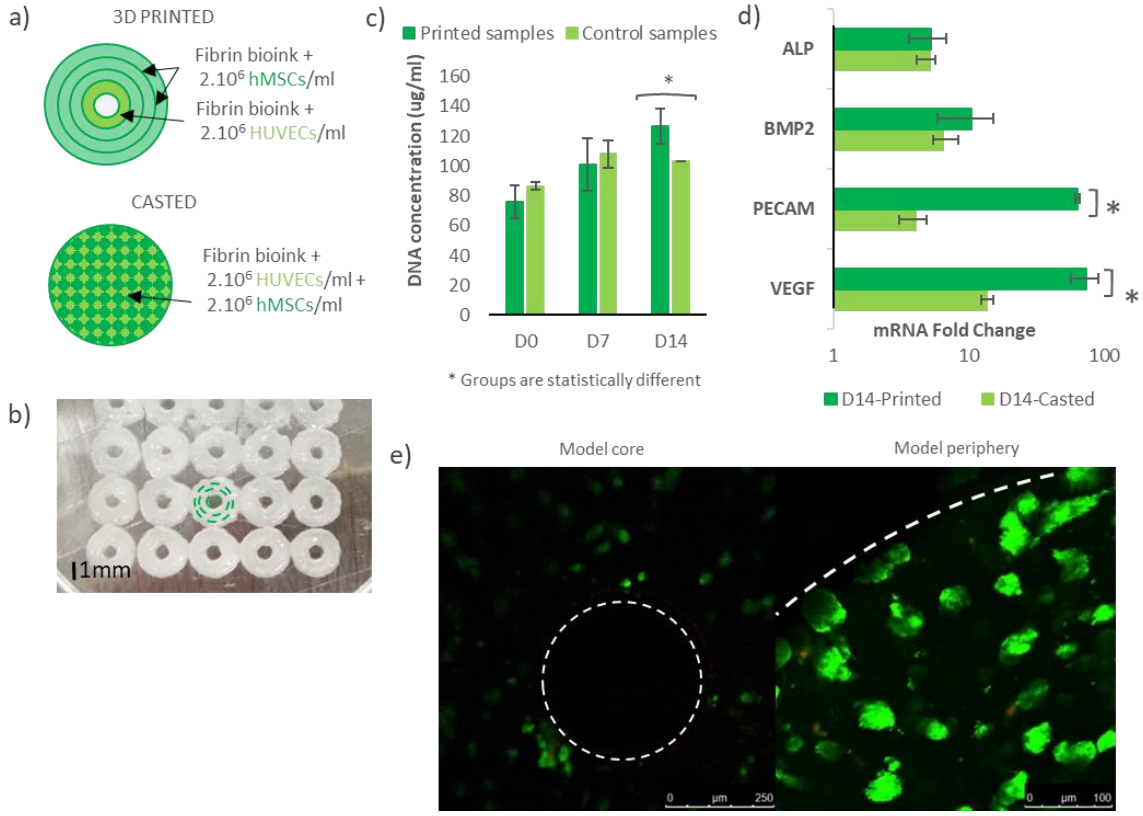

Figure 8: Osteon-like scaffolds in-vitro experiment. (a) Schematic of 3D printed osteon-like scaffolds and casted controls. 3DP scaffolds are composed of four concentric fibrin fibers of 250µm in diameter, containing hMSCs for the three outermost rings, and HUVECs for the innermost ring. Casted samples containing a mixture of MSCs and HUVECs (2.10^6 cells/ml) were used as controls. (b) Bioplotter picture of 3D printed constructs. The inner channel is 350µm in diameter and the complete scaffold is 2.5 mm in diameter. (c) DNA quantification assay showed significant increase in DNA concentration ($p<0.05$) over 14 days of *in vitro* culture in the printed samples compared to the casted samples (n=9). In addition, a significant higher DNA concentration ($p<0.05$) was shown in the printed samples, while the casted samples showed no significant changes. (d) mRNA expression fold change between day 0 and day 14 of *in vitro* culture (n=9). Rt-PCR showed no significant difference in gene expression of osteogenic markers ($p=0.098$), but a significant fold change in mRNA of angiogenic markers ($p<0.05$). (e) Live/Dead images of 3D printed scaffolds at day 14 (n=3). Live cells are stained green, and dead cells are stained red. Cells were counted using Image J in order to quantify cell viability. All data points represent mean ± standard deviation.

In vivo experiments were performed in order to demonstrate the ability of the construct to successfully integrate with the host tissue and assess the angiogenic potential of the scaffolds. Osteon-like samples, as well as MSCs/ECs, casted controls, were implanted subcutaneously in rats (*Figure 9*a), with enough distance between them to be retrieved easily: the MSCs only control was implanted cranially, the MSCs/ECs control caudally and the 3D printed samples in the middle. After 14 days, the samples were retrieved. From simple visual inspection, experimental samples appeared to have a darker red color indicative of potential vascularization (*Figure 9*b). Further histological analyses were performed using Masson's trichrome and Von Kossa (for mineralization) stains. No signs of inflammation (large fibrous capsule, giant cells) were observed in all groups. Masson's trichrome stain showed a clear qualitative difference between samples (*Figure 9*c). In the control sample, the fibrin hydrogel was still visible and the delimitation from surrounding tissue is clear. Cell invasion within the hydrogel had not reached the PCL carrier scaffolds, and few blood vessels were visible. The fibrin hydrogel from the 3D printed sample exhibited stronger blue staining, suggesting that more collagen had been deposited. The same observation was made with the Von Kossa stained samples (Figure 11): all groups showed increased mineralization between day 7 and day 14, but the 3D printed samples exhibited the most increase.

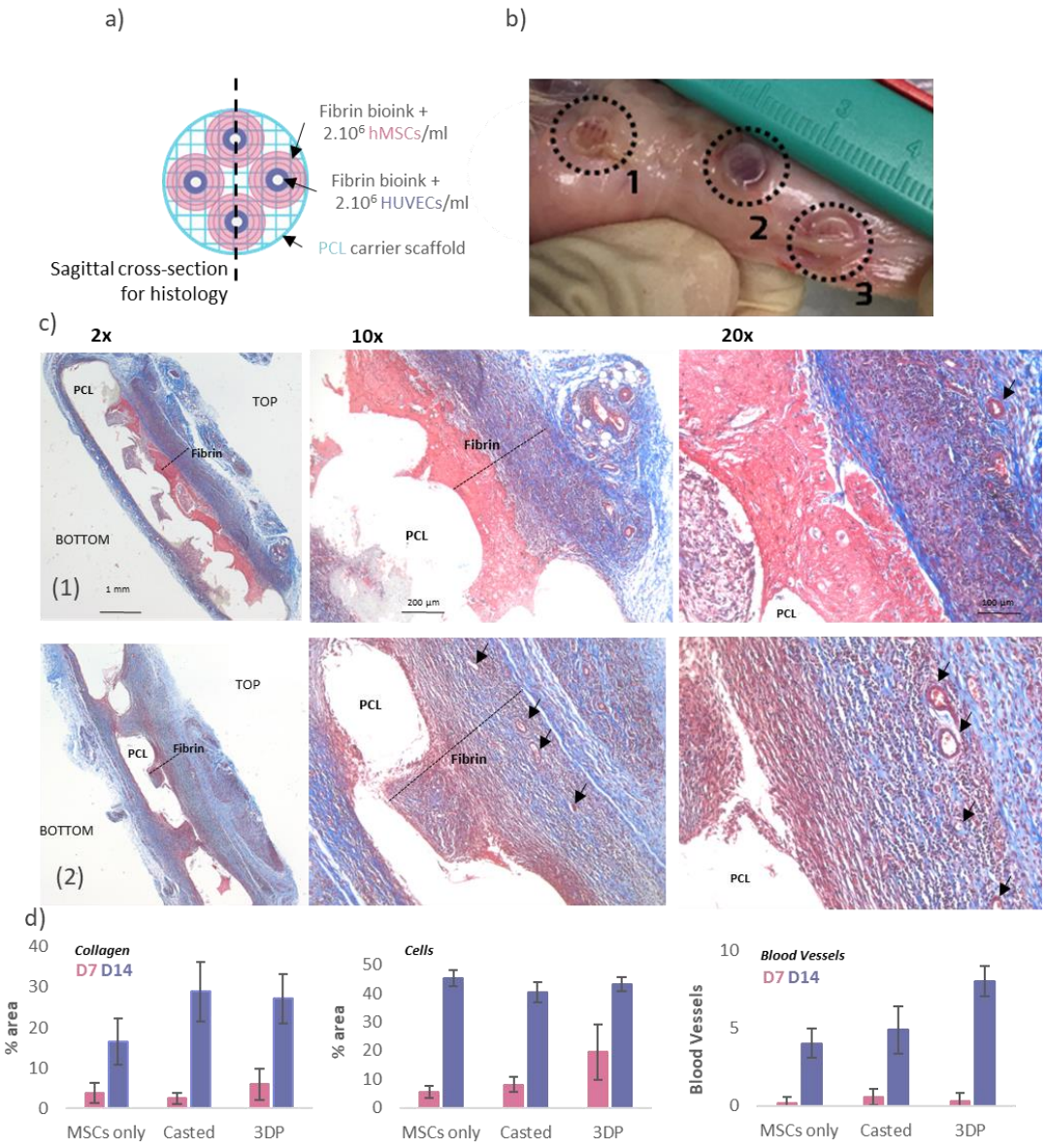

Figure 9 Osteon-like scaffolds in-vivo experiments. (a) Schematic of a 3DP scaffolds. Osteon-like fibrin hydrogels are co-printed with PCL for support. Each 3DP sample comprises four osteon-like fibrin hydrogels, with a diameter of 6.4mm. Control samples consisted of fibrin bioink casted within the barrel of a 3 mm diameter syringe. Once gelled, control samples were casted out of the syringe using the plunger and assembled onto a 3D printed PCL scaffold. (b) Images of samples after 14 days implantation in vivo. TOP refers to the side of the implant with osteons, while BOTTOM refers to the side with the PCL support. (1) rMSCs only control scaffold, (2) rMSCs/RAECs control casted scaffold, and (3) rMSCs/RAECs 3DP osteon-like scaffold. (c) Micrographs of embedded, sectioned and stained samples using Masson Trichrome. Line (1) images of rMSCs/RAECs controls at day 14 after implantation. Line (2) images of 3DP rMSCs/RAECs at day 14 after implantation. Collagen is stained blue, cell nuclei are stained dark purple and fibrin is stained pink. Black arrows indicate blood vessels. (d) Quantitative analysis of Masson's Trichrome images showing the percent area of the pictures covered by either collagen or cells, and the average number of blood vessels per picture (n=12). All data points represent mean ± standard deviation. Groups not sharing a letter are statistically different ($p<0.05$).

Quantitative assessment was performed using Image J. The percentage area of each picture covered by collagen or cells was measured and averaged. The number of blood vessels per area was also counted and averaged. No statistical difference in collagen deposition was observed between the three groups after 7 days. However, after 14 days of in vivo culture, both groups containing ECs had a statistically higher collagen deposition than the MSCs only control. After 14 days of in vivo culture, no significant difference ($p=0.087$) in cell density between groups was observed. However, cell infiltration was more pronounced in the 3DP osteon-like groups, as shown by a statistically higher surface area ($p<0.05$) covered by cells after 7 days of culture. Finally, after 14 days of culture, blood vessels were observed throughout the scaffolds, and a significant increase ($p<0.05$) in the number of blood vessels per area in 3DP osteon-like samples was observed.

In both the mixed and osteon-like scaffolds, the co-culture of ECs and MSCs improved the deposition of collagen, one marker of osteogenesis, and neovascularization. Numerous studies on ECs/MSCs coculture have been demonstrated to achieve enhanced cellular signaling. Both cell populations are known to secrete specific growth factors that are beneficial for mutual growth and differentiation for each other. MSCs promotes neovascularization by secreting pro-angiogenic growth factor such as Ang-1, FGF-2 and, VEGF likely through paracrine communication between EPCs and MSCs, which simulates EPCs proliferation and differentiation[187–189]. In return, EPCs secrete osteogenic growth factors such as insulin growth factor 1, and BMP-2, promoting MSCs differentiation [34,190,191]. In addition, osteon-like scaffolds showed significantly higher cell infiltration and

neovascularization within the construct than the two other control groups. MSCs paracrine factors production and release has been shown to vary with the substrate microarchitecture, stiffness or composition [35,192,193]; although it remains to be proved, we contend that the specific respective patterning of cells, in this case in the shape of osteons, could also affect paracrine signaling or other cell-cell communications, and result in an improved neovascularization. Thus, further experiments are warranted to explain the observed phenomena, and relevant research is progressing in our laboratory. In addition, this osteon-like scaffold could be further optimized to improve its bio-inspired characteristic, for example scaling by incorporating a non-organic phase (hydroxyapatite) to the bioink.

Conclusions

In the present study, we demonstrated the successful fabrication of a novel 3DP fibrin-PCL composite scaffold, with mechanical strength comparable to bone, a stable swelling behavior and cell bioactivity for the construction of bio-inspired structures. Using 3D printing technologies, bioinks were patterned into varied geometries and with controlled dimensions, in order to recreate an optimal microenvironment mimicking the native natural cell pattern found in bones, to form a simplified model of osteons. Most importantly, the utilization of these scaffolds in constructing bio-inspired osteons for bone regeneration demonstrated a promising capacity to improve neovascularization of the construct. These results indicate that proper cell orientation or patterning could play a critical role in neovascularization. The role of distance

between cell populations, introduced via 3D printing, is explored in the next chapter. This bio-inspired osteon-like construct holds potential to be developed as scaffolds in vascularized bone tissue engineering. In addition, advancements in the field of 3D printing, and a higher level of precision will allow the printing of ever more bio-inspired structures.

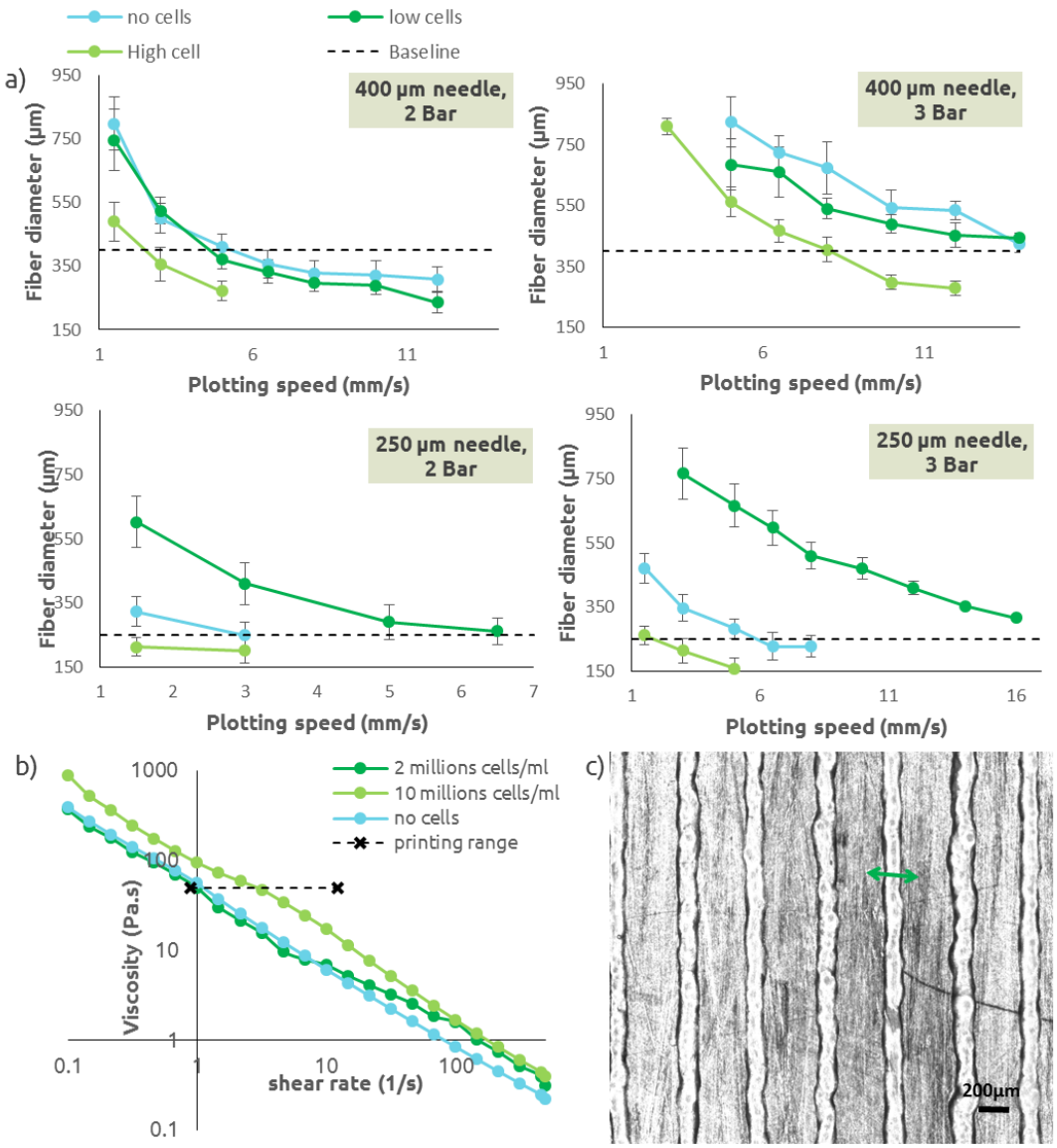

Figure 10: Supplemental Data: Fibrin bioink printing accuracy. (a) Extruded fiber diameter as a function of extrusion pressure, plotting speed, and cell density for variable needle inner diameter (n=9). The baseline line represents the targeted fiber diameter (i.e. needle inner diameter). (b) Rheological evaluation of fibrin bioink seeded with variable density of L929s. The printing shear rate was calculated for every printing condition, the printing shear rate range is represented in black. (c) Bioplotter image of extruded fibers used to measure extruded fiber diameter.

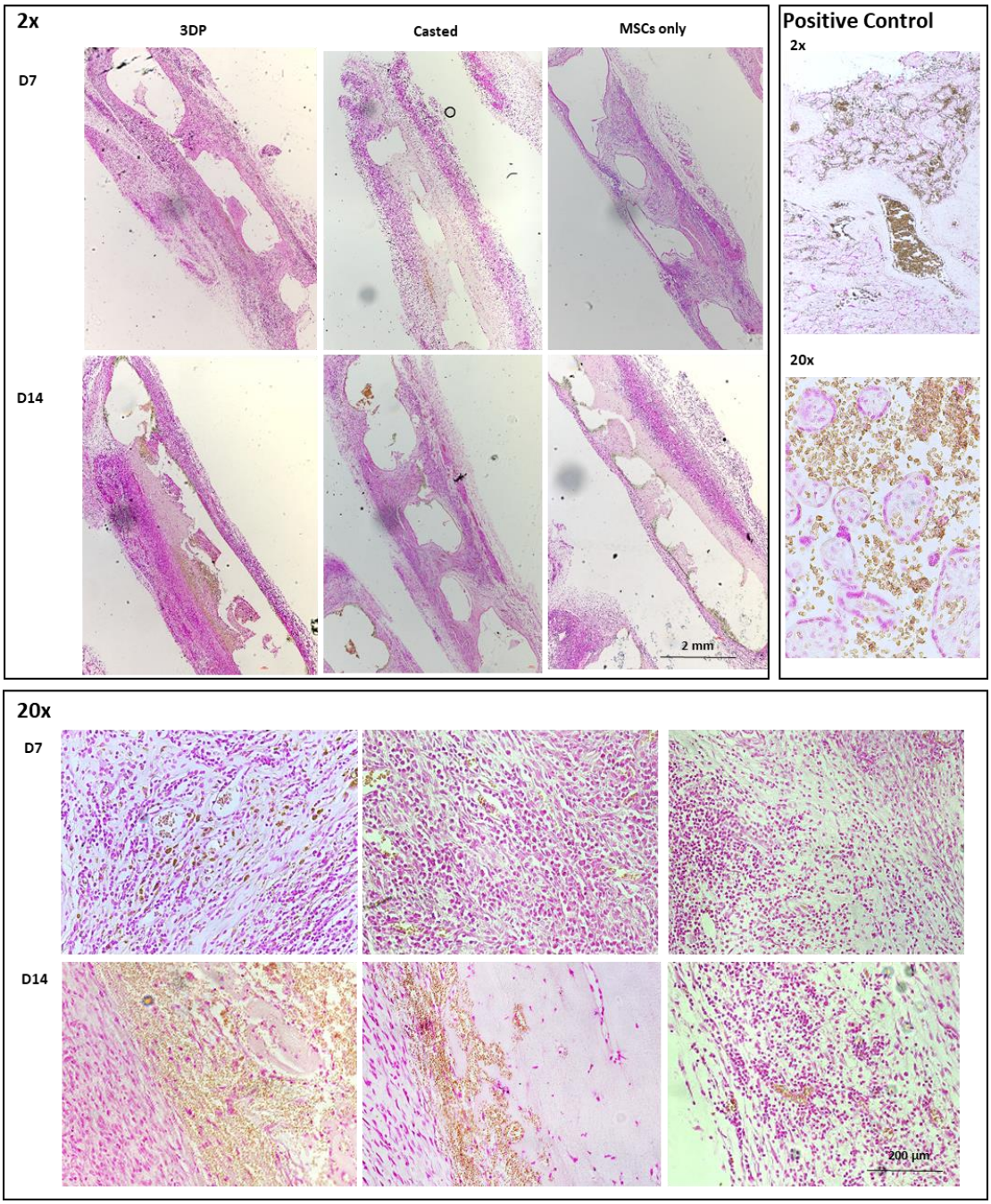

Figure 11: Supplemental Data: Von Kossa staining. Micrographs of embedded, sectioned and stained samples (rMSCs only, rMSCs/RAECs control or rMSCs/RAECs 3DP) using Von Kossa, 7 or 14 days implantation in vivo. Calcium deposits are stained brown to dark depending on UV exposure. 0.1% Nuclear Fast Red Solution was used as a counterstain, staining nuclei pink. Von Kossa staining showed increased mineralization between day 7 and day 14 in all groups, with the most increase shown in the rMSCs/RAECs control and rMSCs/RAECs printed groups.

Chapter 5: Cell-to-Cell distance of HUVECS and MSCs in 3D printed cocultures impacts cellular interactions and angiogenesis.

Introduction

It is well established that human umbilical vein endothelial cells (HUVECs) and human mesenchymal stem cells (hMSCs) secrete specific growth factors that are mutually beneficial. For example, endothelial cells are known to secrete growth factors such as insulin growth factor-1 [33], endothelin-1, and bone morphogenic protein-2, promoting osteogenic growth and differentiation of the MSCs [34].

Recently, studies suggested that cell-cell communication and paracrine secretion can be affected by the substrate microarchitecture [35], mechanical environment [36] or the matrix stiffness [37]. However, little is known about the effect of cell patterning and the distance between cell populations on their crosstalk. The precisely regulated architecture of different tissue types, such as osteons in bones, indicates that characteristic features related to the number, types, and spacing of cells might be critical to tissue function. We previously demonstrated that an osteon-like scaffold, with specific patterning of HUVECs and MSCs, improved neovascularization of the implant in vivo [194].

Until recently, recapitulating complex hierarchical structures in vitro has proved difficult due to limited manufacturing techniques, particularly while using biological materials. 3D printing (3DP) using a three-axis dispensing system, which

builds 3D constructs by extruding fibers of cell-laden materials in a layer-by-layer fashion, offers a unique opportunity in tissue engineering, by enabling precise positioning of cells and biomaterials, tunable mechanical properties, fine control of the external and internal architecture [182]. Controlling those specific parameters can modulate cellular effects. For example, pore sizes of at least 300 µm have been shown to enhance bone formation and vascularization [185]. Could 3D printing also be used to improve angiogenesis by modulating the crosstalk between EC and MSCs, through the precise control of the distance between fibers?

In the present study, the overall objective was to investigate how the distance between 3D printed fibers (i.e. separation and distance between ECs and MSCs populations) affects angiogenesis by modulating cell-cell communication in different 3D printed co-cultures (**Figure 12: Methods. (a) Chart showing the different experimental groups: Endothelial Cells (ECs), Mesenchymal Stem Cells (MSCs), Mixed, and Separated** with a distance of 0µm (D0), 200µm (D1), 400µm (D2) between fibers. ECs/MSCs groups are made of adjacent fibers containing only ECs/MSCs, respectively. The bioink for the mixed group contains both ECs/MSCs, and the fibers are also printed adjacent to each other. For the D0, D1, D2 groups, ECs and MSCs are encapsulated in different bioinks, and the fibers are printed alternatively and with a distance of 0, 200, 400µm between them. (b) Micrographs of 3D printed samples (D0, D1, D2). All samples are 8mm diameter and 1mm thick discs. All samples were stained directly after printing, using calcein, showing live cells in green. Using ImageJ, the distance between fibers was calculated: d(D1)= 195.14±25.4µm and

d(D2)=381.7±25.97µm. (c) After printing, 3D printed samples were incubated for 48h in serum free media. After 48h, the media was collected and the ECs from the samples were magnetically sorted.). ECs and MSCs can communicate through three mechanisms: (i) the direct interaction between membrane molecules of the two adjacent cells (tight junctions, adherent junctions), the secretion of (ii) diffusible factors that diffuse freely in the extracellular environment and interact with the target cells through specific receptors, and (iii) the release of extracellular vesicles (EVs). To this end, we separately analyzed ECs grown in different co-culture conditions and, the paracrine secretions and the released EVs in the conditioned media. Finally, we used functional assays to study the cells and conditioned media angiogenic potential. In vitro angiogenesis assays provide a valuable tool for assessing the effect of angiogenic products as they enable the analysis of isolated processes that contribute to angiogenesis, such as ECs migration, proliferation, sprouting, branching, and lumen formation [56].

Materials and Methods

Cell culture

hMSCs (RoosterBio, Frederick, MD) were cultured in RoosterBasal Media supplemented with RoosterBooster, as per the manufacturer's specifications. Cells were expanded on tissue culture polystyrene flasks for 5 days and grown to 90% confluency before being passaged using trypsin/EDTA. Cells at passage P3 were used for the experiments.

HUVECs (Lonza) were cultured in EBM-2 Basal Medium (Lonza) supplemented by EGM-2 SingleQuot Kit. Cells were expanded on tissue culture polystyrene flasks with media changes every 3 days and grown to 80% confluency before being passaged using trypsin/EDTA. Cells at passage P4 were used for the experiments.

3D Printed Cocultures Preparation

All samples, for the six experimental groups (**Figure 12: Methods. (a) Chart showing the different experimental groups: Endothelial Cells (ECs), Mesenchymal Stem Cells (MSCs), Mixed, and Separated** with a distance of 0µm (D0), 200µm (D1), 400µm (D2) between fibers. ECs/MSCs groups are made of adjacent fibers containing only ECs/MSCs, respectively. The bioink for the mixed group contains both ECs/MSCs, and the fibers are also printed adjacent to each other. For the D0, D1, D2 groups, ECs and MSCs are encapsulated in different bioinks, and the fibers are printed alternatively and with a distance of 0, 200, 400µm between them. (b) Micrographs of 3D printed samples (D0, D1, D2). All samples are 8mm diameter and 1mm thick discs. All samples were stained directly after printing, using calcein, showing live cells in green. Using ImageJ, the distance between fibers was calculated: d(D1)= 195.14±25.4µm and d(D2)=381.7±25.97µm. (c) After printing, 3D printed samples were incubated for 48h in serum free media. After 48h, the media was collected and the ECs from the samples were magnetically sorted. a), were 3D printed using a commercial 3D printing system (3D Bioplotter, EnvisionTEC, Gladbeck, Germany). All printing supplies (30cc barrel and 200 µm precision tips) were purchased from Nordson EFD (RI, USA). All 3D printed samples were about 1 mm in thickness and 8 mm in diameter and were

comprised of concentric fibers (200µm) separated from each other by a distance of either 0, 200 µm or 400 µm (**Figure 12: Methods. (a) Chart showing the different experimental groups: Endothelial Cells (ECs), Mesenchymal Stem Cells (MSCs), Mixed, and Separated** with a distance of 0µm (D0), 200µm (D1), 400µm (D2) between fibers. ECs/MSCs groups are made of adjacent fibers containing only ECs/MSCs, respectively. The bioink for the mixed group contains both ECs/MSCs, and the fibers are also printed adjacent to each other. For the D0, D1, D2 groups, ECs and MSCs are encapsulated in different bioinks, and the fibers are printed alternatively and with a distance of 0, 200, 400µm between them. (b) Micrographs of 3D printed samples (D0, D1, D2). All samples are 8mm diameter and 1mm thick discs. All samples were stained directly after printing, using calcein, showing live cells in green. Using ImageJ, the distance between fibers was calculated: d(D1)= 195.14±25.4µm and d(D2)=381.7±25.97µm. (c) After printing, 3D printed samples were incubated for 48h in serum free media. After 48h, the media was collected and the ECs from the samples were magnetically sorted. b).

Type A porcine gelatin (300g Bloom), fibrinogen and thrombin from bovine plasma were purchased from Sigma. The bioink was prepared by mixing 10w/v% fibrinogen and 5w/v% gelatin and heating to 60°C for 15 min. Cells were then passaged, suspended in media and centrifuged to form a pellet. After aspiration of the supernatant, the pellet was then suspended in the fibrin bioink by manual pipetting, until the solution was homogenous and all clumps were broken down. Three fibrin bioink formulations were prepared using: (1) HUVECS at a density of 2x106 cells/mL, (2) MSCs at a

density of 2x106 cells/mL and (3) a mixed of HUVECs and MSCs (ratio 1:1) at a density of 2x106 cells/mL. The fibrin bio inks were then loaded into low-temperature printer heads and allowed to equilibrate for 30 min at a 22°C. Printed constructs were crosslinked in 100 U thrombin for 30 min, rinsed in Phosphate Buffer Saline (PBS), and incubated in serum-free basal media for 48h.

MACS-mediated selection of HUVECS

Cell samples from each group were isolated from fibrin hydrogels after 48h coculture by dissolution in 1 mg/mL collagenase (Sigma) for 30 min at 37°C and a cell pellet was formed by centrifugation and washed with PBS three times. HUVECs were positively selected for CD31 by magnetic cell sorting (MACS) using MS separation columns (Miltenyi Biotech, Bergisch Gladbach, Germany). Following the manufacturer's instructions, a positive selection for ECs using the CD31 MicroBead Kit (Miltenyi) was performed. PBS was used for the final washing step and elution from the column. The $CD31^+$ population (HUVECs) was used in subsequent assays of endothelial function.

Flow Cytometry (FACS)

Cells sorting was confirmed by flow cytometry prior to use. Harvested and sorted cells suspensions were adjusted to a concentration of 1x106 cells/mL in cold PBS, 10% FCS, and 1% sodium azide. 10 μg/mL of FITC conjugated anti-CD31 antibody (Abcam, Cambridge, UK) was added to the suspension and incubated for 30 min in the dark, at room temperature. Cells were then washed 3 times by centrifugation at 400 x g for 5 min before being resuspended. Flow cytometry was performed on a BD FACSCelesta.

Quantitative reverse transcriptase polymerase chain reaction (rt-PCR).

Total RNA from HUVECs obtained after MACS-mediated separation was isolated using the RNeasy Plus Mini Kit (Qiagen), following the supplier's protocol (n=9). Reverse transcription was performed using TaqMan Reverse Transcription reagents (Applied Biosystems) following the supplier's protocol. qRT-PCR was performed using TaqMan PCR Master mix and TaqMan Gene Expression Assays for vascular endothelial growth factor-A (VEGF), platelet and endothelial cell adhesion molecule-1 (PECAM), von Willebrand factor (VWF), vascular endothelium cadherin 5 (CDH5), and integrin subunit alpha 5 (ITGA5). Quantification of target gene expression was calculated relative to the reference glyceraldehyde 3-phosphate dehydrogenase (GAPDH) gene. The mean minimal cycle threshold values (Ct) were calculated from triplet reactions.

Enzyme-Linked Immunosorbent Assay (ELISA)

For all experimental groups reported in Figure 1a, conditioned media (CdM) was collected after 72h of incubation. CdM media was concentrated using 100 kDa MWCO cut-off filters (Spin-X UF Concentrator, Corning, NY). ELISA kits (Abcam, Cambridge, UK) were used, as per manufacturer instructions, to quantify VEGF, fibroblast growth factor (FGF), angiopoietin 1 (Ang-1) and insulin-like growth factor 1 (IGF1) concentration in the concentrated CdM.

EVs Collection and quantification

EV-containing conditioned media (CdM) was collected after the samples were incubated for 72h. EVs were then isolated from the CdM via differential centrifugation

as reported previously [195]. After initial centrifugation steps to remove cellular debris and larger vesicles, EVs were pelleted in a final 118,000 x g ultracentrifugation step. EVs were then resuspended in PBS and washed with Nanosep 300kDa MWCO spin filters (Pall, NY). EV yield was measured by determining the total protein concentration and particle concentration, via bicinchoninic acid assay (BSA) using the manufacturer's protocol and nanoparticle tracking analysis, respectively. Nanoparticle tracking analysis was performed using a Nanosight LM10, software version 2.3.

Functional Angiogenic Assays

The following assays were performed with at least one of the following conditions: (1) using sorted $CD31^+$ HUVECs and EBM-2 Basal Medium (Lonza) supplemented by EGM-2 SingleQuot Kit, (2) P4 HUVECs (Lonza) and serum-free basal media supplemented with 10% CdM, or (3) P4 HUVECs (Lonza) and serum-free basal media supplemented with 50 µg/ml EVs. P4 HUVECs with full EBM-2 media were used as a positive control, and P4 HUVECs with unsupplemented basal media were used as a negative control.

Proliferation Assay. HUVECs were seeded in 24 well plates at a density of 15,000 cells per well and incubated for 36h. Images of the wells were taken using an inverted microscope (Nikon Eclipse Ti2) and analyzed using ImageJ to measure the confluency (i.e cell surface area) (Supplemental **Figure 12: Methods. (a) Chart showing the different experimental groups: Endothelial Cells (ECs), Mesenchymal Stem Cells (MSCs), Mixed, and Separated** with a distance of 0µm (D0), 200µm (D1), 400µm (D2) between fibers. ECs/MSCs groups are made of adjacent fibers containing only

ECs/MSCs, respectively. The bioink for the mixed group contains both ECs/MSCs, and the fibers are also printed adjacent to each other. For the D0, D1, D2 groups, ECs and MSCs are encapsulated in different bioinks, and the fibers are printed alternatively and with a distance of 0, 200, 400µm between them. (b) Micrographs of 3D printed samples (D0, D1, D2). All samples are 8mm diameter and 1mm thick discs. All samples were stained directly after printing, using calcein, showing live cells in green. Using ImageJ, the distance between fibers was calculated: d(D1)= 195.14±25.4µm and d(D2)=381.7±25.97µm. (c) After printing, 3D printed samples were incubated for 48h in serum free media. After 48h, the media was collected and the ECs from the samples were magnetically sorted. a).

Migration Assay. The scratch wound assay is a simple, quick and inexpensive method to quantify ECs migration. It is based on the ability of EC to fill an area that has been mechanically 'wounded' using a pipette tip on a confluent monolayer of ECs [56]. HUVECs were seeded in 48 well plates at a density of 30,000 cells per well, and incubated for 24h or until a uniform monolayer was formed. The monolayer was then "scratched" using a pipette tip to create a linear gap through the middle of each well. Medium (EBM-2, CdM or EVs) was added. Images of the wells were taken using an inverted microscope (Nikon Eclipse Ti2) after 0h and 12h of incubation. Pictures were analyzed using ImageJ to determine the overall gap closure, as previously described [57].

Tube Formation Assay. In vitro assays that simulate the formation of capillary-like structures can be used to investigate late stages of the angiogenic process [196]. 96 well plate was coated with 35 µl of Matrigel (Corning, NY) and allowed to crosslink for

30min at 37°C. HUVECs were seeded in coated 96 well plates at a density of 15,000 cells per well and incubated for 18h. Images of the wells were taken using an inverted microscope (Nikon Eclipse Ti2) and analyzed using ImageJ and Angiogenesis Analyzer plugin [197] to measure the confluency (i.e cell surface area) (Supplemental **Figure 12: Methods. (a) Chart showing the different experimental groups: Endothelial Cells (ECs), Mesenchymal Stem Cells (MSCs), Mixed, and Separated** with a distance of 0µm (D0), 200µm (D1), 400µm (D2) between fibers. ECs/MSCs groups are made of adjacent fibers containing only ECs/MSCs, respectively. The bioink for the mixed group contains both ECs/MSCs, and the fibers are also printed adjacent to each other. For the D0, D1, D2 groups, ECs and MSCs are encapsulated in different bioinks, and the fibers are printed alternatively and with a distance of 0, 200, 400µm between them. (b) Micrographs of 3D printed samples (D0, D1, D2). All samples are 8mm diameter and 1mm thick discs. All samples were stained directly after printing, using calcein, showing live cells in green. Using ImageJ, the distance between fibers was calculated: d(D1)= 195.14±25.4µm and d(D2)=381.7±25.97µm. (c) After printing, 3D printed samples were incubated for 48h in serum free media. After 48h, the media was collected and the ECs from the samples were magnetically sorted. a).

Permeability Assay. 24 well plates and 0.4-mm pore size inserts were obtained from BD Biosciences. HUVECs were seeded at 60,000 cells per insert well in a total volume of 1.5mL of EBM-2 media and incubated overnight to allow the cell to form a uniform monolayer. HUVECs monolayer permeability was tested by adding 150 µL of 10 mg/mL 40-kDa fluorescein isothiocyanate (FITC)-Dextran (Sigma-Aldrich) to the

upper chamber of each well. Media samples were taken in the bottom chamber of the well after 5, 60, 120, 240min. Measurements were determined with a Spark Multimode Microplate Reader (Tecan) using excitation and emission wavelengths of 485 and 530nm, respectively.

Statistical Analysis

Data were analyzed using single factor analysis of variance (ANOVA) followed by Tukey's Multiple Comparison Test assuming normal data distribution with a confidence of 95% ($p<0.05$).

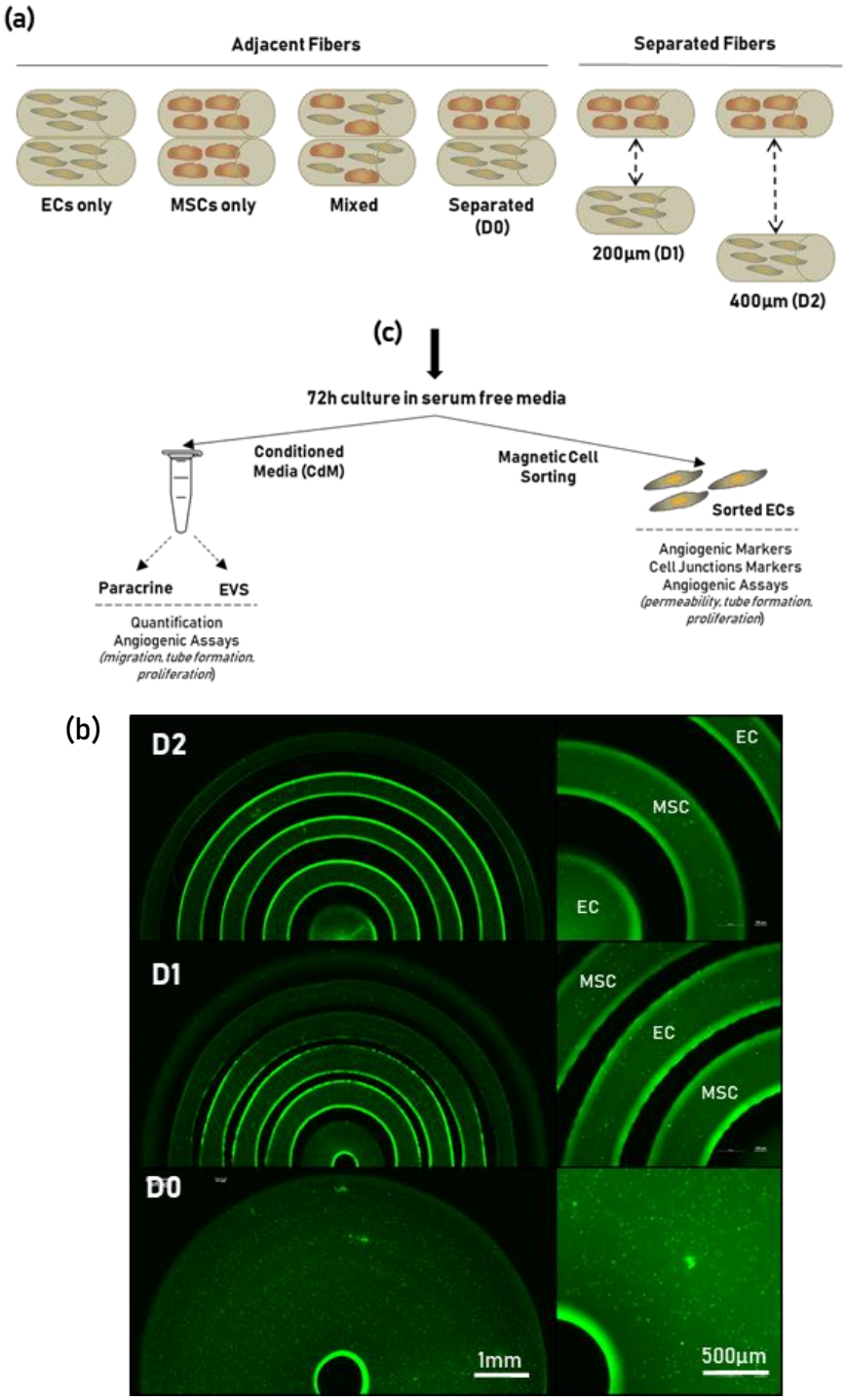

Figure 12: Methods. (a) Chart showing the different experimental groups: Endothelial Cells (ECs), Mesenchymal Stem Cells (MSCs), Mixed, and Separated with a distance of 0µm (D0), 200µm (D1), 400µm (D2) between fibers. ECs/MSCs groups are made of adjacent fibers containing only ECs/MSCs, respectively. The bioink for the mixed group contains both ECs/MSCs, and the fibers are also printed adjacent to each other. For the D0, D1, D2 groups, ECs and MSCs are encapsulated in different bioinks, and the fibers are printed alternatively and with a distance of 0, 200, 400µm between them. (b) Micrographs of 3D printed samples (D0, D1, D2). All samples are 8mm diameter and 1mm thick discs. All samples were stained directly after printing, using calcein, showing live cells in green. Using ImageJ, the distance between fibers was calculated: d(D1)= 195.14±25.4µm and d(D2)=381.7±25.97µm. (c) After printing, 3D printed samples were incubated for 48h in serum free media. After 48h, the media was collected and the ECs from the samples were magnetically sorted.

Results and Discussion

HUVECs grown ≤200μm from ECs condition show characteristics of later stage angiogenesis.

The first objective of this work was to study the angiogenic potential of ECs grown in different co-culture conditions, i.e. separated from MSCs by various distances (0, 200 μm, 400 μm). After 48h of incubation, cells were isolated from the 3D printed samples (Fig. I). HUVECs uniformly express high levels of CD31. This marker was used to positively select HUVECs from MSC-HUVEC mixed cultures using MACS. As determined by fluorescence-activated cell sorting analysis, MACS separation of MSC-HUVEC cocultures yields a very pure population of CD31 HUVECs (Fig. IIb) that was subsequently tested using qPCR and angiogenic assays.

Figure 13: ECs grown in close (≤200μm) coculture condition show characteristics of a later stage angiogenesis. (a) Schematic of the experiment. Cells were collected from the 3D printed samples after 48h of incubation. HUVECs were sorted using CD31 MACS, and used in subsequent experiments. (b) FACS analysis, pre and post-separation. The bottom row confirms the positive selection of HUVECs (c) Rt-PCR showed an increase in gene expression of VEGF and FGF-2 for cells isolated from D2 samples and an increase in the fold change in mRNA of Ang-1 for cells isolated from D0/D1 samples. (d) Cell confluency after 24h of incubation. D2 cells exhibit a significantly higher proliferation rate than the other groups. (e) Permeabilization Assay. Diffusion of Dextran-FITC was observed through a confluent monolayer of HUVECs. Cells isolated from D2 samples showed the highest permeability. Rt PCR

showed an increase in gene expression of ITGA5 for the same cells. c shows the expression of three angiogenic markers (VEGFA, FGF2, and ANG1) in all experimental groups. ECs grown by themselves were used as a control. All three groups with separated cell populations (D0, D1, and D2) showed an increase in gene expression of VEGF-A and FGF-2 when compared to the mixed group; with D2 samples showing the most up-regulation of both genes. However, only D0 and D1 samples showed an important increase in fold change for Ang-1. Sorted HUVECs were also used to study proliferation (Fig. IId). Cells were seeded in well plates at the same density, and confluency was measured after 24h of incubation. P4 HUVECs in growth media were used as a positive control, and P4 HUVECs with unsupplemented basal media were used as a negative control. Both mixed and D2 samples showed a significant increase in confluency ($p<0.05$) when compared to the positive control. D2 sample's cells showed the most mitotic activity, with a significantly higher proliferation rate.

rt-PCR was also performed to study the expression of genes associated with cellular junctions: ITGA5 (integrin) and CDH5 (VE-cadherin). VE-cadherin was the most up-regulated in D0 and D1 groups while ITGA3 was up-regulated with a higher expression in D2 groups (Fig. IIe). Finally, isolated and sorted HUVECs were grown to confluence on a transwell membrane and transport of Dextran-FITC across the monolayer was measured for 4h. **Figure 13: ECs grown in close (≤200μm) coculture condition show characteristics of a later stage angiogenesis.** (a) Schematic of the experiment. Cells were collected from the 3D printed samples after 48h of incubation. HUVECs were sorted using CD31 MACS, and used in subsequent experiments. (b) FACS

analysis, pre and post-separation. The bottom row confirms the positive selection of HUVECs (c) Rt-PCR showed an increase in gene expression of VEGF and FGF-2 for cells isolated from D2 samples and an increase in the fold change in mRNA of Ang-1 for cells isolated from D0/D1 samples. (d) Cell confluency after 24h of incubation. D2 cells exhibit a significantly higher proliferation rate than the other groups. (e) Permeabilization Assay. Diffusion of Dextran-FITC was observed through a confluent monolayer of HUVECs. Cells isolated from D2 samples showed the highest permeability. Rt PCR showed an increase in gene expression of ITGA5 for the same cells. e shows that monolayers, from cells isolated from D2 samples, were significantly the most permeable than monolayers from D0 and D1 cells.

Angiogenesis is a complex, multistep process that includes endothelial cell proliferation, guided migration, the formation of tubular structures, stabilization of newly formed vessels by deposition of the basement membrane, and finally the recruitment of perivascular supporting cells [198,199]. This process is highly regulated and involves numerous factors [40]. In response to angiogenic stimuli, such as VEGF or FGF-2, ECs turn from a quiescent to an active phenotype characterized by a high mitotic index and increased capacity for migration and matrix proteolysis [200]. Proteolytic enzymes produced and secreted by endothelial cells, such as Matrix metalloproteinase (MMP) family members, lead to cell-directed matrix degradation and remodeling, and they further growth factor delivery of matrix-bound growth factors. The early stages of angiogenesis, proliferation, and migration, in addition to VEGF and FGF-2, are also regulated by angiopoietin-2 (Ang-2). Ang-2 released from activated ECs can bind to

its receptor Tie-2, promoting vascular destabilization and a change in ECs adhesive properties [201].

VE-cadherin is an adhesion molecule that mediates cell-to-cell contact between endothelial cells and not only plays a relevant role in the maintenance of vascular integrity but also limits endothelial cell proliferation [202]. When ECs migrate during vessel sprouting, VE-cadherin junctions are temporarily dissolved. Once tubular structures are formed ECs suppress their motile phenotype and new adhesive interactions are established [203]. Integrins, in particular, the α5 subunits, are cell-surface receptors of specific ECM molecules that assist ECs to build new vessels and are strongly linked to the initial steps of angiogenesis. Integrins expressed by ECs is stimulated by angiogenic growth factors, such as FGF-2 [204], and facilitate EC adhesion to the extracellular matrix and their migration [205]. Ang-1, a later marker of angiogenesis, exerts a vessel-sealing effect, by stabilizing the endothelium and reducing integrins expression [206].

The results presented in **Figure 13: ECs grown in close (≤200μm) coculture condition show characteristics of a later stage angiogenesis.** (a) Schematic of the experiment. Cells were collected from the 3D printed samples after 48h of incubation. HUVECs were sorted using CD31 MACS, and used in subsequent experiments. (b) FACS analysis, pre and post-separation. The bottom row confirms the positive selection of HUVECs (c) Rt-PCR showed an increase in gene expression of VEGF and FGF-2 for cells isolated from D2 samples and an increase in the fold change in mRNA of Ang-1 for cells isolated from D0/D1 samples. (d) Cell confluency after 24h of incubation. D2 cells

exhibit a significantly higher proliferation rate than the other groups. (e) Permeabilization Assay. Diffusion of Dextran-FITC was observed through a confluent monolayer of HUVECs. Cells isolated from D2 samples showed the highest permeability. Rt PCR showed an increase in gene expression of ITGA5 for the same cells. suggest that HUVECs grown the farther apart from MSCs (D2) are at an earlier stage of angiogenesis (migration/proliferation) than D0/D1 cells. Indeed, results showed an increase in the up-regulation of VEGF, FGF-2, and ITGA3 (integrins) but a smaller fold change in the expression of VE-Cadherin and Ang-1. HUVECs isolated from D2 samples were also still highly proliferative when compare to D0/D1 cells. On the contrary, HUVECs incubated closer ($\leq$200μm) to MSCs, started to show signs of stabilization, mainly an increase in Ang-1 and VE-cadherin expression.

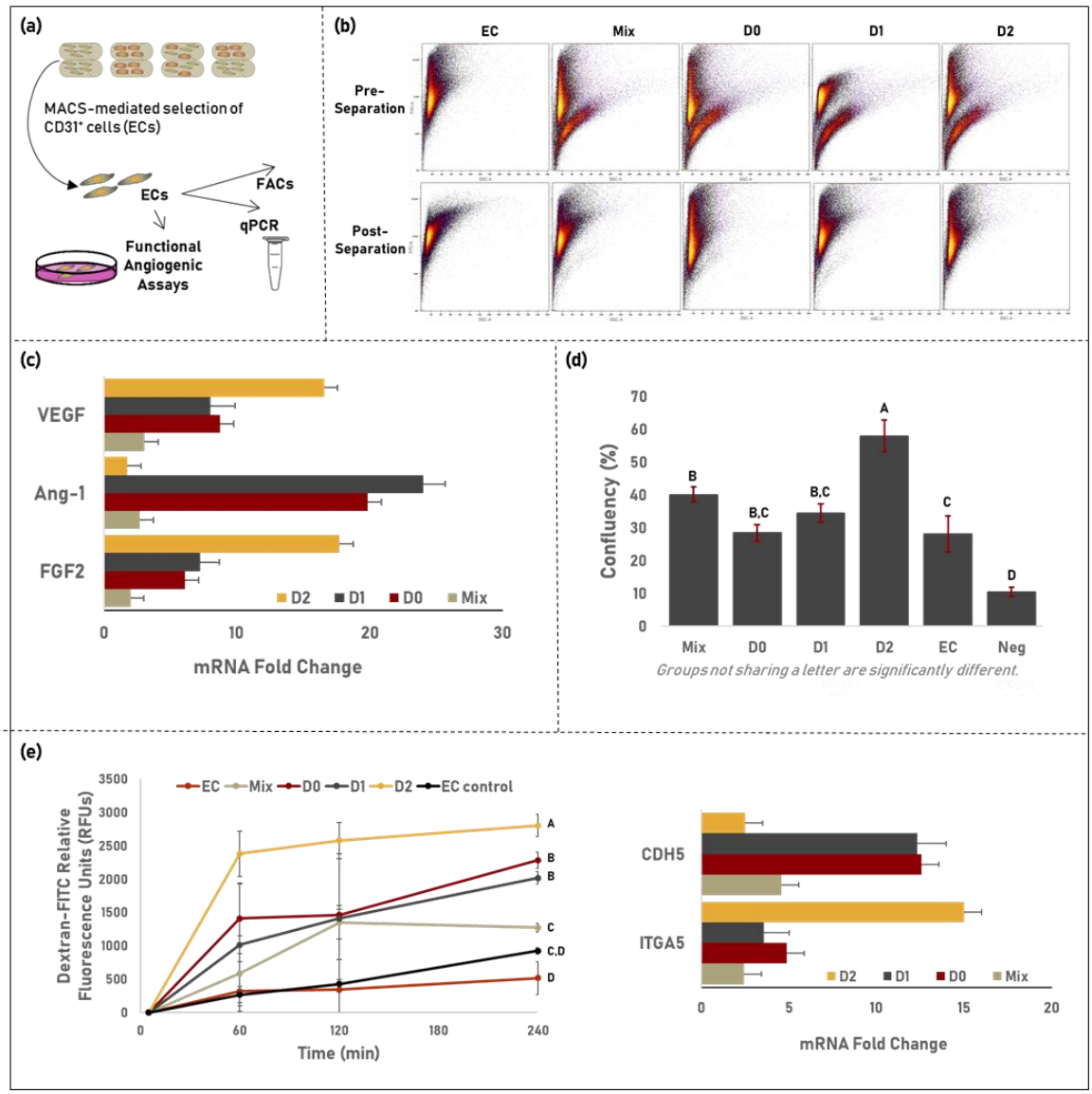

Figure 13: ECs grown in close (≤200µm) coculture condition show characteristics of a later stage angiogenesis. (a) Schematic of the experiment. Cells were collected from the 3D printed samples after 48h of incubation. HUVECs were sorted using CD31 MACS, and used in subsequent experiments. (b) FACS analysis, pre and post-separation. The bottom row confirms the positive selection of HUVECs (c) Rt-PCR showed an increase in gene expression of VEGF and FGF-2 for cells isolated from D2 samples and an increase in the fold change in mRNA of Ang-1 for cells isolated from D0/D1 samples. (d) Cell confluency after 24h of incubation. D2 cells exhibit a significantly higher proliferation rate than the other groups. (e) Permeabilization Assay. Diffusion of Dextran-FITC was observed through a confluent monolayer of HUVECs. Cells isolated from D2 samples showed the highest permeability. Rt PCR showed an increase in gene expression of ITGA5 for the same cells.

The crosstalk between hMSC and HUVECs is regulated by the separation and distance of cell populations.

The second objective of this work was to investigate whether several soluble factors which may influence HUVECs behavior are differentially secreted by cells grown in different 3D printed coculture for 48h. The concentration of three common growth factors (VEGFA, FGF2, and Ang-1) was measured using ELISA (**Figure 14: The crosstalk between hMSC and HUVECs is regulated by the separation and distance of cell populations.** (a) Schematic of the experiments. After 48h of incubation, CdM was collected and concentrated. Different growth factors concentration was measured using ELISAs. Finally the CdM was used to supplement media in functional Angiogenic assays. (b) Concentration of VEGFA, FGF-2 and Ang-1 in CdM from all experimental groups. For each growth factor, groups not sharing a letter are statistically different. Paracrine secretions were significantly increased in coculture groups where HUVECs were separated from MSCs (D0, D1). (c) CdM was used to supplement media in a proliferation assay. HUVECs confluency after 24h was measured. No statistical difference was observed between coculture groups. (d) CdM was used to supplement media for migration assay. Picture of the wound were taken 12h after "scratching" a confluent monolayer of HUVECs, and the wound closure was calculated. Groups incubated with CdM from coculture in which HUVECs and MSCs were grown the farther apart (D2) show a significant increase in migratory activity. (e) CdM was used to supplement media for a tube formation assay. HUVECs incubated

with CdM from coculture in which HUVECs and MSCs were grown separated but close (<200 µm) (D0, D1) formed a significantly longer network.b).

Results indicates a significant increase ($p<0.05$) in VEGFA and FGF2 secretions between MSCs cultured in isolation (731.03 pg/ml and 495.43 pg/ml respectively) and ECs cultured in isolation (306.26 pg/ml and 227.44 pg/ml respectively). In addition, VEGFA and FGF2 were secreted at a significant higher rate by HUVECs and MSCs in "mixed" coculture than HUVECs alone; both concentrations were even higher than the average of ECs alone and MSCs alone, confirming that co-culture improves paracrine secretion of ECs. Those findings are widely supported by literature: MSCs have been shown to be pro-angiogenic, and be able to activate ECs that will in return secrete more VEGFA and FGF2 [207–209]. The levels of VEGFA and FGF2 in D0/D1 CdM was also significantly higher than the ones from "mixed" cocultures. In addition, Ang-1 levels are significantly higher in D0/D1 groups ($p<0.05$). Those results match the qPCR results found in **Figure 13: ECs grown in close (≤200µm) coculture condition show characteristics of a later stage angiogenesis.** (a) Schematic of the experiment. Cells were collected from the 3D printed samples after 48h of incubation. HUVECs were sorted using CD31 MACS, and used in subsequent experiments. (b) FACS analysis, pre and post-separation. The bottom row confirms the positive selection of HUVECs (c) Rt-PCR showed an increase in gene expression of VEGF and FGF-2 for cells isolated from D2 samples and an increase in the fold change in mRNA of Ang-1 for cells isolated from D0/D1 samples. (d) Cell confluency after 24h of incubation. D2 cells exhibit a significantly higher proliferation rate than the other groups. (e) Permeabilization

Assay. Diffusion of Dextran-FITC was observed through a confluent monolayer of HUVECs. Cells isolated from D2 samples showed the highest permeability. Rt PCR showed an increase in gene expression of ITGA5 for the same cells. : D0/D1 coculture cells show both an up-regulation of Ang-1 gene and an increased secretion in Ang-1 when compared to cells from D2 groups. However, D2 CdM contained significantly lower levels of both VEGFA and FGF2 ($p<0.05$), while it was previously shown in **Figure 13: ECs grown in close (≤200µm) coculture condition show characteristics of a later stage angiogenesis.** (a) Schematic of the experiment. Cells were collected from the 3D printed samples after 48h of incubation. HUVECs were sorted using CD31 MACS, and used in subsequent experiments. (b) FACS analysis, pre and post-separation. The bottom row confirms the positive selection of HUVECs (c) Rt-PCR showed an increase in gene expression of VEGF and FGF-2 for cells isolated from D2 samples and an increase in the fold change in mRNA of Ang-1 for cells isolated from D0/D1 samples. (d) Cell confluency after 24h of incubation. D2 cells exhibit a significantly higher proliferation rate than the other groups. (e) Permeabilization Assay. Diffusion of Dextran-FITC was observed through a confluent monolayer of HUVECs. Cells isolated from D2 samples showed the highest permeability. Rt PCR showed an increase in gene expression of ITGA5 for the same cells. that the gene for both those growth factors was the most up-regulated. This suggests that genetic material is not being transduced into proteins or that VEGFA and FGFs are not being secreted via paracrine signaling by the cells in the D2 group, but most likely using another mode of cell-cell communication, such as the exchange of exosomes.

A second set of experiments was conducted to investigate whether cell viability (**Figure 14: The crosstalk between hMSC and HUVECs is regulated by the separation and distance of cell populations.** (a) Schematic of the experiments. After 48h of incubation, CdM was collected and concentrated. Different growth factors concentration was measured using ELISAs. Finally the CdM was used to supplement media in functional Angiogenic assays. (b) Concentration of VEGFA, FGF-2 and Ang-1 in CdM from all experimental groups. For each growth factor, groups not sharing a letter are statistically different. Paracrine secretions were significantly increased in coculture groups where HUVECs were separated from MSCs (D0, D1). (c) CdM was used to supplement media in a proliferation assay. HUVECs confluency after 24h was measured. No statistical difference was observed between coculture groups. (d) CdM was used to supplement media for migration assay. Picture of the wound were taken 12h after "scratching" a confluent monolayer of HUVECs, and the wound closure was calculated. Groups incubated with CdM from coculture in which HUVECs and MSCs were grown the farther apart (D2) show a significant increase in migratory activity. (e) CdM was used to supplement media for a tube formation assay. HUVECs incubated with CdM from coculture in which HUVECs and MSCs were grown separated but close (<200 µm) (D0, D1) formed a significantly longer network.c) and migration (**Figure 14: The crosstalk between hMSC and HUVECs is regulated by the separation and distance of cell populations.** (a) Schematic of the experiments. After 48h of incubation, CdM was collected and concentrated. Different growth factors concentration was measured using ELISAs. Finally the CdM was used to supplement

media in functional Angiogenic assays. (b) Concentration of VEGFA, FGF-2 and Ang-1 in CdM from all experimental groups. For each growth factor, groups not sharing a letter are statistically different. Paracrine secretions were significantly increased in coculture groups where HUVECs were separated from MSCs (D0, D1). (c) CdM was used to supplement media in a proliferation assay. HUVECs confluency after 24h was measured. No statistical difference was observed between coculture groups. (d) CdM was used to supplement media for migration assay. Picture of the wound were taken 12h after "scratching" a confluent monolayer of HUVECs, and the wound closure was calculated. Groups incubated with CdM from coculture in which HUVECs and MSCs were grown the farther apart (D2) show a significant increase in migratory activity. (e) CdM was used to supplement media for a tube formation assay. HUVECs incubated with CdM from coculture in which HUVECs and MSCs were grown separated but close (<200 μm) (D0, D1) formed a significantly longer network.d) of HUVECs were modulated by CdM from different co-culture conditions. The proliferation of HUVECs was significantly stimulated when cultured with CdM media regardless of the type of coculture, as compared to the negative control or CdM from ECs and MSCs cultured in isolation. However, no significant difference was observed between groups supplemented with CdM from "mixed", D0, D1 and D2 cocultures. HUVEC migratory activity when cultured with CdM increased with distance between co-cultured HUVECs and hMSC. Quantification of the invaded area indicated that wound closure was significantly higher in D2 co-cultures ($p<0.05$) than D0 or "mixed" cocultures.

We then investigated whether tube-like structures are differentially generated in HUVECs cultures incubated in growth media supplemented with CdM (**Figure 14: The crosstalk between hMSC and HUVECs is regulated by the separation and distance of cell populations.** (a) Schematic of the experiments. After 48h of incubation, CdM was collected and concentrated. Different growth factors concentration was measured using ELISAs. Finally the CdM was used to supplement media in functional Angiogenic assays. (b) Concentration of VEGFA, FGF-2 and Ang-1 in CdM from all experimental groups. For each growth factor, groups not sharing a letter are statistically different. Paracrine secretions were significantly increased in coculture groups where HUVECs were separated from MSCs (D0, D1). (c) CdM was used to supplement media in a proliferation assay. HUVECs confluency after 24h was measured. No statistical difference was observed between coculture groups. (d) CdM was used to supplement media for migration assay. Picture of the wound were taken 12h after "scratching" a confluent monolayer of HUVECs, and the wound closure was calculated. Groups incubated with CdM from coculture in which HUVECs and MSCs were grown the farther apart (D2) show a significant increase in migratory activity. (e) CdM was used to supplement media for a tube formation assay. HUVECs incubated with CdM from coculture in which HUVECs and MSCs were grown separated but close (<200 µm) (D0, D1) formed a significantly longer network.e). Tube formation assays showed that HUVECs grown with medium supplemented with CdM from all coculture groups self-assembled and elongated, forming a capillary-like network with typically closed structures similar to the ones observed in the positive control group. Incubation of

HUVECs with CdM from D0 and D1 groups resulted in a longer network of tube-like structures.

Those findings seem to support the data collected in **Figure 13: ECs grown in close (≤200μm) coculture condition show characteristics of a later stage angiogenesis.** (a) Schematic of the experiment. Cells were collected from the 3D printed samples after 48h of incubation. HUVECs were sorted using CD31 MACS, and used in subsequent experiments. (b) FACS analysis, pre and post-separation. The bottom row confirms the positive selection of HUVECs (c) Rt-PCR showed an increase in gene expression of VEGF and FGF-2 for cells isolated from D2 samples and an increase in the fold change in mRNA of Ang-1 for cells isolated from D0/D1 samples. (d) Cell confluency after 24h of incubation. D2 cells exhibit a significantly higher proliferation rate than the other groups. (e) Permeabilization Assay. Diffusion of Dextran-FITC was observed through a confluent monolayer of HUVECs. Cells isolated from D2 samples showed the highest permeability. Rt PCR showed an increase in gene expression of ITGA5 for the same cells. . D0/D1 CdM promotes preferentially tube formation, a later stage of angiogenesis, due in part to a significant increase in Ang-1 paracrine secretion. While CdM from D2 samples contains a lower concentration of VEGF/FGF than D0 or D1, still increased HUVECs significantly migration in a wound assay. This seems to further confirm that HUVECs grew in close (≤200μm) coculture condition show characteristics of a later stage angiogenesis.

Since MSCs cultured in isolation produced more VEGFA and FGF2 than HUVECs cultured in isolation, separating cell populations in different fibers (D0, D1, D2) could

create a gradient of paracrine secretions. And this gradient could also vary depending on the distance between fibers. This phenomenon could explain the difference in VEGF/FGF secretion between "mixed", D0, D1, and D2 groups. Endothelial cell migration is mediated by VEGF gradients which orientates, attracts, and induces proliferation of new blood vessels [210–212]. Furthermore, the shape of the VEGFA gradient can dictate the proliferation and migratory response exhibited by endothelial cells [213]. Models predict that VEGF distribution along the gradient forms an uneven slope: cells close to the VEGF-A source would be in an exponential high concentration zone, while cells further away from the source would be in a zone of linear low concentration [214]. In addition, analysis of cell migration in different regions of the applied gradients showed that cells efficiently interpret the positional information provided by the gradients [213]: responses for both VEGFA and FGF2 were more pronounced in the exponential regions of the gradients compared with the linear regions. Based on those findings, we could hypothesize that D0/D1 cocultures formed stronger gradients, eliciting a stronger response from HUVECs to MSCs paracrine secretion.

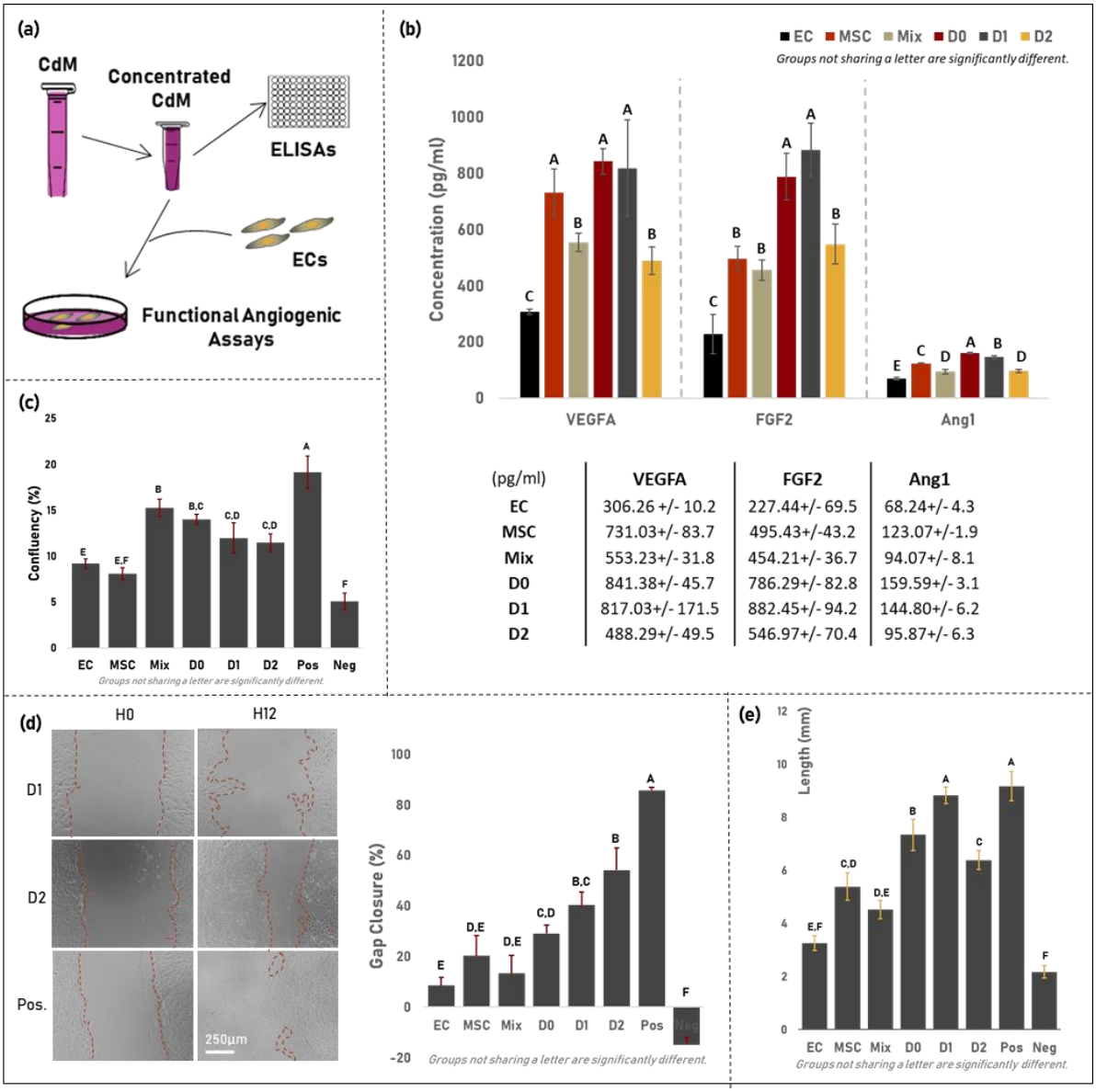

(pg/ml)	VEGFA	FGF2	Ang1
EC	306.26 +/- 10.2	227.44+/- 69.5	68.24+/- 4.3
MSC	731.03+/- 83.7	495.43+/-43.2	123.07+/-1.9
Mix	553.23+/- 31.8	454.21+/- 36.7	94.07+/- 8.1
D0	841.38+/- 45.7	786.29+/- 82.8	159.59+/- 3.1
D1	817.03+/- 171.5	882.45+/- 94.2	144.80+/- 6.2
D2	488.29+/- 49.5	546.97+/- 70.4	95.87+/- 6.3

Figure 14: The crosstalk between hMSC and HUVECs is regulated by the separation and distance of cell populations. (a) Schematic of the experiments. After 48h of incubation, CdM was collected and concentrated. Different growth factors concentration was measured using ELISAs. Finally the CdM was used to supplement media in functional Angiogenic assays. (b) Concentration of VEGFA, FGF-2 and Ang-1 in CdM from all experimental groups. For each growth factor, groups not sharing a letter are statistically different. Paracrine secretions were significantly increased in coculture groups where HUVECs were separated from MSCs (D0, D1). (c) CdM was used to supplement media in a proliferation assay. HUVECs confluency after 24h was measured. No statistical difference was observed between coculture groups. (d) CdM was used to supplement media for migration assay. Picture of the wound were taken 12h after "scratching" a confluent monolayer of HUVECs, and the wound closure was calculated. Groups incubated with CdM from coculture in which HUVECs and MSCs were grown the farther apart (D2) show a significant increase in migratory activity. (e) CdM was used to supplement media for a tube formation assay. HUVECs incubated with CdM from coculture in which HUVECs and MSCs were grown separated but close (<200 µm) (D0, D1) formed a significantly longer network.

EV cargo increases with distance between cell populations and promotes early angiogenesis.

The third objective of this work was to study the angiogenic potential of extracellular vesicles (EVs) exchanged between cell populations. Many studies indicate EVs is a key mediator of the therapeutic functions imparted by cell therapies [215–217]. Thus, we investigated whether EVs play a role in the angiogenic effects observed with CdM. EVs were isolated from the CdM using differential centrifugation and quantified (**Figure 15: EVs cargo increases with distance between cell populations and promotes early angiogenesis.** (a) EVs and protein per EVs quantification. Proteins concentration per EVs increases with the distance between cell populations in co-culture. (b) Schematics of experiment. After 48h of incubation, CdM was collected from all experimental groups and EVs were collected by centrifugation. EVs were then quantified and their Angiogenic potential was evaluated in functional Angiogenic assays. (c) Tube Formation Assay. EVs supplemented media was used to incubate HUVECs on Matrigel. Total length of network formed by tube like structures was measured. No statistical difference was observed between coculture groups. (d) Proliferation Assay. EVs supplemented media was used to grown HUVECs. Confluency was measured after 24 and 48h of incubation. HUVECs grown with D2 EVs showed a higher proliferation rate. (e) Migration Assay. HUVECs grown in D2 EVs supplemented media showed a faster migration. a). The results showed a significant increase ($p<0.05$) in protein concentration per EVs in all separated co-culture groups (D0, D1, D2) as compared to EVs only. EVs collected from D2 CdM showed the most increase

in protein concentration when compared to D0 or D1 groups. Which seems to suggest that EVs cargo content increases with the distance between HUVECs and MSCs. **Figure 13: ECs grown in close (≤200µm) coculture condition show characteristics of a later stage angiogenesis.** (a) Schematic of the experiment. Cells were collected from the 3D printed samples after 48h of incubation. HUVECs were sorted using CD31 MACS, and used in subsequent experiments. (b) FACS analysis, pre and post-separation. The bottom row confirms the positive selection of HUVECs (c) Rt-PCR showed an increase in gene expression of VEGF and FGF-2 for cells isolated from D2 samples and an increase in the fold change in mRNA of Ang-1 for cells isolated from D0/D1 samples. (d) Cell confluency after 24h of incubation. D2 cells exhibit a significantly higher proliferation rate than the other groups. (e) Permeabilization Assay. Diffusion of Dextran-FITC was observed through a confluent monolayer of HUVECs. Cells isolated from D2 samples showed the highest permeability. Rt PCR showed an increase in gene expression of ITGA5 for the same cells. indicated that ECs grown in D2 coculture conditions showed an important up-regulation of VEGFA and FGF2 genes. However, no significant increase in VEGF or FGF secretions were observed in the CdM (**Figure 14: The crosstalk between hMSC and HUVECs is regulated by the separation and distance of cell populations.** (a) Schematic of the experiments. After 48h of incubation, CdM was collected and concentrated. Different growth factors concentration was measured using ELISAs. Finally the CdM was used to supplement media in functional Angiogenic assays. (b) Concentration of VEGFA, FGF-2 and Ang-1 in CdM from all experimental groups. For each growth factor, groups not sharing a

letter are statistically different. Paracrine secretions were significantly increased in coculture groups where HUVECs were separated from MSCs (D0, D1). (c) CdM was used to supplement media in a proliferation assay. HUVECs confluency after 24h was measured. No statistical difference was observed between coculture groups. (d) CdM was used to supplement media for migration assay. Picture of the wound were taken 12h after "scratching" a confluent monolayer of HUVECs, and the wound closure was calculated. Groups incubated with CdM from coculture in which HUVECs and MSCs were grown the farther apart (D2) show a significant increase in migratory activity. (e) CdM was used to supplement media for a tube formation assay. HUVECs incubated with CdM from coculture in which HUVECs and MSCs were grown separated but close (<200 µm) (D0, D1) formed a significantly longer network.b). Altogether, it would indicate that most likely VEGF/FGF proteins or nucleic acids regulating these pathways were preferentially loaded into EVs in D2 cocultures. We could hypothesize that EVs secretion is preferred as a mode of cell-cell communication when cell populations are further apart.

Functional angiogenic assays were performed to assess the angiogenic potential of EVs only. Media supplemented with EVs (normalized by EV protein concentration) was used to perform tube formation (**Figure 15: EVs cargo increases with distance between cell populations and promotes early angiogenesis.** (a) EVs and protein per EVs quantification. Proteins concentration per EVs increases with the distance between cell populations in co-culture. (b) Schematics of experiment. After 48h of incubation, CdM was collected from all experimental groups and EVs were collected

by centrifugation. EVs were then quantified and their Angiogenic potential was evaluated in functional Angiogenic assays. (c) Tube Formation Assay. EVs supplemented media was used to incubate HUVECs on Matrigel. Total length of network formed by tube like structures was measured. No statistical difference was observed between coculture groups. (d) Proliferation Assay. EVs supplemented media was used to grown HUVECs. Confluency was measured after 24 and 48h of incubation. HUVECs grown with D2 EVs showed a higher proliferation rate. (e) Migration Assay. HUVECs grown in D2 EVs supplemented media showed a faster migration.c), proliferation (**Figure 15: EVs cargo increases with distance between cell populations and promotes early angiogenesis.** (a) EVs and protein per EVs quantification. Proteins concentration per EVs increases with the distance between cell populations in co-culture. (b) Schematics of experiment. After 48h of incubation, CdM was collected from all experimental groups and EVs were collected by centrifugation. EVs were then quantified and their Angiogenic potential was evaluated in functional Angiogenic assays. (c) Tube Formation Assay. EVs supplemented media was used to incubate HUVECs on Matrigel. Total length of network formed by tube like structures was measured. No statistical difference was observed between coculture groups. (d) Proliferation Assay. EVs supplemented media was used to grown HUVECs. Confluency was measured after 24 and 48h of incubation. HUVECs grown with D2 EVs showed a higher proliferation rate. (e) Migration Assay. HUVECs grown in D2 EVs supplemented media showed a faster migration.d) and migration (**Figure 15: EVs cargo increases with distance between cell populations and promotes early angiogenesis.** (a) EVs and

protein per EVs quantification. Proteins concentration per EVs increases with the distance between cell populations in co-culture. (b) Schematics of experiment. After 48h of incubation, CdM was collected from all experimental groups and EVs were collected by centrifugation. EVs were then quantified and their Angiogenic potential was evaluated in functional Angiogenic assays. (c) Tube Formation Assay. EVs supplemented media was used to incubate HUVECs on Matrigel. Total length of network formed by tube like structures was measured. No statistical difference was observed between coculture groups. (d) Proliferation Assay. EVs supplemented media was used to grown HUVECs. Confluency was measured after 24 and 48h of incubation. HUVECs grown with D2 EVs showed a higher proliferation rate. (e) Migration Assay. HUVECs grown in D2 EVs supplemented media showed a faster migration.e) assays. Results indicated that media supplemented with D2 EVs significantly improved HUVECs proliferation and migration in comparison to Mix, D0, or D1. HUVECs proliferation after 24h seemed to be correlated to EV proteins concentration (r^2=0.9551) (**Figure 14: The crosstalk between hMSC and HUVECs is regulated by the separation and distance of cell populations.** (a) Schematic of the experiments. After 48h of incubation, CdM was collected and concentrated. Different growth factors concentration was measured using ELISAs. Finally the CdM was used to supplement media in functional Angiogenic assays. (b) Concentration of VEGFA, FGF-2 and Ang-1 in CdM from all experimental groups. For each growth factor, groups not sharing a letter are statistically different. Paracrine secretions were significantly increased in coculture groups where HUVECs were separated from MSCs (D0, D1). (c) CdM was

used to supplement media in a proliferation assay. HUVECs confluency after 24h was measured. No statistical difference was observed between coculture groups. (d) CdM was used to supplement media for migration assay. Picture of the wound were taken 12h after “scratching” a confluent monolayer of HUVECs, and the wound closure was calculated. Groups incubated with CdM from coculture in which HUVECs and MSCs were grown the farther apart (D2) show a significant increase in migratory activity. (e) CdM was used to supplement media for a tube formation assay. HUVECs incubated with CdM from coculture in which HUVECs and MSCs were grown separated but close (<200 μm) (D0, D1) formed a significantly longer network.d). However, no significant effect on tube formation was observed. As discussed previously, VEGF and FGF are both involved in early angiogenesis, promoting EC proliferation and migration. Those results would further suggest that either VEGF/FGF or other nucleic acids involved in these pathways were loaded in EVs for farther apart co-culture (D2).

Evidence seems to indicate that in coculture where cells are the farther apart, EVS is preferred for cell-cell communication. This could explain why angiogenesis is happening slower than groups D0, D1. This study appears to indicate that EVs are largely involved in cell-cell communication in cocultures where the cells are farther apart, while paracrine signaling via soluble proteins is dominant when the cells are closer together. The mode of cell-cell communication may dominate the rate of angiogenesis. VEGF, FGF-2, and Ang1 can act upon target cells by interacting with receptors on the cell surface. Depending on whether the function of these EVs is imparted by surface proteins or internal cargo, they may need to initially be processed before triggering a functional response, consequently resulting in delayed

angiogenesis. Thus, cocultures with cell populations closer together demonstrated later stage angiogenesis.

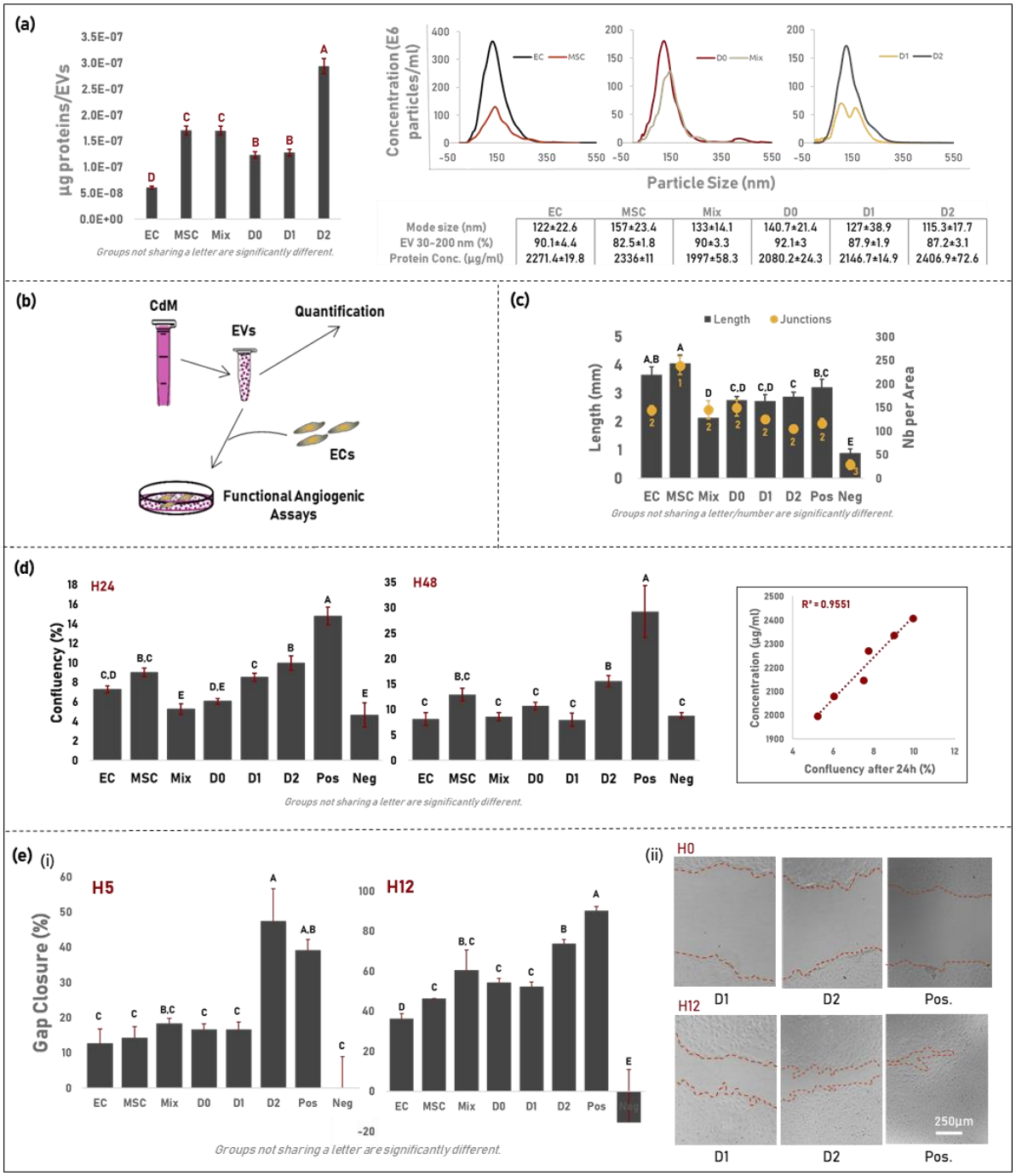

Figure 15: EVs cargo increases with distance between cell populations and promotes early angiogenesis. (a) EVs and protein per EVs quantification. Proteins concentration per EVs increases with the distance between cell populations in co-culture. (b) Schematics of experiment. After 48h of incubation, CdM was collected from all experimental groups and EVs were collected by centrifugation. EVs were then quantified and their Angiogenic potential was evaluated in functional Angiogenic assays. (c) Tube Formation Assay. EVs supplemented media was used to incubate HUVECs on Matrigel. Total length of network formed by tube like structures was measured. No statistical difference was observed between coculture groups. (d) Proliferation Assay. EVs supplemented media was used to grown HUVECs. Confluency was measured after 24 and 48h of incubation. HUVECs grown with D2 EVs showed a higher proliferation rate. (e) Migration Assay. HUVECs grown in D2 EVs supplemented media showed a faster migration.

Conclusion

These results suggest that controlling the distance between ECs and MSCs in coculture, using 3D printing, can influence angiogenesis. We showed that HUVECs grown in close (≤200μm) coculture condition presented characteristics of later stage angiogenesis: Ang-1 and VE-cadherin were upregulated, and paracrine secretion used to culture HUVECs on Matrigel formed significantly longer a network of tube-like structures. However, HUVECs grown farther apart from MSCs (400μm) showed characteristics of earlier stages of angiogenesis: both VEGF and FGF-2 were upregulated, and HUVECs grown in media supplemented with CdM or EVs from D2 groups presented a significantly higher mitotic activity and migration rate. In addition, the separation and distance between ECs and MSCs seemed to modulate cell-cell communication. In groups in which fibers were printed the farther apart (400μm), cells produced EVs with a significantly increase cargo. Finally, by modulating distance between printed fibers, results indicated that we can create different paracrine secretion gradients, hence modulate the crosstalk between HUVECS and MSCs. Further experiments should be performed to better understand the mechanism behind the phenomenon observed, such as why exactly is EVs communication is increased when cell populations are grown farther apart.

Chapter 6: Repair of Calvarial Defects in Rats with Optimized 3D Printed EC-MSCs Cocultures

Introduction

Based on the concepts and findings from Chapter 4 and Chapter 5, this study was designed to determine whether optimized concentric 3D printed (3DP) cocultures could support osteogenic differentiation and consequent bone regeneration, as well as proper neovascularization, in an *in vivo* model. A calvarial rat model was chosen as it is a well-documented model for the evaluation of bone healing. The critical size defect in rat calvaria is the smallest diameter of the intraosseous wound that does not heal spontaneously. Defects of 8 mm created surgically in the rat's calvaria by Takagi and Urist [218] showed healing by connective fibrous tissue after 6 months. The defect was reduced to 5 mm in four weeks, but no further healing of the defect was noted thereafter. In addition, Hollinger and Kleinschmidt [219] found that after 13 months of healing, an 8 mm cranial defect in Long–Evans rats did not heal spontaneously.

In this study, 3DP samples, alternating fibers containing endothelial cells (ECs) and mesenchymal stem cells (MSCs) were implanted in a calvarial rat defect, and retrieve after 12 weeks. Histological analysis was performed for identification of new osteoid matrix within the injury site and analyzed for quantification of new bone formation and new blood vessels.

Material and Methods

Cell Culture

Rat primary aortic endothelial cells (RAECs) were purchased from Cell Biologics (Chicago, IL) and cultured according to manufacturer instructions. Rat MSCs (rMSCs) were purchased from RD Systems (Minneapolis, MN) and cultured in osteogenic media for 7 days prior to implantation. The osteogenic media was formulated by supplementing growth media with 100 nM dexamethasone (Sigma, St. Louis, MO), 10 mM β-glycerophosphate (Sigma), and 173 mM ascorbic acid (Sigma). Cells were expanded on tissue culture polystyrene flasks with media changes every 3 days and grown to 80% confluency before being passaged using trypsin/EDTA. Cells at passage P4 were used for the experiments.

3D Printed Samples Preparation

Scaffolds for in vivo evaluation were fabricated using a commercial extrusion-based 3D printer (3D Bioplotter, EnvisionTEC, Gladbeck, Germany). All printing supply (30cc barrel and 200 μm/400 μm precision tips) were purchased from Nordson EFD (RI, USA).

All samples were about 0.7 mm in thickness and 8 mm in diameter (**Figure 16**). Fibrinogen and thrombin from bovine plasma were purchased from Sigma. Type A porcine gelatin (300g Bloom) was purchased from Sigma. The bioink was prepared by mixing 10 w/v% fibrinogen and 5w/v% gelatin and heating to 60°C for 15 min. Cells were passaged, suspended in media and centrifuged to form a pellet. After aspiration of the supernatant, the pellet was then suspended in fibrin bioink by manual pipetting,

until the solution was homogenous and all clumps were broken down. Fibrin bioink encapsulating $2x10^6$ rMSCs/ml or $2x10^6$ RAECs/ml were used to print experimental samples. Fibrin bioink encapsulating 2x106 rMSCs-RAECs/ml (ratio 1:1) were used to print control samples. All bioinks were loaded into separate print heads and were heated to 22°C for 30 min prior to printing. Printed constructs were crosslinked in 100 U thrombin for 30 min. All of the above was performed under sterile conditions.

Live/Dead Assay

3DP samples, prepared as explained above, were used to assess in vitro cell viability directly after printing. Cell viability was assessed using a Live/Dead assay (Invitrogen) following the manufacturer's protocol. Briefly, samples were incubated with 2 µM ethidium homodimer and 4 µM calcein AM for 1 h. Fluorescent images were taken using a confocal microscope (Leica SP5 X). Live cells appeared green while the dead ones were red.

Animal Implantation

The Institutional Animal Care and Use Committee of the University of Maryland approved the study (protocol number R-MAY-18-26), and all animals were treated in accordance with the Guide for the Care and Use of Laboratory Animals. The experiment was conducted in 30 male adult Sprague Dawley rats.

Implantation was explained elsewhere [220]. Briefly, the fur on the bridge of the snout between the eyes to the caudal end of the calvarium was shaved to expose the surgical site. Using a scalpel, an incision of approximately 1.5 cm was made over the scalp from the nasal bone to just caudal to the middle of the bregma to visualize the calvarium.

The underlying bone was exposed. The calvarium was scored with a surgical drill while being irrigated with sterile normal saline to form an 8 mm diameter defect on the sagittal suture. Once the calvarium was freed, it was raised off the dura to finish the defect. The defect was washed with sterile normal saline to remove any debris and/or bone chips. The scaffold was placed into the defects and the wound was closed over the implant using a running 4-0 monocryl suture. Control animals (CT) underwent sham surgery exactly as described but without implanting the scaffold material. For these animals undergoing cranial window implantation, after a scaffold was placed inside the defect, a circular glass coverslip was placed to cover the implant. The optical window was sealed to the skull with cyanoacrylate, covering all the exposed skull, wound margins and cover glass edges [221]. Animals were monitored daily for up to 12 weeks. No complications were reported.

Histological Analysis

At 4 and 12 days post implantation, animals were euthanized by inhalation of CO2 and the samples and surrounding bone tissue were explanted. Each explanted tissue sample was fixed in paraformaldehyde (4%), decalcified in 20% EDTA, and embedded in paraffin for histological analysis. Explanted tissue samples were prepared and sliced (15 μm slides) by Histoserv, Inc. (Germantown, MD). For histological evaluation, sections were rehydrated in consecutive ethanol washes and stained by Masson's trichrome staining and Hematoxylin/Eosin. The thickness of the defect, the length of the newly formed bone and the number of blood vessels for each sample were measured using ImageJ.

Statistical Analysis

For each animal, the length of the new bone formed was calculated over 3 different sections/samples: a total of 9 measurements (n=12) were taken for each group. For both the thickness of the defect and the number of blood vessel per area, measurements were taken in two different areas/section, with 3 sections/sample: a total of 18 measurements were taken for each group.

The ANOVA test for variance analysis was performed followed by Tukey's Multiple Comparison Test assuming normal data distribution with a confidence of 95% ($p<0.05$).

Results

Healing of critical-size bone defect on visual examination.

The aim of this chapter was to determine whether optimized concentric 3D printed (3DP) cocultures could support osteogenic differentiation and consequent bone regeneration, as well as proper neovascularization, in an in vivo model. 8-mm bone defects were created in the calvarial bones of rats. Two experimental groups and one control group were assayed at twelve weeks post calvarial defect. The cranial bones were harvested at 12 weeks after the creation of bone defects.

Implanted samples were 8 mm by 0.7 mm discs. Two experimental groups were prepared. Schematics of each are shown in **Figure 16**a. The first group (control) consisted of concentric fibers, printed using a fibrin bioink (described in Chapter 4) encapsulating both rat ECs and rat MSCs, with a ratio of 1:1. The second, experimental group consisted of concentric fibers, alternating bioink encapsulating either rat ECs or rat MSCs. Live/Dead staining was performed in order to verify the viability of the cells

post-printing, and prior to implantation. Fluorescent images showed mostly viable cells (**Figure 16**). In order to confirm the proper patterning of the cells, rMSCs and rECs were stained with Calcein AM or DAPI respectively, prior to printing. After printing, samples were imaged (**Figure 16**c).

All wounds healed without any complications, or evidence of infection. At retrieval, samples appeared to be covered by a healthy periosteum. No signs of inflammation were visible. On visual examination (**Figure 17**), the critical size defect left unfilled (CT) was not closed, the sagittal vein and peripheral blood vessels were clearly visible. New tissue formation was visible only on the edges of the defect. Defects in both 3D printed controls (CT-3DP) and experimental group (EXP-3DP) appeared to have nearly closed. However, the sagittal vein was still slightly visible in the CT-3DP group, suggesting that the newly formed tissue might be thinner than in the EXP-3DP group.

Healing of critical-size bone defect on histological analysis.

The densities of blood vessels present in all scaffolds were measured 4 weeks after implantation. Histological sections stained with HE showed relatively few blood vessels within the control scaffolds (**Figure 18**a). In contrast, 3DP scaffolds displayed a higher density of blood vessels interspersed throughout the scaffold. Quantification of blood vessels densities confirmed that 3DP-EXP scaffolds had a significantly higher blood vessel density than 3DP-CT and CT scaffolds (**Figure 18**b).

The effect of induces angiogenesis on bone tissue regeneration within the critical-sized defects after 12 weeks were analyzed next. Histological analysis of the

samples was performed using a Masson's trichrome stain. Using this method, mineralized bone is stained dark blue while osteoids, or unmineralized bone tissue, are stained pink/red. Collagen fibers are also stained blue. Cytoplasm is stained pink and cell nuclei black. Gross observations of the Masson's trichrome stained slides showed only minimal appositional bone regeneration and a thin layer of fibrous tissue and obvious defects remaining in the control group (**Figure 19**a). 3DP samples showed significantly enhanced bone growth as compared to controls ones. Histomorphometric analysis corroborated the histological findings (**Figure 19**b). The length and thickness of the newly formed bone in defect sites were calculated. The results indicated that 3DP-EXP groups were significantly thicker than the 3DP-CT and CT groups. However, the length of new bone was not significantly different than the other groups.

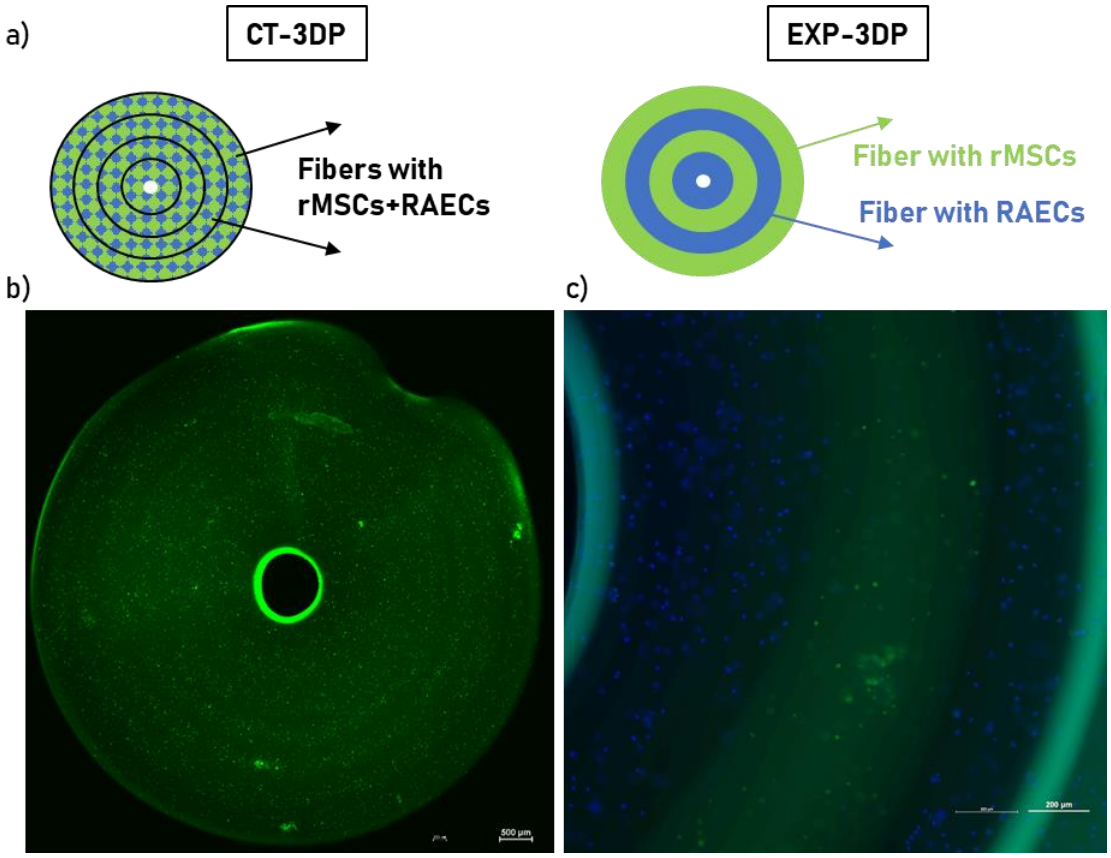

Figure 16: Methods. (a) Schematics of the **3D printed samples.** Discs were 8 mm in diameter and 0.7mm thick, and made of concentric fibers (200 µm) with no space between fibers. Control groups were printed using a bioink containing a mix of RAECs and MSCs (ratio 1:1). Experimental groups were printed using two different bioinks, one containing MSCs, the other containing RAECs; fibers were alternated. (b) Live/Dead Micrograph of 3DP samples. Live cell were stained with Calcein AM (green) and dead cells were stained with ethidium homodimer (red). Cell viability was high after printing. (c) Experimental group, MSCs were stained with Calcein AM (green) and RAECs with DAPI (blue).

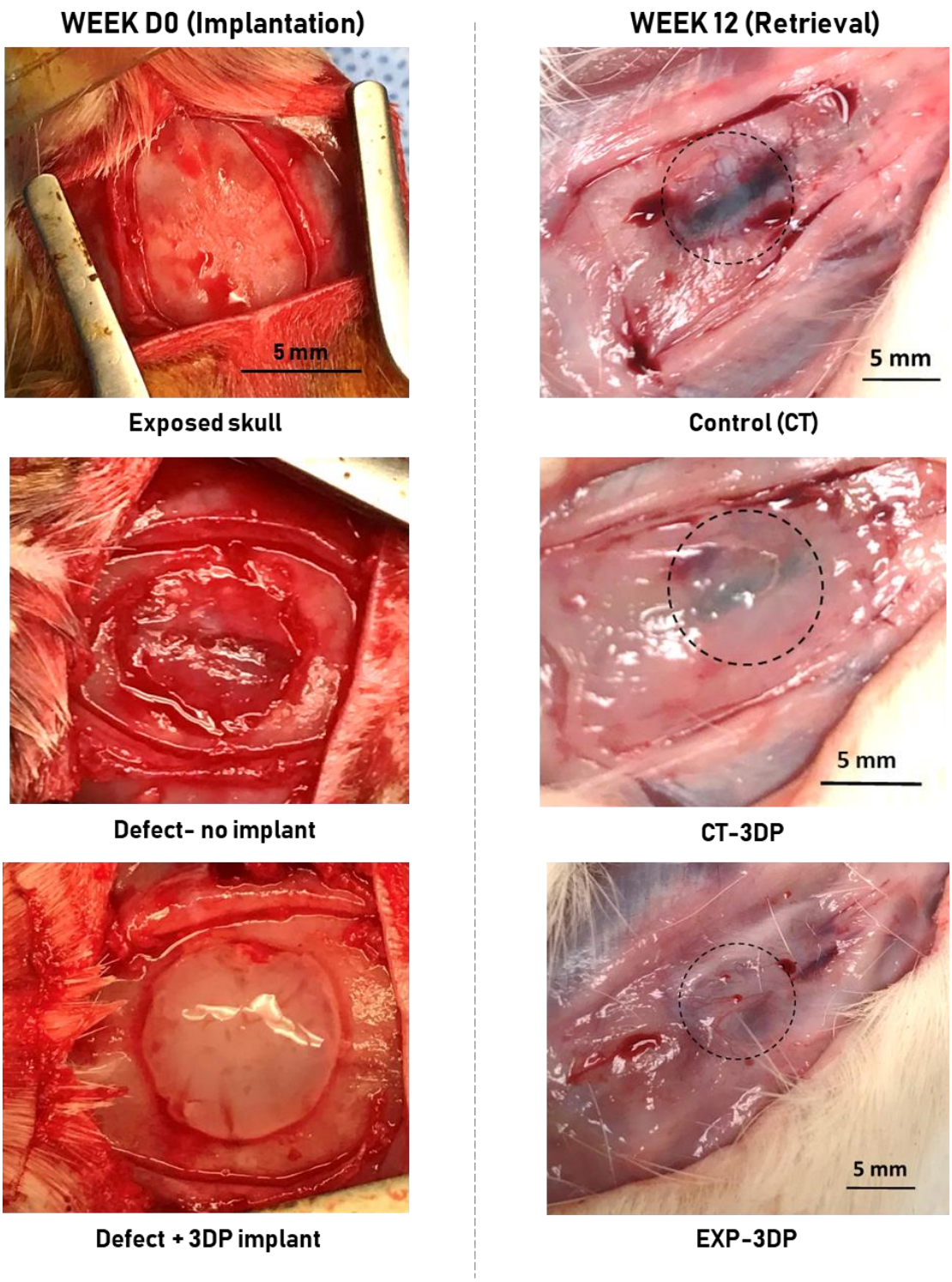

Figure 17: Sample implantation in rat calvarial defects, and extraction. The left panel shows pictures taken during surgery. In order, the exposed skull prior to drilling, the critical size defect, and finally the critical size defect filled with a 3D printed sample. Sham surgery was performed on CT group, leaving the defect empty. The right panel shows pictures taken during sample retrieval.

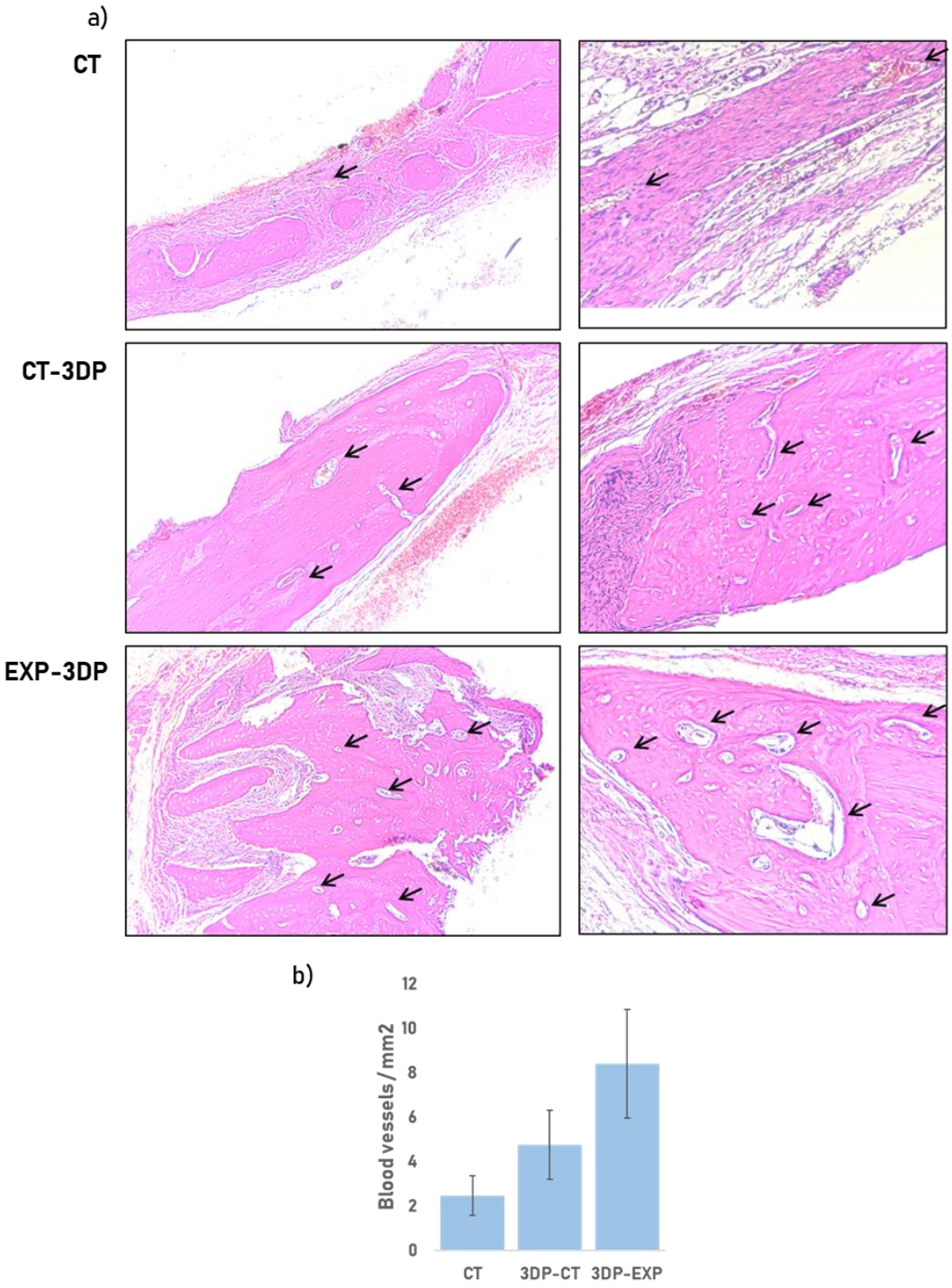

Figure 18: Optimized 3DP coculture enhanced blood vessel ingrowth after 4 weeks. (a) Representative images of HE stained slides. (b) Quantification of blood vessel densities.

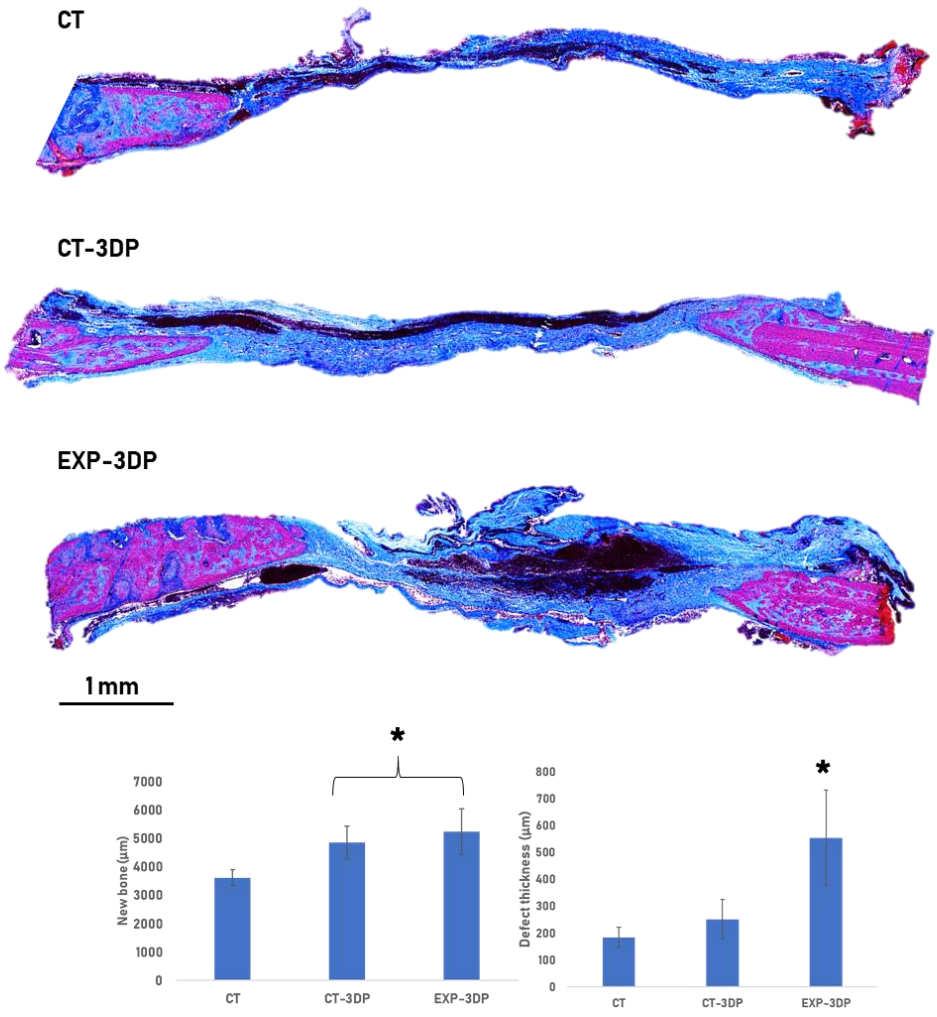

Figure 19: Representative images of Masson's trichrome stained slides. New bone formed and bone thickness were also quantified. Groups with an * are statistically different.

Conclusion

Masson's trichrome stained slices of repaired tissues showed that the EXP-3DP groups could not only stimulate regeneration of new bone but also regenerate a larger amount of bone defect than the control group. No significant difference in the amount was observed between both 3DP groups.

However, a significantly higher number of blood vessels was observed in EXP-3DP when compared to CT-3DP. This observation suggests the higher efficiency of indirect ECs/MSCs contact in prompting the release of paracrine signals that stimulate the angiogenesis of local tissues.

Chapter 7: Summary and Future Directions

Summary

In Chapter 2, we demonstrated the successful fabrication of calcium deficient hydroxyapatite microparticles, with biological properties closer to the bone than stoichiometric, commercially available hydroxyapatite. This CDHAP exhibited a well-defined 3D network of crystalline nanoplates forming mesoporous and hollow structures. The high specific area created by those structures enabled us to load VEGF with high efficiency and sustained drug release property when compared to the loading efficiency of SBp. Additionally, we demonstrated that VEGF-CDHAp could be used to improve both osteogenesis and angiogenesis in vitro. These CDHAp have held great potentials for drug-delivery applications and could be used to deliver not only VEGF but also multiple bioactive growth factors. They could find broad utility in many bone tissue engineering applications where sustained release of factors in a local environment is advantageous.

In Chapter 4, we developed and optimized a fibrin bioink, with potential applications going beyond bone tissue engineering. Fibrin is a natural polymer known to support wound healing by inducing angiogenesis and promoting cell attachment and proliferation, and therefore an attractive matrix for stem cell differentiation and tissue engineering. We also demonstrated the successful fabrication of a novel 3DP fibrin-PCL composite scaffold, with mechanical strength comparable to bone, a stable swelling behavior and cell bioactivity for the construction of bio-inspired structures.

By using 3D printing technologies, we were able to successfully patterned bioinks into varied geometries and with controlled dimensions, in order to recreate an optimal microenvironment mimicking the native natural cell pattern found in bones, to form a simplified model of osteons. These results lead us to believe that cell placement or patterning could play a critical role in neovascularization. Most importantly, the utilization of these scaffolds in constructing bio-inspired osteons for bone regeneration demonstrated a promising capacity to improve neovascularization of the construct. This bio-inspired osteon-like construct holds potential to be developed as scaffolds in vascularized bone tissue engineering.

In Chapter 5, we investigated the role of distance between cell populations, introduced via 3D printing, in ECs/MSCs crosstalk. Our results suggested that controlling the distance between ECs and MSCs in coculture, using 3D printing, could influence angiogenesis. We showed that HUVECs grown in close (≤200μm) coculture condition presented characteristics of later stage angiogenesis: Ang-1 and VE-cadherin were upregulated, and paracrine secretion used to culture HUVECs on Matrigel formed significantly longer a network of tube-like structures. In addition, the separation and distance between ECs and MSCs seemed to modulate cell-cell communication. In groups in which fibers were printed the farther apart (400μm), cells produced EVs with a significantly increase cargo. Finally, by modulating distance between printed fibers, results indicated that we could create different paracrine secretion gradients, hence modulate the crosstalk between HUVECS and MSCs. Combining the technology developed in chapter 4 and the findings of chapter 5, we determine whether optimized concentric 3D printed (3DP) cocultures could support osteogenic differentiation and

consequent bone regeneration, as well as proper neovascularization, in a critical size rat cranial defect.

Future Directions

3D printed gradient of VEGF using CDHAp

It has been shown that in order to control vascular organization, it is not so much the availability of VEGF, but the presence of gradients that controls vascular migration [222]. By creating distinct patterns of VEGF onto scaffolds or within hydrogels, gradients can be instituted, resulting in spatially driven endothelial cell elongation and branching [223,224]. The mesoporous calcium deficient hydroxyapatite developed in Chapter 2, presents high capacity for drug loading and show great potential as candidate carriers for VEGF release. The 3D printing of these osteoinductive microparticles in specific patterns could be used as a novel way to deliver gradient of VEGF to ECs and MSCs, and to improve ECs invasion and sprouting throughout a 3DP scaffold, and hence the development of a stable microvasculature.

Synergistic effect of CDHAp and ECs/MSCs coculture

In this manuscript, we focused on two avenues to improve the neovascularization of bone tissue constructs: (1) the development of osteoinductive mesoporous microparticles, and (2) the optimization of ECs/MSCs coculture, utilizing the capabilities of 3D printing, and based on a bio-inspired strategy. The next step could combine the use of both in order to demonstrate that a 3D printed osteon-like scaffold

containing MSCs, ECs, *and* CDHAp improves the formation of a pre-vascular network due to the synergetic effects of improved VEGF delivery and paracrine signaling.

Developing new bio-inspired bioinks for 3D printing

Biomimicry is based on the fact that the intrinsic properties of biomaterials need to mimic the 3D microenvironment of the native tissue in terms of topographical, biological and physicomechanical features, in order to provide instructing cues to surrounding cells to stimulate their adhesion, migration, proliferation, and differentiation. In this dissertation, we mainly focused on recreating units found in bones (osteons), i.e. in mimicking the native cell patterning of cortical bones. To do so, we used a fibrin bioink.

However, as mentioned previously, the bone extracellular matrix is a nanocomposite of organic and inorganic elements. Bones are composed of 65 % by weight of minerals, primarily carbonated apatite and 20-25% of organic components. Bone organic phase mainly consists of collagen I. In order to increase the biomimecry of our 3DP osteons, one approach would be to develop bio-inspired inks for 3D printing. An optimal strategy would be to decellularize bone natural ECM (dECM) to eliminate immunogenicity and co-print dECM with biocompatible hydrogels and cells in an attempt to provide physiological conditions of native tissues. Cell-laden ECM hydrogels were successfully developed for 3D printing and co-printed with polycaprolactone to develop functional cartilage, heart and adipose tissue [225]. In a recent study, 3D printing of bone dECM on porous scaffolds was found to promote bone regeneration and improve osteoblast adhesion and proliferation [226,227].

Another strategy to improve bioinks for bone printing would be the use of mineralized collagen. Based on the understanding of natural mineralized collagen and its formation process, many studies developed bio-inspired materials mimicking natural mineralized collagen [228,229]. Several protocols have been developed to synthesized an HA and collagen composite [230]. Interestingly, some of those methods are very similar to the one used in Chapter 2 to form CDHA. It consists of precipitating calcium phosphate directly around collagen fibrils, by gradually adding calcium and phosphate to a collagen-fibril-containing medium at an elevated pH value [231]. Cui *et al.* designed and prepared bio-inspired mineralized collagen nano-fibrils that was similar to the natural bone in terms of both the composition and the nanostructure: the mineralized collagen fibrils aligned parallel to each other to form mineralized collagen fibers [232]. The bone remodeling ability of mineralized collagen was evaluated in both a segmental defect rabbit model (long bone) [233] and a sheep cranial defect [234]. In both cases, the results showed that the bio-inspired mineralized collagen repaired the critical defect.

The use of this bio-inspired material is limited, and to the best of my knowledge has yet to be adapted to 3D printing.

Appendix 1: A brief summary of bone biology.

Bone is an organ composed of bone tissue, bone marrow, epithelium, blood vessels, and nerves. Its mechanical function is the most widely recognized and studied, but bones also played a major role in hematopoiesis and mineral, phosphate and glucose homeostasis [4]. On the macroscopic scale, bone is made of dense cortical bone forming an outside shell and cancellous bone within the marrow cavity. The more porous trabecular bone, found in the metaphysis of bones, presents a large surface area and is responsible for the long term control of calcium and phosphate balance. The dense cortical bone, mostly found in the diaphysis of bones, comprises most of the bone mass and takes on most of the role for load bearing and protection [235].

Bone multiscale organization

To achieve those fundamental functions, bones are organized in a hierarchical manner. On the microscale level, cortical bone is composed of many Haversian systems or osteons that are the product of bone resorption and replacement [236]. Those osteons are composed of a central canal, the Haversian canal, carrying the blood vessels, surrounded by layers of concentric lamellae. Bone cells are arranged in several circular layers around the vascular canal. Mature osteons are between 100 and 250µm diameters, corresponding to 20 to 25 lamellae, and measure from 1 to 10mm in length. On the nanoscale level, lamellae are composed of collagen fibers with plates of mineral interspersed within and between the collagen fibrils. The collagen fibrils are composed

of molecules forming a triple helix composed of two α1 chains and a single α2 chain [237].

Figure 20: Bone multiscale organization. *Cortical bone is made of an assembly of modular structures called osteons. Which is also a geometrically efficient system for supplying blood.*

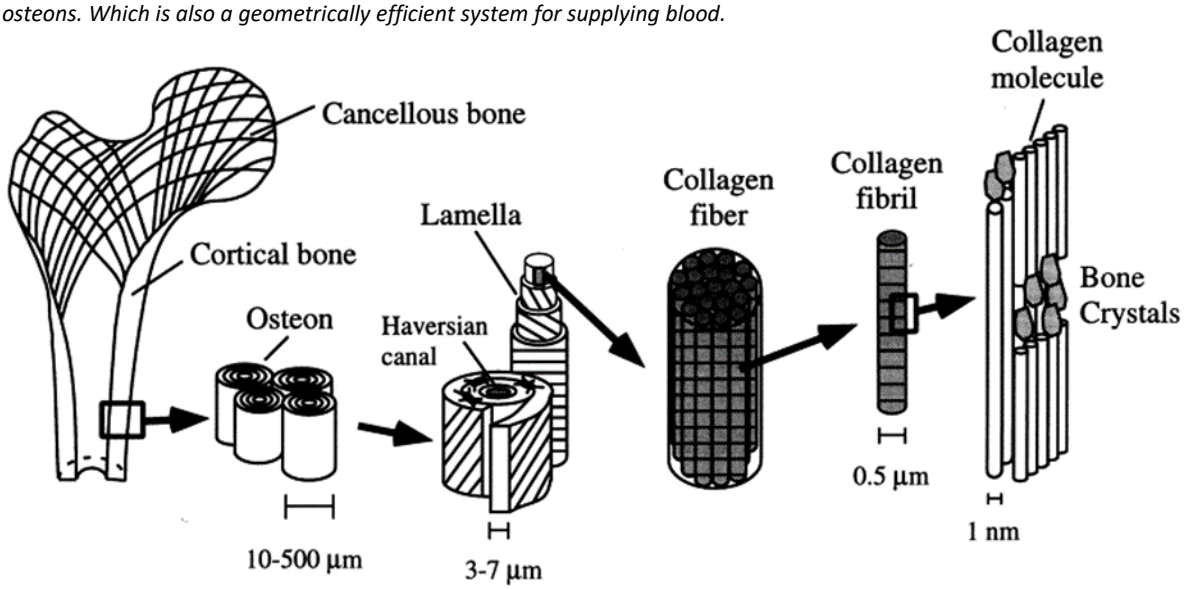

Bone tissue composition

Bones are composed of 65 % by weight of minerals, primarily carbonated apatite and 20-25% of organic components. The remainder 10% is composed of water that is bound to the collagen-mineral composite. The organic phase in made of 90% type I collagen. The remaining 10% is made up of non-collagenous proteins (NCPs) which play a vital role in regulating collagen formation and fibril size, mineralization, and cell attachment [238]. Among NCPs, the most notables are proteoglycans, glycoproteins, such as alkaline phosphatase (ALP), osteopontin, osteocalcin (OCN), fibronectin and osteonectin. ALP is used as a biomarker for bone formation as it hydrolyzes pyrophosphates in bone, allowing normal crystal growth and mineralization. Osteopontin is secreted in the early stages of osteogenesis, inhibiting the mineral formation and crystal growth. Osteocalcin enhances calcium binding and control mineral deposition.

The mineral phase is initially deposited as an amorphous of calcium phosphate. Bone mineral starts to nucleate into the holes and pores present in the collagen fibrils and is catalyzed by the presence of phosphated esters groups and carboxylate groups present in the collagen fibrils. Thereafter, as bone tissue mature the carbonate content is reduced and mineral crystals grow, becoming more plate-like, and eventually interconnecting all of the collagen fibrils. Mineral crystals in bone are on average 20-50 nm long, 15 nm wide and 2-5 nm thick.

During mineralization, minerals rapidly deposited within the collagen framework, achieving 65-70% of its total mineralization within about 3 weeks after initial deposition of collagen. As a major component of bone, hydroxyapatite may possess certain biochemical moieties capable of interacting with cell surface proteins.

Bone cells

Four types of cells are found within the bone matrix: osteoclasts, osteoblasts, lining cells and osteocytes. Osteoclasts function as bone resorbing cells. Osteoblasts are the cells responsible for bone formation, carrying out the function of bone matrix proteins secretion and bone mineralization. Once the bone matrix completed, some mature osteoblasts remain entrapped in bone as osteocytes, and some flatten to cover the quiescent bone surface as bone lining cells [239].

Osteoblasts originate from mesenchymal progenitors, found mostly in the bone marrow. The commitment of mesenchymal stem cells to the osteoblastic lineage starts by their differentiation into osteoprogenitor cells and depends on specific activation of transcription factors induced by morphogenetic and development proteins [240]. At this stage bone, morphogenic protein 2 (BMP2) and Wnt signaling are up-regulated [241].

Osteoprogenitor cells then transition into pre-osteoblast cells, corresponding to an up-regulation of alkaline phosphatase (ALP) and runt-related transcription factor 2 (Runx2) [242]. Finally, pre-osteoblast cells mature into osteoblasts. Runx2 and osterix both up-regulated at this stage, are essential for establishing the osteoblasts phenotype by regulating the expression of a gene that controls bone formation and remodeling (osteocalcin, osteopontin, MMP13) [242,243]. The runx2 signaling pathway is activated by Wnts and BMP2 [244]. ALP is often used as a biomarker of osteogenic differentiation: ALP is expressed early in development, where it is observed on the cell surface and in matrix vesicles. While later during the differentiation of MSCs into osteoblasts, other genes such as osteocalcin are upregulated and ALP expression declines. ALP is among the first functional genes expressed in the process of calcification. It is therefore likely that at least one of its roles in the mineralization process occurs at an early step [245].

Bone blood supply

In calcified tissues, cells must be within 250μm of their blood supply, as nutrients cannot diffuse rapidly through the dense mineralized tissue. The circular arrangement of cells in osteons around a central Haversian canal provides a geometrically efficient system for supplying the maximum amount of bone tissue, from the minimum number of vessels [246]. Vessels in bones have the structural characteristics of capillaries: their walls contain no smooth muscle cells, and they are lined by an incomplete layer of endothelial cells [247].

Bibliography

1. Giannoudis, P. V, Dinopoulos, H. & Tsiridis, E. Bone substitutes: an update. *Injury* **36 Suppl 3**, S20-7 (2005).
2. Van Heest, A., Swiontkowski, M., Leinberry, C., Cohen, M. & Jupiter, J. Bone-graft substitutes. *Lancet* **353**, S28–S29 (1999).
3. Henkel, J., Woodruff, M. A., Epari, D. R., Steck, R., Glatt, V., Dickinson, I. C., Choong, P. F. M., Schuetz, M. A. & Hutmacher, D. W. Bone Regeneration Based on Tissue Engineering Conceptions - A 21st Century Perspective. *Bone Res.* **1**, 216–48 (2013).
4. DiGirolamo, D. J., Clemens, T. L. & Kousteni, S. The skeleton as an endocrine organ. *Nat. Rev. Rheumatol.* **8**, 674–683 (2012).
5. Rubin, J., Rubin, C. & Jacobs, C. R. Molecular pathways mediating mechanical signaling in bone. *Gene* **367**, 1–16 (2006).
6. Weiner, S. & Wagner, H. D. The material bone: Structure-mechanical function relations. *Annu. Rev. Mater. Sci.* **28**, 271–298 (1998).
7. LeGeros, R. Z. Calcium Phosphate-Based Osteoinductive Materials. *Chem. Rev.* **108**, 4742–4753 (2008).
8. Bourne, G. H., and G. M. H. The organic matrix of bone. in *The biochemistry and physiology of bone.* 127–89 (Academic Press, NYC, 1972).
9. Pittenger, M. F. Multilineage Potential of Adult Human Mesenchymal Stem Cells. *Science (80-.).* **284**, 143–147 (1999).
10. Damien, C. J. & Parsons, J. R. Bone graft and bone graft substitutes: a review of current technology and applications. *J. Appl. Biomater.* **2**, 187–208 (1991).
11. Yaszemski, M. J., Payne, R. G., Hayes, W. C., Langer, R. & Mikos, A. G. Evolution of bone transplantation: molecular, cellular and tissue strategies to engineer human bone. *Biomaterials* **17**, 175–85 (1996).
12. Younger, E. M. & Chapman, M. W. Morbidity at bone graft donor sites. *J. Orthop. Trauma* **3**, 192–5 (1989).
13. St John, T. A., Vaccaro, A. R., Sah, A. P., Schaefer, M., Berta, S. C., Albert, T. & Hilibrand, A. Physical and monetary costs associated with autogenous bone graft harvesting. *Am. J. Orthop. (Belle Mead. NJ).* **32**, 18–23 (2003).
14. Zimmermann, G., Moghaddam, A., Group, A.-B. T. P. F. S. & al., et. Allograft bone matrix versus synthetic bone graft substitutes. *Injury* **42 Suppl 2**, S16-21 (2011).
15. Arrington, E. D., Smith, W. J., Chambers, H. G., Bucknell, A. L. & Davino, N. A. Complications of iliac crest bone graft harvesting. *Clin. Orthop. Relat. Res.* 300–9 (1996).
16. Salgado, A. J., Coutinho, O. P. & Reis, R. L. Bone Tissue Engineering: State of the Art and Future Trends. *Macromol. Biosci.* **4**, 743–765 (2004).
17. Burg, K. J., Porter, S. & Kellam, J. F. Biomaterial developments for bone tissue engineering. *Biomaterials* **21**, 2347–59 (2000).
18. Mistry, A. S. & Mikos, A. G. Tissue Engineering Strategies for Bone Regeneration. in 1–22 (Springer Berlin Heidelberg, 2005). doi:10.1007/b99997
19. O'Keefe, R. J. & Mao, J. Bone tissue engineering and regeneration: from

discovery to the clinic--an overview. *Tissue Eng. Part B. Rev.* **17**, 389–92 (2011).
20. Amini, A. R., Laurencin, C. T. & Nukavarapu, S. P. Bone tissue engineering: recent advances and challenges. *Crit. Rev. Biomed. Eng.* **40**, 363–408 (2012).
21. Towler, D. A. The osteogenic-angiogenic interface: Novel insights into the biology of bone formation and fracture repair. *Curr. Osteoporos. Rep.* **6**, 67–71 (2008).
22. Fiedler, T., Belova, I. V., Murch, G. E., Poologasundarampillai, G., Jones, J. R., Roether, J. A. & Boccaccini, A. R. A comparative study of oxygen diffusion in tissue engineering scaffolds. *J. Mater. Sci. Mater. Med.* **25**, 2573–2578 (2014).
23. Huang, Y.-C., Kaigler, D., Rice, K. G., Krebsbach, P. H. & Mooney, D. J. Combined Angiogenic and Osteogenic Factor Delivery Enhances Bone Marrow Stromal Cell-Driven Bone Regeneration. *J. Bone Miner. Res.* **20**, 848–857 (2004).
24. Radisic, M., Malda, J., Epping, E., Geng, W., Langer, R. & Vunjak-Novakovic, G. Oxygen gradients correlate with cell density and cell viability in engineered cardiac tissue. *Biotechnol. Bioeng.* **93**, 332–343 (2006).
25. Ball, O., Nguyen, B.-N. B., Placone, J. K. & Fisher, J. P. 3D Printed Vascular Networks Enhance Viability in High-Volume Perfusion Bioreactor. *Ann. Biomed. Eng.* **44**, 3435–3445 (2016).
26. Nguyen, B.-N. B., Moriarty, R. A., Kamalitdinov, T., Etheridge, J. M. & Fisher, J. P. Collagen hydrogel scaffold promotes mesenchymal stem cell and endothelial cell coculture for bone tissue engineering. *J. Biomed. Mater. Res. Part A* **105**, 1123–1131 (2017).
27. Egaña, J. T., Fierro, F. A., Krüger, S., Bornhäuser, M., Huss, R., Lavandero, S. & Machens, H.-G. Use of Human Mesenchymal Cells to Improve Vascularization in a Mouse Model for Scaffold-Based Dermal Regeneration. *Tissue Eng. Part A* **15**, 1191–1200 (2009).
28. Kneser, U., Polykandriotis, E., Ohnolz, J., Heidner, K., Grabinger, L., Euler, S., Amann, K. U., Hess, A., Brune, K., Greil, P., Stu¨ Rzl, M. & Horch, R. E. Engineering of Vascularized Transplantable Bone Tissues: Induction of Axial Vascularization in an Osteoconductive Matrix Using an Arteriovenous Loop. *Tissue Eng.* **12**, 1721–1731 (2006).
29. Lieberman, J. R., Daluiski, A. & Einhorn, T. A. *The Role of Growth Factors in the Repair of Bone BIOLOGY AND CLINICAL APPLICATIONS*. (2002).
30. Nguyen, B.-N. B., Moriarty, R. A., Kamalitdinov, T., Etheridge, J. M. & Fisher, J. P. Collagen hydrogel scaffold promotes mesenchymal stem cell and endothelial cell coculture for bone tissue engineering. *J. Biomed. Mater. Res. Part A* **105**, 1123–1131 (2017).
31. Dahlin, R. L., Gershovich, J. G., Kasper, F. K. & Mikos, A. G. Flow Perfusion Co-culture of Human Mesenchymal Stem Cells and Endothelial Cells on Biodegradable Polymer Scaffolds. *Ann. Biomed. Eng.* **42**, 1381–1390 (2014).
32. Ma, J., van den Beucken, J. J. J. P., Yang, F., Both, S. K., Cui, F.-Z., Pan, J. & Jansen, J. A. Coculture of Osteoblasts and Endothelial Cells: Optimization of Culture Medium and Cell Ratio. *Tissue Eng. Part C Methods* **17**, 349–357

(2011).
33. Yu, Y., Mu, J., Fan, Z., Lei, G., Yan, M., Wang, S., Tang, C., Wang, Z., Yu, J. & Zhang, G. Insulin-like growth factor 1 enhances the proliferation and osteogenic differentiation of human periodontal ligament stem cells via ERK and JNK MAPK pathways. *Histochem. Cell Biol.* **137**, 513–525 (2012).
34. Huang, Z., Ren, P.-G., Ma, T., Smith, R. L. & Goodman, S. B. Modulating osteogenesis of mesenchymal stem cells by modifying growth factor availability. *Cytokine* **51**, 305–10 (2010).
35. Martín-Saavedra, F., Crespo, L., Escudero-Duch, C., Saldaña, L., Gómez-Barrena, E. & Vilaboa, N. Substrate Microarchitecture Shapes the Paracrine Crosstalk of Stem Cells with Endothelial Cells and Osteoblasts. *Sci. Rep.* **7**, 15182 (2017).
36. Kasper, G., Dankert, N., Tuischer, J., Hoeft, M., Gaber, T., Glaeser, J. D., Zander, D., Tschirschmann, M., Thompson, M., Matziolis, G. & Duda, G. N. Mesenchymal Stem Cells Regulate Angiogenesis According to Their Mechanical Environment. *Stem Cells* **25**, 903–910 (2007).
37. Seib, F. P., Prewitz, M., Werner, C. & Bornhäuser, M. Matrix elasticity regulates the secretory profile of human bone marrow-derived multipotent mesenchymal stromal cells (MSCs). *Biochem. Biophys. Res. Commun.* **389**, 663–667 (2009).
38. Novosel, E. C., Kleinhans, C. & Kluger, P. J. Vascularization is the key challenge in tissue engineering. *Adv. Drug Deliv. Rev.* **63**, 300–311 (2011).
39. Ferrara, N. & Gerber, H. P. The role of vascular endothelial growth factor in angiogenesis. *Acta Haematol.* **106**, 148–56 (2001).
40. Iruela-Arispe, M. L. & Dvorak, H. F. Angiogenesis: a dynamic balance of stimulators and inhibitors. *Thromb. Haemost.* **78**, 672–7 (1997).
41. SILVA, E. A. & MOONEY, D. J. Spatiotemporal control of vascular endothelial growth factor delivery from injectable hydrogels enhances angiogenesis. *J. Thromb. Haemost.* **5**, 590–598 (2007).
42. Marui, A., Kanematsu, A., Yamahara, K., Doi, K., Kushibiki, T., Yamamoto, M., Itoh, H., Ikeda, T., Tabata, Y. & Komeda, M. Simultaneous application of basic fibroblast growth factor and hepatocyte growth factor to enhance the blood vessels formation. *J. Vasc. Surg.* **41**, 82–90 (2005).
43. Epstein, N. E. Complications due to the use of BMP/INFUSE in spine surgery: The evidence continues to mount. *Surg. Neurol. Int.* **4**, S343-52 (2013).
44. Richardson, T. P., Peters, M. C., Ennett, A. B. & Mooney, D. J. Polymeric system for dual growth factor delivery. *Nat. Biotechnol.* **19**, 1029–1034 (2001).
45. Chen, R. R. & Mooney, D. J. Polymeric growth factor delivery strategies for tissue engineering. *Pharm. Res.* **20**, 1103–12 (2003).
46. Kirby, G. T. S., White, L. J., Steck, R., Berner, A., Bogoevski, K., Qutachi, O., Jones, B., Saifzadeh, S., Hutmacher, D. W., Shakesheff, K. M. & Woodruff, M. A. Microparticles for Sustained Growth Factor Delivery in the Regeneration of Critically-Sized Segmental Tibial Bone Defects. *Mater. (Basel, Switzerland)* **9**, (2016).
47. Quinlan, E., López-Noriega, A., Thompson, E. M., Hibbitts, A., Cryan, S. A. & O'Brien, F. J. Controlled release of vascular endothelial growth factor from

spray-dried alginate microparticles in collagen-hydroxyapatite scaffolds for promoting vascularization and bone repair. *J. Tissue Eng. Regen. Med.* **11**, 1097–1109 (2017).
48. Bose, S., Tarafder, S., Edgington, J. & Bandyopadhyay, A. *Overview Biomaterials for regenerative medicine Calcium phosphate Ceramics in drug delivery*. *JOM* **63**,
49. de Groot, K. *Bioceramics of Calcium Phosphate*. (CRC Press, 2018). doi:10.1201/9781351070133
50. Rey, C. Calcium phosphate biomaterials and bone mineral. Differences in composition, structures and properties. *Biomaterials* **11**, 13–5 (1990).
51. Bandyopadhyay, A., Bernard, S., Xue, W. & Bose, S. Calcium Phosphate-Based Resorbable Ceramics: Influence of MgO, ZnO, and SiO2 Dopants. *J. Am. Ceram. Soc.* **89**, 2675–2688 (2006).
52. Doonan, S. Chromatography on Hydroxyapatite. in *Protein Purification Protocols* 191–194 (Humana Press). doi:10.1385/1-59259-655-X:191
53. Dubok, V. A. Bioceramics — Yesterday, Today, Tomorrow. *Powder Metall. Met. Ceram.* **39**, 381–394 (2000).
54. Feng, D., Shi, J., Wang, X., Zhang, L. & Cao, S. Hollow hybrid hydroxyapatite microparticles with sustained and pH-responsive drug delivery properties. *RSC Adv* **3**, 24975–24985 (2013).
55. Wang, K., Wang, Y., Zhao, X., Li, Y., Yang, T., Zhang, X. & Wu, X. Sustained release of simvastatin from hollow carbonated hydroxyapatite microspheres prepared by aspartic acid and sodium dodecyl sulfate. *Mater. Sci. Eng. C* **75**, 565–571 (2017).
56. Liang, C.-C., Park, A. Y. & Guan, J.-L. In vitro scratch assay: a convenient and inexpensive method for analysis of cell migration in vitro. *Nat. Protoc.* **2**, 329–333 (2007).
57. Patel, D. B., Gray, K. M., Santharam, Y., Lamichhane, T. N., Stroka, K. M. & Jay, S. M. Impact of cell culture parameters on production and vascularization bioactivity of mesenchymal stem cell-derived extracellular vesicles. *Bioeng. Transl. Med.* **2**, 170–179 (2017).
58. Hongbo B. Lu, †, Charles T. Campbell, ‡, Daniel J. Graham, † and & Buddy D. Ratner†, §. Surface Characterization of Hydroxyapatite and Related Calcium Phosphates by XPS and TOF-SIMS. (2000). doi:10.1021/AC990812H
59. Mavropoulos, E., Rossi, A. M., da Rocha, N. C. C., Soares, G. A., Moreira, J. C. & Moure, G. T. Dissolution of calcium-deficient hydroxyapatite synthesized at different conditions. *Mater. Charact.* **50**, 203–207 (2003).
60. Lin, J. H. C., Kuo, K. H., Ding, S. J. & Ju, C. P. Surface reaction of stoichiometric and calcium-deficient hydroxyapatite in simulated body fluid. *J. Mater. Sci. Mater. Med.* **12**, 731–741 (2001).
61. Barrère, F., van Blitterswijk, C. A. & de Groot, K. Bone regeneration: molecular and cellular interactions with calcium phosphate ceramics. *Int. J. Nanomedicine* **1**, 317–32 (2006).
62. CHOU, Y., HUANG, W., DUNN, J., MILLER, T. & WU, B. The effect of biomimetic apatite structure on osteoblast viability, proliferation, and gene

expression. *Biomaterials* **26**, 285–295 (2005).
63. Suzuki, O., Kamakura, S., Katagiri, T., Nakamura, M., Zhao, B., Honda, Y. & Kamijo, R. Bone formation enhanced by implanted octacalcium phosphate involving conversion into Ca-deficient hydroxyapatite. *Biomaterials* **27**, 2671–2681 (2006).
64. Dorozhkin, S. V. A review on the dissolution models of calcium apatites. *Prog. Cryst. Growth Charact. Mater.* **44**, 45–61 (2002).
65. Oryan, A., Kamali, A., Moshiri, A. & Baghaban Eslaminejad, M. Role of Mesenchymal Stem Cells in Bone Regenerative Medicine: What Is the Evidence? *Cells Tissues Organs* **204**, 59–83 (2017).
66. Strehl, R., Schumacher, K. & Minuth, W. W. *Proliferating Cells versus Differentiated Cells in Tissue Engineering*. *TISSUE ENGINEERING* **8**, (2002).
67. Ruijtenberg, S. & van den Heuvel, S. Coordinating cell proliferation and differentiation: Antagonism between cell cycle regulators and cell type-specific gene expression. *Cell Cycle* **15**, 196–212 (2016).
68. Shum, L. C., White, N. S., Mills, B. N., Bentley, K. L. de M. & Eliseev, R. A. Energy Metabolism in Mesenchymal Stem Cells During Osteogenic Differentiation. *Stem Cells Dev.* **25**, 114–22 (2016).
69. Aubin, J. E. Bone stem cells. *J. Cell. Biochem. Suppl.* **30**–**31**, 73–82 (1998).
70. Langer, R. & Vacanti, J. P. Tissue engineering. *Science* **260**, 920–6 (1993).
71. Cancedda, R., Giannoni, P. & Mastrogiacomo, M. A tissue engineering approach to bone repair in large animal models and in clinical practice. *Biomaterials* **28**, 4240–50 (2007).
72. Santos, M. I. & Reis, R. L. Vascularization in bone tissue engineering: physiology, current strategies, major hurdles and future challenges. *Macromol. Biosci.* **10**, 12–27 (2010).
73. Quarto, R., Mastrogiacomo, M., Cancedda, R., Kutepov, S. M., Mukhachev, V., Lavroukov, A., Kon, E. & Marcacci, M. Repair of large bone defects with the use of autologous bone marrow stromal cells. *N. Engl. J. Med.* **344**, 385–6 (2001).
74. Schimming, R. & Schmelzeisen, R. Tissue-engineered bone for maxillary sinus augmentation. *J. Oral Maxillofac. Surg.* **62**, 724–9 (2004).
75. Bruder, S. P., Kraus, K. H., Goldberg, V. M. & Kadiyala, S. The effect of implants loaded with autologous mesenchymal stem cells on the healing of canine segmental bone defects. *J. Bone Joint Surg. Am.* **80**, 985–96 (1998).
76. Puelacher, W. C., Vacanti, J. P., Ferraro, N. F., Schloo, B. & Vacanti, C. A. Femoral shaft reconstruction using tissue-engineered growth of bone. *Int. J. Oral Maxillofac. Surg.* **25**, 223–8 (1996).
77. Shang, Q., Wang, Z., Liu, W., Shi, Y., Cui, L. & Cao, Y. Tissue-engineered bone repair of sheep cranial defects with autologous bone marrow stromal cells. *J. Craniofac. Surg.* **12**, 586-93; discussion 594–5 (2001).
78. Schliephake, H., Knebel, J. W., Aufderheide, M. & Tauscher, M. Use of cultivated osteoprogenitor cells to increase bone formation in segmental mandibular defects: an experimental pilot study in sheep. *Int. J. Oral Maxillofac. Surg.* **30**, 531–7 (2001).
79. Karageorgiou, V. & Kaplan, D. Porosity of 3D biomaterial scaffolds and

osteogenesis. *Biomaterials* **26**, 5474–91 (2005).
80. Jones, A. C., Arns, C. H., Sheppard, A. P., Hutmacher, D. W., Milthorpe, B. K. & Knackstedt, M. A. Assessment of bone ingrowth into porous biomaterials using MICRO-CT. *Biomaterials* **28**, 2491–504 (2007).
81. Otsuki, B., Takemoto, M., Fujibayashi, S., Neo, M., Kokubo, T. & Nakamura, T. Pore throat size and connectivity determine bone and tissue ingrowth into porous implants: three-dimensional micro-CT based structural analyses of porous bioactive titanium implants. *Biomaterials* **27**, 5892–900 (2006).
82. Cao, H. & Kuboyama, N. A biodegradable porous composite scaffold of PGA/beta-TCP for bone tissue engineering. *Bone* **46**, 386–95 (2010).
83. Kucharska, M., Butruk, B., Walenko, K., Brynk, T. & Ciach, T. Fabrication of in-situ foamed chitosan/β-TCP scaffolds for bone tissue engineering application. *Mater. Lett.* **85**, 124–127 (2012).
84. Sultana, N. & Wang, M. Fabrication of HA/PHBV composite scaffolds through the emulsion freezing/freeze-drying process and characterisation of the scaffolds. *J. Mater. Sci. Mater. Med.* **19**, 2555–2561 (2007).
85. Hutmacher, D. W. Scaffolds in tissue engineering bone and cartilage. *Biomaterials* **21**, 2529–2543 (2000).
86. Bose, S., Vahabzadeh, S. & Bandyopadhyay, A. Bone tissue engineering using 3D printing. *Mater. Today* **16**, 496–504 (2013).
87. Murphy, S. V & Atala, A. 3D bioprinting of tissues and organs. *Nat. Biotechnol.* **32**, 773–85 (2014).
88. Gao, G., Schilling, A. F., Hubbell, K., Yonezawa, T., Truong, D., Hong, Y., Dai, G. & Cui, X. Improved properties of bone and cartilage tissue from 3D inkjet-bioprinted human mesenchymal stem cells by simultaneous deposition and photocrosslinking in PEG-GelMA. *Biotechnol. Lett.* (2015). doi:10.1007/s10529-015-1921-2
89. Poldervaart, M. T., Wang, H., van der Stok, J., Weinans, H., Leeuwenburgh, S. C. G., Öner, F. C., Dhert, W. J. A. & Alblas, J. Sustained release of BMP-2 in bioprinted alginate for osteogenicity in mice and rats. *PLoS One* **8**, e72610 (2013).
90. Fedorovich, N. E., Kuipers, E., Gawlitta, D., Dhert, W. J. A. & Alblas, J. Scaffold porosity and oxygenation of printed hydrogel constructs affect functionality of embedded osteogenic progenitors. *Tissue Eng. Part A* **17**, 2473–86 (2011).
91. Wang, X., Tolba, E., Schröder, H. C., Neufurth, M., Feng, Q., Diehl-Seifert, B. & Müller, W. E. G. Effect of bioglass on growth and biomineralization of SaOS-2 cells in hydrogel after 3D cell bioprinting. *PLoS One* **9**, e112497 (2014).
92. Levato, R., Visser, J., Planell, J. A., Engel, E., Malda, J. & Mateos-Timoneda, M. A. Biofabrication of tissue constructs by 3D bioprinting of cell-laden microcarriers. *Biofabrication* **6**, 035020 (2014).
93. Schütz, K., Placht, A.-M., Paul, B., Brüggemeier, S., Gelinsky, M. & Lode, A. Three-dimensional plotting of a cell-laden alginate/methylcellulose blend: towards biofabrication of tissue engineering constructs with clinically relevant dimensions. *J. Tissue Eng. Regen. Med.* (2015). doi:10.1002/term.2058

94. Wüst, S., Godla, M. E., Müller, R. & Hofmann, S. Tunable hydrogel composite with two-step processing in combination with innovative hardware upgrade for cell-based three-dimensional bioprinting. *Acta Biomater.* **10**, 630–40 (2014).
95. Sawkins, M. J., Mistry, P., Brown, B. N., Shakesheff, K. M., Bonassar, L. J. & Yang, J. Cell and protein compatible 3D bioprinting of mechanically strong constructs for bone repair. *Biofabrication* **7**, 035004 (2015).
96. Martínez-Vázquez, F. J., Cabañas, M. V, Paris, J. L., Lozano, D. & Vallet-Regí, M. Fabrication of novel Si-doped hydroxyapatite/gelatine scaffolds by rapid prototyping for drug delivery and bone regeneration. *Acta Biomater.* **15**, 200–9 (2015).
97. Gonçalves, E. M., Oliveira, F. J., Silva, R. F., Neto, M. A., Fernandes, M. H., Amaral, M., Vallet-Regí, M. & Vila, M. Three-dimensional printed PCL-hydroxyapatite scaffolds filled with CNTs for bone cell growth stimulation. *J. Biomed. Mater. Res. B. Appl. Biomater.* (2015). doi:10.1002/jbm.b.33432
98. Zigang Ge, Lishan Wang, Boon Chin Heng, Tian, X.-F., Kai Lu, Tai Weng Fan, V., Jin Fei Yeo, Tong Cao & Tan, E. Proliferation and differentiation of human osteoblasts within 3D printed poly-lactic-co-glycolic acid scaffolds. *J. Biomater. Appl.* **23**, 533–47 (2009).
99. Kruyt, M., De Bruijn, J., Rouwkema, J., Van Bliterswijk, C., Oner, C., Verbout, A. & Dhert, W. Analysis of the dynamics of bone formation, effect of cell seeding density, and potential of allogeneic cells in cell-based bone tissue engineering in goats. *Tissue Eng. Part A* **14**, 1081–8 (2008).
100. Kruyt, M. C., de Bruijn, J. D., Wilson, C. E., Oner, F. C., van Blitterswijk, C. A., Verbout, A. J. & Dhert, W. J. A. Viable osteogenic cells are obligatory for tissue-engineered ectopic bone formation in goats. *Tissue Eng.* **9**, 327–36 (2003).
101. Nair, K., Gandhi, M., Khalil, S., Yan, K. C., Marcolongo, M., Barbee, K. & Sun, W. Characterization of cell viability during bioprinting processes. *Biotechnol. J.* **4**, 1168–77 (2009).
102. Chang, R., Nam, J. & Sun, W. Effects of dispensing pressure and nozzle diameter on cell survival from solid freeform fabrication-based direct cell writing. *Tissue Eng. Part A* **14**, 41–8 (2008).
103. Lutolf, M. P. & Hubbell, J. A. Synthetic biomaterials as instructive extracellular microenvironments for morphogenesis in tissue engineering. *Nat. Biotechnol.* **23**, 47–55 (2005).
104. Drury, J. L. & Mooney, D. J. Hydrogels for tissue engineering: scaffold design variables and applications. *Biomaterials* **24**, 4337–4351 (2003).
105. Slaughter, B. V, Khurshid, S. S., Fisher, O. Z., Khademhosseini, A. & Peppas, N. A. Hydrogels in regenerative medicine. *Adv. Mater.* **21**, 3307–29 (2009).
106. Bokhari, M. A., Akay, G., Zhang, S. & Birch, M. A. The enhancement of osteoblast growth and differentiation in vitro on a peptide hydrogel-polyHIPE polymer hybrid material. *Biomaterials* **26**, 5198–208 (2005).
107. Abbott, A. Cell culture: biology's new dimension. *Nature* **424**, 870–2 (2003).
108. Fedorovich, N. E., Schuurman, W., Wijnberg, H. M., Prins, H.-J., van Weeren, P. R., Malda, J., Alblas, J. & Dhert, W. J. A. Biofabrication of osteochondral tissue equivalents by printing topologically defined, cell-laden hydrogel

scaffolds. *Tissue Eng. Part C. Methods* **18**, 33–44 (2012).
109. Ahn, S., Lee, H., Bonassar, L. J. & Kim, G. Cells (MC3T3-E1)-laden alginate scaffolds fabricated by a modified solid-freeform fabrication process supplemented with an aerosol spraying. *Biomacromolecules* **13**, 2997–3003 (2012).
110. Cohen, D. L., Malone, E., Lipson, H. & Bonassar, L. J. Direct freeform fabrication of seeded hydrogels in arbitrary geometries. *Tissue Eng.* **12**, 1325–35 (2006).
111. Gasperini, L., Mano, J. F. & Reis, R. L. Natural polymers for the microencapsulation of cells. *J. R. Soc. Interface* **11**, 20140817 (2014).
112. Fedorovich, N. E., Alblas, J., de Wijn, J. R., Hennink, W. E., Verbout, A. J. & Dhert, W. J. A. Hydrogels as extracellular matrices for skeletal tissue engineering: state-of-the-art and novel application in organ printing. *Tissue Eng.* **13**, 1905–25 (2007).
113. Stevens, M. M., Marini, R. P., Schaefer, D., Aronson, J., Langer, R. & Shastri, V. P. In vivo engineering of organs: the bone bioreactor. *Proc. Natl. Acad. Sci. U. S. A.* **102**, 11450–5 (2005).
114. Augst, A. D., Kong, H. J. & Mooney, D. J. Alginate hydrogels as biomaterials. *Macromol. Biosci.* **6**, 623–33 (2006).
115. Wang, L., Shelton, R. M., Cooper, P. R., Lawson, M., Triffitt, J. T. & Barralet, J. E. Evaluation of sodium alginate for bone marrow cell tissue engineering. *Biomaterials* **24**, 3475–81 (2003).
116. Atala, A. & Yoo, J. J. *Essentials of 3D Biofabrication and Translation*. (Elsevier Science, 2015).
117. Malda, J., Visser, J., Melchels, F. P., Jüngst, T., Hennink, W. E., Dhert, W. J. A., Groll, J. & Hutmacher, D. W. 25th anniversary article: Engineering hydrogels for biofabrication. *Adv. Mater.* **25**, 5011–28 (2013).
118. Sisson, K., Zhang, C., Farach-Carson, M. C., Chase, D. B. & Rabolt, J. F. Evaluation of cross-linking methods for electrospun gelatin on cell growth and viability. *Biomacromolecules* **10**, 1675–80 (2009).
119. Young, S., Wong, M., Tabata, Y. & Mikos, A. G. Gelatin as a delivery vehicle for the controlled release of bioactive molecules. *J. Control. Release* **109**, 256–74 (2005).
120. Hoch, E., Hirth, T., Tovar, G. E. M. & Borchers, K. Chemical tailoring of gelatin to adjust its chemical and physical properties for functional bioprinting. *J. Mater. Chem. B* **1**, 5675 (2013).
121. Schiele, N. R., Chrisey, D. B. & Corr, D. T. Gelatin-based laser direct-write technique for the precise spatial patterning of cells. *Tissue Eng. Part C. Methods* **17**, 289–98 (2011).
122. Zhang, T., Yan, K. C., Ouyang, L. & Sun, W. Mechanical characterization of bioprinted in vitro soft tissue models. *Biofabrication* **5**, 045010 (2013).
123. Xu, T., Binder, K. W., Albanna, M. Z., Dice, D., Zhao, W., Yoo, J. J. & Atala, A. Hybrid printing of mechanically and biologically improved constructs for cartilage tissue engineering applications. *Biofabrication* **5**, 015001 (2013).
124. Luo, Y., Wu, C., Lode, A. & Gelinsky, M. Hierarchical mesoporous bioactive glass/alginate composite scaffolds fabricated by three-dimensional plotting for

bone tissue engineering. *Biofabrication* **5**, 015005 (2013).
125. Jones, J. R. Review of bioactive glass: from Hench to hybrids. *Acta Biomater.* **9**, 4457–86 (2013).
126. Sart, S., Agathos, S. N. & Li, Y. Engineering stem cell fate with biochemical and biomechanical properties of microcarriers. *Biotechnol. Prog.* **29**, 1354–66
127. Martin, Y., Eldardiri, M., Lawrence-Watt, D. J. & Sharpe, J. R. Microcarriers and their potential in tissue regeneration. *Tissue Eng. Part B. Rev.* **17**, 71–80 (2011).
128. Malda, J. & Frondoza, C. G. Microcarriers in the engineering of cartilage and bone. *Trends Biotechnol.* **24**, 299–304 (2006).
129. Tadic, D. & Epple, M. A thorough physicochemical characterisation of 14 calcium phosphate-based bone substitution materials in comparison to natural bone. *Biomaterials* **25**, 987–94 (2004).
130. Obregon, F., Vaquette, C., Ivanovski, S., Hutmacher, D. W. & Bertassoni, L. E. Three-Dimensional Bioprinting for Regenerative Dentistry and Craniofacial Tissue Engineering. *J. Dent. Res.* (2015). doi:10.1177/0022034515588885
131. Hutmacher, D. W., Sittinger, M. & Risbud, M. V. Scaffold-based tissue engineering: rationale for computer-aided design and solid free-form fabrication systems. *Trends Biotechnol.* **22**, 354–62 (2004).
132. Melchels, F. P. W., Feijen, J. & Grijpma, D. W. A review on stereolithography and its applications in biomedical engineering. *Biomaterials* **31**, 6121–30 (2010).
133. Seyednejad, H., Gawlitta, D., Dhert, W. J. a, Van Nostrum, C. F., Vermonden, T. & Hennink, W. E. Preparation and characterization of a three-dimensional printed scaffold based on a functionalized polyester for bone tissue engineering applications. *Acta Biomater.* **7**, 1999–2006 (2011).
134. Eosoly, S., Brabazon, D., Lohfeld, S. & Looney, L. Selective laser sintering of hydroxyapatite/poly-epsilon-caprolactone scaffolds. *Acta Biomater.* **6**, 2511–7 (2010).
135. Schantz, J.-T., Brandwood, A., Hutmacher, D. W., Khor, H. L. & Bittner, K. Osteogenic differentiation of mesenchymal progenitor cells in computer designed fibrin-polymer-ceramic scaffolds manufactured by fused deposition modeling. *J. Mater. Sci. Mater. Med.* **16**, 807–19 (2005).
136. Gratson, G. M., Xu, M. & Lewis, J. A. Microperiodic structures: direct writing of three-dimensional webs. *Nature* **428**, 386 (2004).
137. Detsch, R., Uhl, F., Deisinger, U. & Ziegler, G. 3D-Cultivation of bone marrow stromal cells on hydroxyapatite scaffolds fabricated by dispense-plotting and negative mould technique. *J. Mater. Sci. Mater. Med.* **19**, 1491–6 (2008).
138. Lode, A., Bernhardt, A. & Gelinsky, M. Cultivation of human bone marrow stromal cells on three-dimensional scaffolds of mineralized collagen: influence of seeding density on colonization, proliferation and osteogenic differentiation. *J. Tissue Eng. Regen. Med.* **2**, 400–7 (2008).
139. Wu, C., Luo, Y., Cuniberti, G., Xiao, Y. & Gelinsky, M. Three-dimensional printing of hierarchical and tough mesoporous bioactive glass scaffolds with a controllable pore architecture, excellent mechanical strength and

mineralization ability. *Acta Biomater.* **7**, 2644–50 (2011).
140. Sobral, J. M., Caridade, S. G., Sousa, R. A., Mano, J. F. & Reis, R. L. Three-dimensional plotted scaffolds with controlled pore size gradients: Effect of scaffold geometry on mechanical performance and cell seeding efficiency. *Acta Biomater.* **7**, 1009–18 (2011).
141. Shor, L., Güçeri, S., Wen, X., Gandhi, M. & Sun, W. Fabrication of three-dimensional polycaprolactone/hydroxyapatite tissue scaffolds and osteoblast-scaffold interactions in vitro. *Biomaterials* **28**, 5291–7 (2007).
142. Mondrinos, M. J., Dembzynski, R., Lu, L., Byrapogu, V. K. C., Wootton, D. M., Lelkes, P. I. & Zhou, J. Porogen-based solid freeform fabrication of polycaprolactone-calcium phosphate scaffolds for tissue engineering. *Biomaterials* **27**, 4399–408 (2006).
143. Heo, S.-J., Kim, S.-E., Wei, J., Hyun, Y.-T., Yun, H.-S., Kim, D.-H., Shin, J. W. & Shin, J.-W. Fabrication and characterization of novel nano- and micro-HA/PCL composite scaffolds using a modified rapid prototyping process. *J. Biomed. Mater. Res. A* **89**, 108–16 (2009).
144. Hollinger, J. O. & Battistone, G. C. Biodegradable bone repair materials. Synthetic polymers and ceramics. *Clin. Orthop. Relat. Res.* 290–305 (1986).
145. Rezwan, K., Chen, Q. Z., Blaker, J. J. & Boccaccini, A. R. Biodegradable and bioactive porous polymer/inorganic composite scaffolds for bone tissue engineering. *Biomaterials* **27**, 3413–31 (2006).
146. Sousa, F. C. G. & Evans, J. R. G. Sintered Hydroxyapatite Latticework for Bone Substitute. *J. Am. Ceram. Soc.* **86**, 517–519 (2003).
147. Tarafder, S., Balla, V. K., Davies, N. M., Bandyopadhyay, A. & Bose, S. Microwave-sintered 3D printed tricalcium phosphate scaffolds for bone tissue engineering. *J. Tissue Eng. Regen. Med.* **7**, 631–41 (2013).
148. Kalita, S. J., Bose, S., Hosick, H. L. & Bandyopadhyay, A. Development of controlled porosity polymer-ceramic composite scaffolds via fused deposition modeling. *Mater. Sci. Eng. C* **23**, 611–620 (2003).
149. Liu, X. & Ma, P. X. Polymeric scaffolds for bone tissue engineering. *Ann. Biomed. Eng.* **32**, 477–86 (2004).
150. Giordano, R. A., Wu, B. M., Borland, S. W., Cima, L. G., Sachs, E. M. & Cima, M. J. Mechanical properties of dense polylactic acid structures fabricated by three dimensional printing. *J. Biomater. Sci. Polym. Ed.* **8**, 63–75 (1996).
151. Suwanprateeb, J., Thammarakcharoen, F., Wongsuvan, V. & Chokevivat, W. Development of porous powder printed high density polyethylene for personalized bone implants. *J. Porous Mater.* **19**, 623–632 (2011).
152. Wang, M. O., Vorwald, C. E., Dreher, M. L., Mott, E. J., Cheng, M.-H., Cinar, A., Mehdizadeh, H., Somo, S., Dean, D., Brey, E. M. & Fisher, J. P. Evaluating 3D-printed biomaterials as scaffolds for vascularized bone tissue engineering. *Adv. Mater.* **27**, 138–44 (2015).
153. Goh, B. T., Teh, L. Y., Tan, D. B. P., Zhang, Z. & Teoh, S. H. Novel 3D polycaprolactone scaffold for ridge preservation--a pilot randomised controlled clinical trial. *Clin. Oral Implants Res.* **26**, 271–7 (2015).
154. Reichert, J. C., Wullschleger, M. E., Cipitria, A., Lienau, J., Cheng, T. K.,

Schütz, M. A., Duda, G. N., Nöth, U., Eulert, J. & Hutmacher, D. W. Custom-made composite scaffolds for segmental defect repair in long bones. *Int. Orthop.* **35**, 1229–36 (2011).
155. Wang, M. O., Piard, C. M., Melchiorri, A., Dreher, M. L. & Fisher, J. P. Evaluating changes in structure and cytotoxicity during in vitro degradation of three-dimensional printed scaffolds. *Tissue Eng. Part A* **21**, 1642–53 (2015).
156. Ghasemi-Mobarakeh, L., Prabhakaran, M. P., Tian, L., Shamirzaei-Jeshvaghani, E., Dehghani, L. & Ramakrishna, S. Structural properties of scaffolds: Crucial parameters towards stem cells differentiation. *World J. Stem Cells* **7**, 728–44 (2015).
157. Lee, J. W., Kang, K. S., Lee, S. H., Kim, J.-Y., Lee, B.-K. & Cho, D.-W. Bone regeneration using a microstereolithography-produced customized poly(propylene fumarate)/diethyl fumarate photopolymer 3D scaffold incorporating BMP-2 loaded PLGA microspheres. *Biomaterials* **32**, 744–52 (2011).
158. Vila, M., Cicuéndez, M., Sánchez-Marcos, J., Fal-Miyar, V., Manzano, M., Prieto, C. & Vallet-Regi, M. Electrical stimuli to increase cell proliferation on carbon nanotubes/mesoporous silica composites for drug delivery. *J. Biomed. Mater. Res. A* **101**, 213–21 (2013).
159. Wang, M., Cheng, X., Zhu, W., Holmes, B., Keidar, M. & Zhang, L. G. Design of biomimetic and bioactive cold plasma-modified nanostructured scaffolds for enhanced osteogenic differentiation of bone marrow-derived mesenchymal stem cells. *Tissue Eng. Part A* **20**, 1060–71 (2014).
160. Liu, X., Feng, Q., Bachhuka, A. & Vasilev, K. Surface modification by allylamine plasma polymerization promotes osteogenic differentiation of human adipose-derived stem cells. *ACS Appl. Mater. Interfaces* **6**, 9733–41 (2014).
161. Chen, G., Zhou, P., Mei, N., Chen, X., Shao, Z., Pan, L. & Wu, C. Silk fibroin modified porous poly(epsilon-caprolactone) scaffold for human fibroblast culture in vitro. *J. Mater. Sci. Mater. Med.* **15**, 671–7 (2004).
162. Kao, C.-T., Lin, C.-C., Chen, Y.-W., Yeh, C.-H., Fang, H.-Y. & Shie, M.-Y. Poly(dopamine) coating of 3D printed poly(lactic acid) scaffolds for bone tissue engineering. *Mater. Sci. Eng. C* **56**, 165–173 (2015).
163. Kuo, Y.-C. & Yeh, C.-F. Effect of surface-modified collagen on the adhesion, biocompatibility and differentiation of bone marrow stromal cells in poly(lactide-co-glycolide)/chitosan scaffolds. *Colloids Surf. B. Biointerfaces* **82**, 624–31 (2011).
164. Volkmer, E., Drosse, I., Otto, S., Stangelmayer, A., Stengele, M., Kallukalam, B. C., Mutschler, W. & Schieker, M. Hypoxia in static and dynamic 3D culture systems for tissue engineering of bone. *Tissue Eng. Part A* **14**, 1331–40 (2008).
165. Yeatts, A. B. & Fisher, J. P. Bone tissue engineering bioreactors: dynamic culture and the influence of shear stress. *Bone* **48**, 171–81 (2011).
166. Yeatts, A. B. & Fisher, J. P. Tubular perfusion system for the long-term dynamic culture of human mesenchymal stem cells. *Tissue Eng. Part C. Methods* **17**, 337–48 (2011).
167. Rowley, J. A., Madlambayan, G. & Mooney, D. J. Alginate hydrogels as

synthetic extracellular matrix materials. *Biomaterials* **20**, 45–53 (1999).
168. Grieb, T. A., Forng, R.-Y., Stafford, R. E., Lin, J., Almeida, J., Bogdansky, S., Ronholdt, C., Drohan, W. N. & Burgess, W. H. Effective use of optimized, high-dose (50 kGy) gamma irradiation for pathogen inactivation of human bone allografts. *Biomaterials* **26**, 2033–42 (2005).
169. Reilly, D. T. & Burstein, A. H. The elastic and ultimate properties of compact bone tissue. *J. Biomech.* **8**, 393–405 (1975).
170. Trachtenberg, J. E., Mountziaris, P. M., Miller, J. S., Wettergreen, M., Kasper, F. K. & Mikos, A. G. Open-source three-dimensional printing of biodegradable polymer scaffolds for tissue engineering. *J. Biomed. Mater. Res. A* **102**, 4326–35 (2014).
171. Habibovic, P., Yuan, H., van der Valk, C. M., Meijer, G., van Blitterswijk, C. A. & de Groot, K. 3D microenvironment as essential element for osteoinduction by biomaterials. *Biomaterials* **26**, 3565–75 (2005).
172. Phillippi, J. A., Miller, E., Weiss, L., Huard, J., Waggoner, A. & Campbell, P. Microenvironments engineered by inkjet bioprinting spatially direct adult stem cells toward muscle- and bone-like subpopulations. *Stem Cells* **26**, 127–34 (2008).
173. Fedorovich, N. E., Wijnberg, H. M., Dhert, W. J. A. & Alblas, J. Distinct tissue formation by heterogeneous printing of osteo- and endothelial progenitor cells. *Tissue Eng. Part A* **17**, 2113–21 (2011).
174. Annabi, N., Tamayol, A., Uquillas, J. A., Akbari, M., Bertassoni, L. E., Cha, C., Camci-Unal, G., Dokmeci, M. R., Peppas, N. A. & Khademhosseini, A. 25th anniversary article: Rational design and applications of hydrogels in regenerative medicine. *Adv. Mater.* **26**, 85–123 (2014).
175. Tertuliano, O. A. & Greer, J. R. The nanocomposite nature of bone drives its strength and damage resistance. *Nat. Mater.* **15**, 1195–1202 (2016).
176. Andric, T., Sampson, A. C. & Freeman, J. W. Fabrication and characterization of electrospun osteon mimicking scaffolds for bone tissue engineering. *Mater. Sci. Eng. C* **31**, 2–8 (2011).
177. Kang, H.-W., Lee, S. J., Ko, I. K., Kengla, C., Yoo, J. J. & Atala, A. A 3D bioprinting system to produce human-scale tissue constructs with structural integrity. *Nat. Biotechnol.* **34**, 312–319 (2016).
178. Chung, E., Rytlewski, J. A., Merchant, A. G., Dhada, K. S., Lewis, E. W. & Suggs, L. J. Fibrin-based 3D matrices induce angiogenic behavior of adipose-derived stem cells. *Acta Biomater.* **17**, 78–88 (2015).
179. Janmey, P. A., Winer, J. P. & Weisel, J. W. Fibrin gels and their clinical and bioengineering applications. *J. R. Soc. Interface* **6**, 1–10 (2009).
180. An, S. S. A. & Rajangam, S. S. A. Fibrinogen and fibrin based micro and nano scaffolds incorporated with drugs, proteins, cells and genes for therapeutic biomedical applications. *Int. J. Nanomedicine* **8**, 3641 (2013).
181. Kneser, U., Voogd, A., Ohnolz, J., Buettner, O., Stangenberg, L., Zhang, Y. H., Stark, G. B. & Schaefer, D. J. Fibrin gel-immobilized primary osteoblasts in calcium phosphate bone cement: in vivo evaluation with regard to application as injectable biological bone substitute. *Cells. Tissues. Organs* **179**, 158–69 (2005).

182. Piard, C. M., Chen, Y. & Fisher, J. P. Cell-Laden 3D Printed Scaffolds for Bone Tissue Engineering. *Clin. Rev. Bone Miner. Metab.* **13**, (2015).
183. Gunatillake, P. A. & Adhikari, R. Biodegradable synthetic polymers for tissue engineering. *Eur. Cell. Mater.* **5**, 1–16; discussion 16 (2003).
184. Roohani-Esfahani, S.-I., Newman, P. & Zreiqat, H. Design and Fabrication of 3D printed Scaffolds with a Mechanical Strength Comparable to Cortical Bone to Repair Large Bone Defects. (2015). doi:10.1038/srep19468
185. KARAGEORGIOU, V. & KAPLAN, D. Porosity of 3D biomaterial scaffolds and osteogenesis. *Biomaterials* **26**, 5474–5491 (2005).
186. Cyster, L. A., Grant, D. M., Howdle, S. M., Rose, F. R. A. J., Irvine, D. J., Freeman, D., Scotchford, C. A. & Shakesheff, K. M. The influence of dispersant concentration on the pore morphology of hydroxyapatite ceramics for bone tissue engineering. *Biomaterials* **26**, 697–702 (2005).
187. Kirkpatrick, C. J., Fuchs, S. & Unger, R. E. Co-culture systems for vascularization — Learning from nature. *Adv. Drug Deliv. Rev.* **63**, 291–299 (2011).
188. Kolbe, M., Xiang, Z., Dohle, E., Tonak, M., Kirkpatrick, C. J. & Fuchs, S. Paracrine Effects Influenced by Cell Culture Medium and Consequences on Microvessel-Like Structures in Cocultures of Mesenchymal Stem Cells and Outgrowth Endothelial Cells. *Tissue Eng. Part A* **17**, 2199–2212 (2011).
189. Gershovich, J. G., Dahlin, R. L., Kasper, F. K. & Mikos, A. G. Enhanced Osteogenesis in Cocultures with Human Mesenchymal Stem Cells and Endothelial Cells on Polymeric Microfiber Scaffolds. *Tissue Eng. Part A* **19**, 2565–2576 (2013).
190. Ern, C., Krump-Konvalinkova, V., Docheva, D., Schindler, S., Rossmann, O., Böcker, W., Mutschler, W. & Schieker, M. Interactions of Human Endothelial and Multipotent Mesenchymal Stem Cells in Cocultures. *Open Biomed. Eng. J.* **4**, 190–198 (2010).
191. Guerrero, J., Catros, S., Derkaoui, S.-M., Lalande, C., Siadous, R., Bareille, R., Thébaud, N., Bordenave, L., Chassande, O., Le Visage, C., Letourneur, D. & Amédée, J. Cell interactions between human progenitor-derived endothelial cells and human mesenchymal stem cells in a three-dimensional macroporous polysaccharide-based scaffold promote osteogenesis. *Acta Biomater.* **9**, 8200–8213 (2013).
192. Su, N., Gao, P.-L., Wang, K., Wang, J.-Y., Zhong, Y. & Luo, Y. Fibrous scaffolds potentiate the paracrine function of mesenchymal stem cells: A new dimension in cell-material interaction. *Biomaterials* **141**, 74–85 (2017).
193. Kusuma, G. D., Carthew, J., Lim, R. & Frith, J. E. Effect of the Microenvironment on Mesenchymal Stem Cell Paracrine Signaling: Opportunities to Engineer the Therapeutic Effect. *Stem Cells Dev.* **26**, 617–631 (2017).
194. Piard, C., Baker, H., Kamalitdinov, T. & Fisher, J. P. Bioprinted osteon-like scaffolds enhance in vivo neovascularization. *Biofabrication* (2019). doi:10.1088/1758-5090/ab078a
195. Lamichhane, T. N., Raiker, R. S. & Jay, S. M. Exogenous DNA Loading into Extracellular Vesicles via Electroporation is Size-Dependent and Enables

Limited Gene Delivery. *Mol. Pharm.* **12**, 3650–3657 (2015).
196. Arnaoutova, I. & Kleinman, H. K. In vitro angiogenesis: endothelial cell tube formation on gelled basement membrane extract. *Nat. Protoc.* **5**, 628–635 (2010).
197. Carpentier, G. ImageJ contribution: Angiogenesis Analyzer. *ImageJ News*
198. Eilken, H. M. & Adams, R. H. Dynamics of endothelial cell behavior in sprouting angiogenesis. *Curr. Opin. Cell Biol.* **22**, 617–625 (2010).
199. Potente, M., Gerhardt, H. & Carmeliet, P. Basic and Therapeutic Aspects of Angiogenesis. *Cell* **146**, 873–887 (2011).
200. Risau, W. Mechanisms of angiogenesis. *Nature* **386**, 671–674 (1997).
201. Scharpfenecker, M., Fiedler, U., Reiss, Y. & Augustin, H. G. The Tie-2 ligand Angiopoietin-2 destabilizes quiescent endothelium through an internal autocrine loop mechanism. *J. Cell Sci.* **118**, 771–780 (2005).
202. Vestweber, D. VE-Cadherin. *Arterioscler. Thromb. Vasc. Biol.* **28**, 223–232 (2008).
203. Carmeliet, P. Angiogenesis in health and disease. *Nat. Med.* **9**, 653–660 (2003).
204. Brooks, P., Clark, R. & Cheresh, D. Requirement of vascular integrin alpha v beta 3 for angiogenesis. *Science (80-.).* **264**, 569–571 (1994).
205. Avraamides, C. J., Garmy-Susini, B. & Varner, J. A. Integrins in angiogenesis and lymphangiogenesis. *Nat. Rev. Cancer* **8**, 604–617 (2008).
206. Thurston, G., Rudge, J. S., Ioffe, E., Zhou, H., Ross, L., Croll, S. D., Glazer, N., Holash, J., McDonald, D. M. & Yancopoulos, G. D. Angiopoietin-1 protects the adult vasculature against plasma leakage. *Nat. Med.* **6**, 460–463 (2000).
207. Mayer, H., Bertram, H., Lindenmaier, W., Korff, T., Weber, H. & Weich, H. Vascular endothelial growth factor (VEGF-A) expression in human mesenchymal stem cells: Autocrine and paracrine role on osteoblastic and endothelial differentiation. *J. Cell. Biochem.* **95**, 827–839 (2005).
208. Li, H., Daculsi, R., Grellier, M., Bareille, R., Bourget, C., Remy, M. & Amedee, J. The Role of Vascular Actors in Two Dimensional Dialogue of Human Bone Marrow Stromal Cell and Endothelial Cell for Inducing Self-Assembled Network. *PLoS One* **6**, e16767 (2011).
209. Ge, Q. *et al.* VEGF secreted by mesenchymal stem cells mediates the differentiation of endothelial progenitor cells into endothelial cells via paracrine mechanisms. *Mol. Med. Rep.* **17**, 1667–1675 (2017).
210. Helm, C.-L. E., Fleury, M. E., Zisch, A. H., Boschetti, F. & Swartz, M. A. *Synergy between interstitial flow and VEGF directs capillary morphogenesis in vitro through a gradient amplification mechanism*. (2005).
211. Gerhardt, H., Golding, M., Fruttiger, M., Ruhrberg, C., Lundkvist, A., Abramsson, A., Jeltsch, M., Mitchell, C., Alitalo, K., Shima, D. & Betsholtz, C. VEGF guides angiogenic sprouting utilizing endothelial tip cell filopodia. *J. Cell Biol.* **161**, 1163–1177 (2003).
212. Rivron, N. C., Vrij, E. J., Rouwkema, J., Gac, S. Le, Berg, A. van den, Truckenmüller, R. K. & Blitterswijk, C. A. van. Tissue deformation spatially modulates VEGF signaling and angiogenesis. *Proc. Natl. Acad. Sci.* **109**,

6886–6891 (2012).
213. Barkefors, I., Le Jan, S., Jakobsson, L., Hejll, E., Carlson, G., Johansson, H., Jarvius, J., Park, J. W., Li Jeon, N. & Kreuger, J. Endothelial cell migration in stable gradients of vascular endothelial growth factor A and fibroblast growth factor 2: effects on chemotaxis and chemokinesis. *J. Biol. Chem.* **283**, 13905–12 (2008).
214. Akeson, A., Herman, A., Wiginton, D. & Greenberg, J. Endothelial cell activation in a VEGF-A gradient: Relevance to cell fate decisions. *Microvasc. Res.* **80**, 65–74 (2010).
215. Lee, C., Mitsialis, S. A., Aslam, M., Vitali, S. H., Vergadi, E., Konstantinou, G., Sdrimas, K., Fernandez-Gonzalez, A. & Kourembanas, S. Exosomes Mediate the Cytoprotective Action of Mesenchymal Stromal Cells on Hypoxia-Induced Pulmonary Hypertension. *Circulation* **126**, 2601–2611 (2012).
216. Prathipati, P., Nandi, S. S. & Mishra, P. K. Stem cell-derived exosomes, autophagy, extracellular matrix turnover, and miRNAs in cardiac regeneration during stem cell therapy. *Stem Cell Rev.* **13**, 79 (2017).
217. Sahoo, S., Klychko, E., Thorne, T., Misener, S., Schultz, K. M., Millay, M., Ito, A., Liu, T., Kamide, C., Agrawal, H., Perlman, H., Qin, G., Kishore, R. & Losordo, D. W. Exosomes From Human CD34 $^{+}$ Stem Cells Mediate Their Proangiogenic Paracrine Activity. *Circ. Res.* **109**, 724–728 (2011).
218. Takagi, K. & Urist, M. R. The role of bone marrow in bone morphogenetic protein-induced repair of femoral massive diaphyseal defects. *Clin. Orthop. Relat. Res.* 224–31
219. Hollinger, J. O. & Kleinschmidt, J. C. The critical size defect as an experimental model to test bone repair materials. *J. Craniofac. Surg.* **1**, 60–8 (1990).
220. Spicer, P. P., Kretlow, J. D., Young, S., Jansen, J. A., Kasper, F. K. & Mikos, A. G. Evaluation of bone regeneration using the rat critical size calvarial defect. *Nat. Protoc.* **7**, 1918–29 (2012).
221. Holtmaat, A., Bonhoeffer, T., Chow, D. K., Chuckowree, J., De Paola, V., Hofer, S. B., Hübener, M., Keck, T., Knott, G., Lee, W.-C. A., Mostany, R., Mrsic-Flogel, T. D., Nedivi, E., Portera-Cailliau, C., Svoboda, K., Trachtenberg, J. T. & Wilbrecht, L. Long-term, high-resolution imaging in the mouse neocortex through a chronic cranial window. *Nat. Protoc.* **4**, 1128–1144 (2009).
222. Odedra, D., Chiu, L. L. Y., Shoichet, M. & Radisic, M. Endothelial cells guided by immobilized gradients of vascular endothelial growth factor on porous collagen scaffolds. *Acta Biomater.* **7**, 3027–3035 (2011).
223. Alsop, A. T., Pence, J. C., Weisgerber, D. W., Harley, B. A. C. & Bailey, R. C. Photopatterning of vascular endothelial growth factor within collagen-glycosaminoglycan scaffolds can induce a spatially confined response in human umbilical vein endothelial cells. *Acta Biomater.* **10**, 4715–4722 (2014).
224. Baker, B. M., Trappmann, B., Stapleton, S. C., Toro, E. & Chen, C. S. Microfluidics embedded within extracellular matrix to define vascular architectures and pattern diffusive gradients. *Lab Chip* **13**, 3246 (2013).

225. Pati, F., Jang, J., Ha, D.-H., Won Kim, S., Rhie, J.-W., Shim, J.-H., Kim, D.-H. & Cho, D.-W. Printing three-dimensional tissue analogues with decellularized extracellular matrix bioink. *Nat. Commun.* **5**, 3935 (2014).
226. Jang, J., Kim, T. G., Kim, B. S., Kim, S.-W., Kwon, S.-M. & Cho, D.-W. Tailoring mechanical properties of decellularized extracellular matrix bioink by vitamin B2-induced photo-crosslinking. *Acta Biomater.* **33**, 88–95 (2016).
227. Meseguer-Olmo, L., Vicente-Ortega, V., Alcaraz-Baños, M., Calvo-Guirado, J. L., Vallet-Regí, M., Arcos, D. & Baeza, A. *In-vivo* behavior of Si-hydroxyapatite/polycaprolactone/DMB scaffolds fabricated by 3D printing. *J. Biomed. Mater. Res. Part A* **101A**, 2038–2048 (2013).
228. Nudelman, F., Lausch, A. J., Sommerdijk, N. A. J. M. & Sone, E. D. In vitro models of collagen biomineralization. *J. Struct. Biol.* **183**, 258–269 (2013).
229. Tomoaia, G. & Pasca, R.-D. On the Collagen Mineralization. A Review. *Clujul Med.* **88**, 15–22 (2015).
230. Qiu, Z.-Y., Cui, Y., Tao, C.-S., Zhang, Z.-Q., Tang, P.-F., Mao, K.-Y., Wang, X.-M. & Cui, F.-Z. Mineralized Collagen: Rationale, Current Status, and Clinical Applications. *Mater. (Basel, Switzerland)* **8**, 4733–4750 (2015).
231. Constantz B.R., G. S. Mineralized Collagen. (1993).
232. W. Zhang, S. S. Liao, and & Cui*, F. Z. Hierarchical Self-Assembly of Nano-Fibrils in Mineralized Collagen. (2003). doi:10.1021/CM030080G
233. Liao, S. S., Cui, F. Z., Zhang, W. & Feng, Q. L. Hierarchically biomimetic bone scaffold materials: Nano-HA/collagen/PLA composite. *J. Biomed. Mater. Res.* **69B**, 158–165 (2004).
234. Wang, S., Yang, Y., Zhao, Z., Wang, X., Mikos, A. G., Qiu, Z., Song, T., Sun, X., Zhao, L., Zhang, C. & Cui, F. Mineralized Collagen-Based Composite Bone Materials for Cranial Bone Regeneration in Developing Sheep. (2017). doi:10.1021/acsbiomaterials.7b00159
235. Marks, S. C. & Odgren, P. R. Chapter 1 – Structure and Development of the Skeleton. in *Principles of Bone Biology* 3–15 (2002). doi:10.1016/B978-012098652-1.50103-7
236. Rho, J.-Y., Kuhn-Spearing, L. & Zioupos, P. Mechanical properties and the hierarchical structure of bone. *Med. Eng. Phys.* **20**, 92–102 (1998).
237. Akkus, O. Chapter 1 – Bone Morphology and Organization. in *Basic and Applied Bone Biology* 3–25 (2014). doi:10.1016/B978-0-12-416015-6.00001-0
238. Webster, T. J. & Ahn, E. S. Nanostructured biomaterials for tissue engineering bone. *Adv. Biochem. Eng. Biotechnol.* **103**, 275–308 (2007).
239. Takahashi, N., Udagawa, N., Takami, M. & Suda, T. Chapter 7 – Cells of Bone: Osteoclast Generation. in *Principles of Bone Biology* 109–126 (2002). doi:10.1016/B978-012098652-1.50109-8
240. Aubin, J. E. & Triffitt, J. T. Chapter 4 – Mesenchymal Stem Cells and Osteoblast Differentiation. in *Principles of Bone Biology* 59–81 (2002). doi:10.1016/B978-012098652-1.50106-2
241. Clevers, H. Wnt/β-Catenin Signaling in Development and Disease. *Cell* **127**, 469–480 (2006).
242. Ducy, P., Zhang, R., Geoffroy, V., Ridall, A. L. & Karsenty, G. Osf2/Cbfa1: a transcriptional activator of osteoblast differentiation. *Cell* **89**, 747–54 (1997).

243. Nakashima, K., Zhou, X., Kunkel, G., Zhang, Z., Deng, J. M., Behringer, R. R. & de Crombrugghe, B. The novel zinc finger-containing transcription factor osterix is required for osteoblast differentiation and bone formation. *Cell* **108**, 17–29 (2002).
244. Bellido, T., Plotkin, L. I. & Bruzzaniti, A. Chapter 2 – Bone Cells. in *Basic and Applied Bone Biology* 27–45 (2014). doi:10.1016/B978-0-12-416015-6.00002-2
245. Golub, E. E. & Boesze-Battaglia, K. *The role of alkaline phosphatase in mineralization*.
246. Mercado-Pagán, Á. E., Stahl, A. M., Shanjani, Y. & Yang, Y. Vascularization in Bone Tissue Engineering Constructs. *Ann. Biomed. Eng.* **43**, 718–729 (2015).
247. Lafage-Proust, M.-H., Roche, B., Langer, M., Cleret, D., Vanden Bossche, A., Olivier, T. & Vico, L. Assessment of bone vascularization and its role in bone remodeling. *Bonekey Rep.* **4**, 662 (2015).